Gran Sasso Science Institute
Astroparticle Physics program
XXXII cycle

MEASUREMENT OF COSMIC RAY PROTON + HELIUM FLUX WITH THE DAMPE EXPERIMENT

PhD candidate
Zhaomin Wang

Supervisor:
Prof. Ivan De Mitri

Abstract

This thesis concentrates on the measurement of cosmic-ray light component (proton + helium) spectrum with the Dark Matter Particle Explorer (DAMPE). In chapter one, an introduction on cosmic-ray history is given together with the acceleration mechanism and some recent experiments. A description on DAMPE system is presented in chapter two, which includes its sub-detectors, scientific targets and parameters. There are various challenges in measuring cosmic ray energy with a limited-size calorimeter (like the BGO of DAMPE). In chapter three, various unfolding methods for reconstructing the primary energy of cosmic ray nuclei are discussed. It turns out that the method based on the Bayes theorem has the best performance on reconstructing the cosmic-ray energy for DAMPE. The test results show that the Bayes method is capable of reconstructing nuclei energy with good accuracy on both MC samples (bias within 2%) and real data that come from the test beams at CERN (bias within 3%). In chapter four, a detailed description on the measurement of cosmic ray protons + helium spectrum is presented, which involves the candidates selection, energy reconstruction and calculation of the statistical and systematic uncertainties. Finally, the proton + helium spectrum with energy 40 GeV to 100 TeV is presented.

Contents

List of Figures

List of Tables

Introduction

Research on Cosmic Rays (CRs) has been a hot topic ever since their first discovery by Victor Hess in 1912. At present,it is known that 99% of CR particles are nuclei. The remaining parts include electrons, gamma-rays and a very small component (less than 0.1%) of anti-particles. The energies of CR particles span from few MeVs up to 10^{20} eV. A precise measurement on CR energy spectrum could advance our understanding on CR origin and acceleration mechanism, thus, shedding light on the evolution of our universe.

Launched on 17 December 2015, the Dark Matter Particle Explorer (DAMPE) is a state of the art satellite-borne experiment for direct CR detection. While it was conceived mainly to search for signatures of dark matter particles in the lepton and gamma ray spectra, DAMPE distinguishes itself also by its capacity to measure CR nuclei fluxes with unprecedented resolution (better than 40% at 800 GeV for protons) in an energy range from few tens of GeV up to 100 TeV. Light nuclei (proton and helium elements) are the dominant components of CRs and account for ∼99% of CR flux. DAMPE has published its measurement on CR proton flux [6] (see chapter 1), in which a spectral softening at $\sim$ 13 TeV is confirmed. The Understanding on this spectral feature (for instance to figure out the softening is energy-dependent or rigidity-dependent) can be enhanced by measuring other type of CR nuclei. In this thesis, the CR proton + helium spectrum with energy from 40 GeV to 100 TeV will be measured. Selecting the proton + helium samples has the advantages of almost no background and very high purity. Besides, some selection cuts used for measuring the proton or helium spectra alone can be set less stringent or removed. Therefore, a larger statistics can be obtained, which gives the potential to extend the spectrum to higher energy and reveal subtle features. Moreover, since the light components spectrum measured by DAMPE can reach such a high energy which overlaps with some ground-based experiment measurements, a comparison on light nuclei spectrum between the direct and indirect measurements can be done.

In chapter one, we will briefly describe the history of CR research together with CR acceleration models from which a power law feature spectrum can be derived. Then

some of the recent experiments on both CR direct and indirect measurements will be presented together with part of their scientific results.

In chapter two, the DAMPE detector system will be introduced. DAMPE is composed by four sub-detectors: the plastic scintillator detector, the silicon-tungsten tracker detector, the bismuth germanium oxide imaging calorimeter and the neutron detector. The scientific goals and detector parameters of DAMPE will also be described in this chapter.

A precise energy measurement on CR particles plays an essential role in measuring a cosmic ray spectrum. In chapter three, three widely used energy unfolding methods for reconstructing the energy of hadronic particles will be discussed: The Bayes method, the singular value decomposition method and the iterative dinamically stabilized method. The Monte Carlo samples and beam test data of DAMPE are used to test their performance on reconstructing the nucleus energy.

In chapter four, we will introduce the data analysis on proton + helium spectrum. The procedures involve candidate selection, energy reconstruction and analysis on systematic uncertainties. Finally, the CR proton + helium spectrum with energy between 40 GeV and 100 TeV will be presented. Some discussions on the spectral features and comparisons with previous measurements will also be made.

Chapter 1

Cosmic-Ray Physics

After the first discovery of Cosmic Rays (CRs) in 1912 (by Victor Hess), researchers have never stopped their enthusiasm on studying the related topics. For instance, the CR origin and acceleration mechanism. Up to today, though tremendous achievements have been made in both theoretical and experimental parts, there are still various questions regarding the nature of CRs waiting for being explored. In this chapter, a brief introduction on the history and development of CR research are given. Some recent experiments and their major results are also presented.

1.1 The history of Cosmic-Ray physics

In 1896, Henri Becquerel found the phenomenon of radioactivity. The researchers realized that some materials could produce ionization, which are called the radioactive materials [7]. The charged particles radiated by radioactive materials can ionize the gas inside a charged vessel, which leads to the electroscope that inside the same vessel being discharged then. The discharged rate of the electroscope reflects the counts of the entering charged particles, thus, provided a primitive method to measure a flux of charged particles. At around 1900, researchers improved the sensitivity of the electroscope device and found that the discharging phenomenon existed even though the electroscope was isolated with the radioactive materials [1]. There were two hypotheses upon this phenomenon: The radiation was terrestrial or extraterrestrial. An experiment was then needed to confirm one of the explanations.

The location for performing the experiment must be far away from the ground in order to avoid the terrestrial source of radiation. The ionization rate would decrease if the excess atmospheric radiation was terrestrial. In 1909, Theodor Wulf performed the

FIGURE 1.1: Victor Hess (right inside the basket) was preparing for the balloon experiment.

measurement on the ionization rate at the top of the Eiffle Tower [8]. However, due to the limitation of the height (only 300 m from the ground), the result was too similar to the ground-based measurement to derive any decisive conclusions.

In 1912, Victor Hess improved the accuracy of the electroscope used by Wulf and measured the ionization rate at the height of 5200 m by using a balloon as the platform. Hess found that the radiation rate reach a minimum at the altitude around 1000 m then increase significantly [9] after that. Hess concluded that the increase of the radiation rate was due to an extraterrestrial source basing on the measurement. The same conclusion was then made by Werner Kolhorster by performing another balloon experiment at the altitude of $\sim$ 9200 m [10]. The experiment of Hess was recognized as the first discovery of the CRs, thus Hess was awarded the Nobel Prize in 1936. Moreover, Hess noticed that there was barely difference between the daytime and night regarding the radiation rate as well. The hypothesis that the sun was the direct source of the radiation was excluded based on this non-difference phenomenon.

In 1927, Jacob Clay found a variation of the CR intensity regarding the latitude [11], which implies that the CRs are charged particles that can be deflected by the geomagnetic field. In 1939, Pierre Auger and his collaborators found that groups of CRs could simultaneously reach the detectors that were separated as large as 200 m [12]. This phenomenon implies that the atmospheric CRs could be secondary particles induced from a single high energy primary particle. Besides, Pierre Auger concluded that the arrival primary particles on Earth can reach the energy up to 10^{15} eV. In 1941, Marcel Schein and his group found that the compositions of the CRs are mainly protons [13]. In 1962, John Linsley observed an CR event with energy of 10^{20} eV [14]. More detailed reviews

of the CRs history can be found in [15]. At present, more accurate measurements on CRs provide the possibilities on not only identifying different CR species but studying on their spectral features as well, which makes possible the study on CR acceleration and propagation mechanisms in our universe. Some recent CR experiments and their measured spectra will be introduced in section 1.3.

1.2 Acceleration of cosmic-ray particles

The existence of ultra high energy CRs implies an effective acceleration mechanism in the universe. Meanwhile, the power-law feature of CR energy spectrum set some constraints on acceleration models. The CRs with energy lower than the "knee" [1] are the dominating part of the CRs spectrum. It is a common belief that these CRs are accelerated by shock waves in a supernova remnant. The shell-like supernova remnant can be the source of our galaxy CRs [16]. Meanwhile extra-galactic CRs could be produced by active galactic nuclei [17].

In 1949, Enrico Fermi proposed a model which can result in a power-law shape of CR spectrum which is recognized as the second-order Fermi acceleration mechanism [18]. Then from late 1970s, researchers modified the model and made it a more effective mechanism to describe the picture of CR acceleration process [19]. The modified version of the second-order Fermi acceleration mechanism is referred as diffusive shock acceleration mechanism, which could not only result in a power-law-featured CR spectrum but also give a spectral index quantitatively. Though the recent CRs observation results have revealed some more complex features than the simple single-power-law feature, the acceleration mechanism described in the diffusive shock acceleration model is still the foundation of new models that try to explain the observed new features of the CR spectrum. Therefore, the second-order Fermi acceleration mechanism and the diffusive shock acceleration mechanism will be introduced in this section. The description follows [7].

1.2.1 The second-order Fermi acceleration mechanism

In 1949, Fermi proposed a picture in which CR particles collide with clouds in interstellar medium, which makes possible accelerating CR to to a very high energy. The cloud is a cluster of gas with density much larger than its background (vacuum space). The cloud is assumed to move in velocity V with stochastic directions. A particle would gain some

[1] The "knee" refers to a spectral softening at energy of $\sim 10^{15}$ eV for the all-particle spectrum. The spectral index changes from ~ -2.7 before the knee to ~ -3.1 after the "knee".

energies in collision with the cloud. If the particle remains in the acceleration region for a characteristic time $\tau_{\rm esc}$, a power law feature spectrum can be resulted in.

Supposing that a particle with mass of m, velocity of v and energy of E collides with a cloud with velocity of V and mass M, where M $\gg$ m. The particle energy E in the reference frame of the cloud is:

$$\mathrm{E}' = \gamma(\mathrm{E} + \mathrm{V} \cdot \mathrm{p} \cdot \cos\theta), \tag{1.1}$$

where γ is the Lorentz factor of the cloud and equals $[1 - (\mathrm{V}/\mathrm{c})]^{-1/2}$, p is the particle momentum, θ represents the angle between the particle and cloud velocities. In the cloud reference frame, the x (assuming its direction is the same with the direction of V) component of the particle momentum becomes:

$$\mathrm{p}'_{\mathrm{x}} = \gamma \left(\mathrm{p}_{\mathrm{x}} + \frac{\mathrm{V} \cdot \mathrm{E}}{\mathrm{c}^2} \right). \tag{1.2}$$

The particle energy is conserved during the collision, and the momentum p_{x} is reversed after the collision. Therefore the energy after collision (E'') becomes:

$$\mathrm{E}'' = \gamma(\mathrm{E}' + \mathrm{V} \cdot \mathrm{p}'_{\mathrm{x}}) \tag{1.3}$$

in the frame of the observer. By combing equation 1.1, 1.2 with equation 1.3 and using:

$$\frac{\mathrm{p}_{\mathrm{x}}}{\mathrm{E}} = \frac{\mathrm{m} \cdot \mathrm{v} \cdot \gamma \cdot \cos\theta}{\mathrm{m} \cdot \mathrm{c}^2 \cdot \gamma} = \frac{\mathrm{v} \cdot \cos\theta}{\mathrm{c}^2}\ , \tag{1.4}$$

the E'' can be derived as:

$$\mathrm{E}'' = \gamma^2 \cdot \mathrm{E} \left[1 + \frac{2 \cdot \mathrm{V} \cdot \mathrm{v} \cdot \cos\theta}{\mathrm{c}^2} + \left(\frac{\mathrm{V}}{\mathrm{c}} \right)^2 \right]\ , \tag{1.5}$$

thus, the energy change ΔE equals:

$$\Delta\mathrm{E} = \mathrm{E}'' - \mathrm{E} = \mathrm{E} \left[\frac{2\mathrm{Vv}\cos\theta}{\mathrm{c}^2} + 2 \left(\frac{\mathrm{V}}{\mathrm{c}} \right)^2 \right]\ . \tag{1.6}$$

The θ is stochastic. Supposing v $\approx$ c, the probability of a collision happens with a pitch angle θ is proportional to $\gamma[1 + (\mathrm{V}/\mathrm{c}) \cdot \cos\theta]$. Moreover, the probability of the pitch angle lying between θ and $\theta + \mathrm{d}\theta$ is proportional to $\sin\theta \mathrm{d}\theta$. Averaging over the possible values of θ, which are in the range of 0 to π, results in:

$$\left\langle \frac{\Delta\mathrm{E}}{\mathrm{E}} \right\rangle = 2 \left(\frac{\mathrm{V}}{\mathrm{c}} \right) \frac{\int_0^\pi \cos\theta \cdot [1 + (\frac{\mathrm{V}}{\mathrm{c}}) \cdot \cos\theta] \mathrm{d}\theta}{\int_0^\pi [1 + (\frac{\mathrm{V}}{\mathrm{c}}) \cdot \cos\theta] \mathrm{d}\theta} + 2 \left(\frac{\mathrm{V}}{\mathrm{c}} \right)^2 = \frac{8}{3} \left(\frac{\mathrm{V}}{\mathrm{c}} \right)^2\ . \tag{1.7}$$

Equation 1.7 indicates that the average energy gain in a collision is in second-order of V/c. Given the fact the average time between the subsequent collisions is 2L/c where L represents the mean free path for CR particles, the average change of energy in a collision is:

$$\frac{dE}{dt} = \frac{4}{3}\left(\frac{V^2}{c \cdot L}\right) E = \alpha E \ . \tag{1.8}$$

According to equation 1.8, a power-law spectrum can be resulted in by using the CR diffusion-loss equation:

$$\frac{dN(E)}{dt} = D \cdot \nabla^2 N(E) + \frac{\partial}{\partial E}\left[\frac{dE}{dt} \cdot N(E)\right] - \frac{N}{\tau_{esc}} + Q(E) \ , \tag{1.9}$$

where D represents the diffusion coefficient, N(E) is the number of the particles, τ_{esc} is the average time for a particle remains in the acceleration region, Q(E) represents the particle injection rate from a source. Since a steady-state, where no new particles will come into the system, is being considered here, we have dN(E)/dt, $D\nabla^2 N(E)$ and Q(E) equal 0. With these premises, equation 1.9 turns to:

$$-\frac{d}{dE}\left[\alpha \cdot E \cdot N(E)\right] - \frac{N(E)}{\tau_{esc}} = 0, \tag{1.10}$$

which leads to

$$\frac{dN(E)}{dE} = -\left(1 + \frac{1}{\alpha \cdot \tau_{esc}}\right)\frac{N(E)}{E} \ . \tag{1.11}$$

A power law shape spectrum can be resulted in by solving the above differential equation as:

$$N(E) = \text{constant} \cdot E^{-x} \ , \tag{1.12}$$

with $x = 1 + (\alpha \cdot \tau_{esc})^{-1}$.

Even though the second-order Fermi acceleration mechanism could lead to a power-law CR energy spectrum, there are still several questions being not answered. For instance: Given the fact that the velocity of the cloud V is very small compared with light velocity c, and the mean free path for CRs is $\sim$ 0.1 pc, thus the collision between a particle and cloud would likely happen a few times a year. Such a low frequency collision can barely accelerate the CRs to such a high energy as observed on Earth. Moreover, the second-order acceleration mechanism could not reveal the spectral index quantitatively. Considering these issues, a more effective acceleration mechanism, called diffusive shock acceleration mechanism, were proposed in 1970s (see the following section).

1.2.2 The diffusive shock acceleration mechanism

Based on the second-order Fermi acceleration mechanism, the characteristic of the diffusive shock acceleration mechanism is that it can result in an energy spectrum with spectral index of ~ 2. In the diffusive shock acceleration model, a constant κ is defined in the equation $E = \kappa E_0$, where E_0 and E represent the average energy of CR particles before and after a collision respectively. Therefore, κ actually reflects energy gain in one collision. Furthermore, another constant P is defined as the representation of the probability that a particle remains in the acceleration region after a collision. By using of κ and P, there will be $N = P^k N_0$ particles with average energy of $E = \kappa^k E_0$ remaining in the acceleration region after k times of collision. After some transformations, we can easily get:

$$\frac{\ln(N/N_0)}{\ln(E/E_0)} = \frac{\ln P}{\ln \kappa} \ , \tag{1.13}$$

which leads to

$$\frac{N}{N_0} = \left(\frac{E}{E_0}\right)^{\ln P/\ln \kappa} \ . \tag{1.14}$$

From equation 1.14, a pow law energy spectrum can be derives:

$$N(E)dE = \text{constant} \cdot E^{-1+(\ln P/\ln \kappa)} dE \ . \tag{1.15}$$

Combing equation 1.14 with equation 1.12, it is clear that $(\ln P/\ln \kappa) = -(\alpha \tau_{esc})^{-1}$. The definitions of P and κ indicates that P is related to τ_{esc} and κ is related to α.

In 1970s, various research groups implemented the first-order Fermi acceleration mechanism in different astrophysical environments and produced various CR acceleration models [20–23]. These models are associated with acceleration processes in strong shock waves. In [23], a very clear picture upon an individual particle acceleration process is depicted. In the following paragraphs, we will follow the [23] to describe the acceleration mechanism that could result in an index of CR spectrum quantitatively.

Supposing there is a strong shock wave with a supersonic front velocity $\mathbf{v_s}$ moving in the interstellar gas ((a) of Fig. 1.2). The gas in front of the shock is with density ρ_1, velocity $\mathbf{v_1}(=0)$ and temperature T_1. The density, velocity and temperature of the gas behind the shock are ρ_2, $\mathbf{v_2}$, and T_2 respectively. It will be more convenient to analyse the dynamics of this system in the reference frame of the shock. In this case, the velocity of the upstream [2] gas is $-\mathbf{v_s}$. Considering the continuity of the system, we have:

$$\rho_1 \cdot v_1 = \rho_2 \cdot v_2 \ . \tag{1.16}$$

[2] The upstream area refers to the area of the shock front. Meanwhile, the downstream area refers to the back shock area (as shown in (a) of Fig. 1.2).

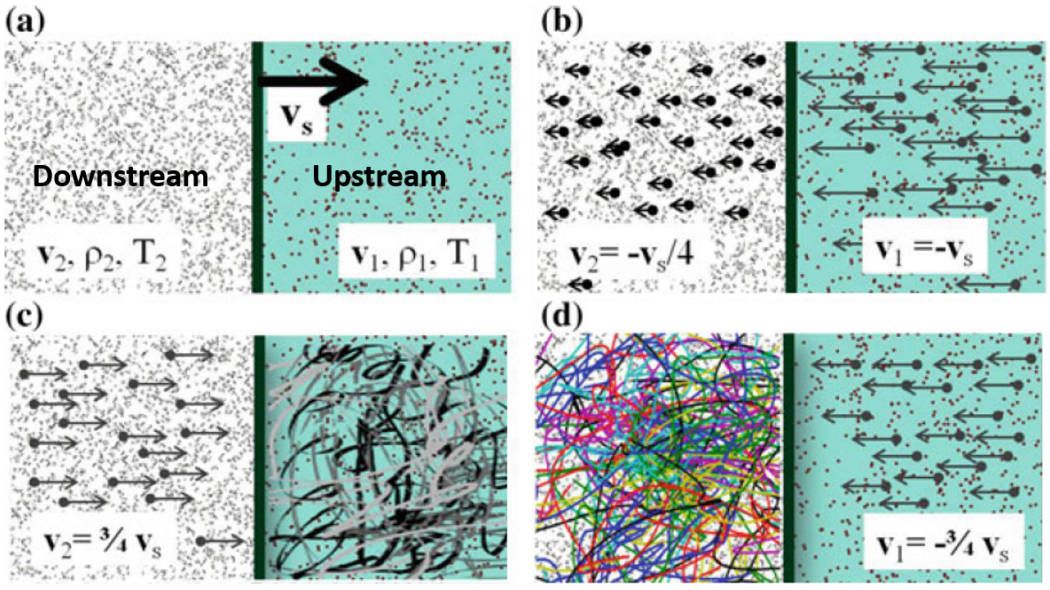

FIGURE 1.2: The activities of the particles in a nearby region of a strong shock wave. The black bar in the middle of each plot is the shock front, the region behind the shock front is called downstream, meanwhile the region in front is called the upstream. (a): A moving shock wave with a supersonic velocity $\mathbf{v_s}$ in the observer frame; (b): The same situation with (a) seen from the rest frame of the shock front; (c): The flow of the downstream material observed in the rest frame of the upstream. The velocities of the upstream particles are isotropic; (d): The same situation with (c) but observed in the rest frame of the downstream, from where the velocities of the downstream material are isotropic.

In a strong shock, $\rho_2/\rho_1 = \mathrm{R}$, where R is determined by the gas compositions. According to [7], R can be taken as 4. Then we have $|\mathbf{v_1}|/|\mathbf{v_2}| = 4$ and $\mathbf{v_1} = -\mathbf{v_s}$, $\mathbf{v_2} = -\mathbf{v_s}/4$ (as shown in (b) of Fig. 1.2).

The velocity of upstream gas is 0 if we see from the reference frame of the upstream gas, however, the velocity of particles in the upstream region are stochastic because of the scattering. The gas velocity in the downstream region becomes 3/4 $\mathbf{v}_\mathrm{s}$ ((c) of the Fig. 1.2) in this case. When a particle from the upstream crosses the shock front and reaches the downstream, it encounters the gas with velocity of 3/4 $\mathbf{v}_\mathrm{s}$. In this case, a head-on collision (θ larger than $\pi/2$) happens and the particle gains energy in order of $\Delta\mathrm{E}/\mathrm{E} \sim |\mathbf{v_s}|/\mathrm{c}$. Then the particle has the probability being scattered back into the upstream if we see from the frame of the reference of the downstream, as it is shown in (d)of Fig. 1.2. The particle gains energy also in order of $\Delta\mathrm{E}/\mathrm{E} \sim |\mathbf{v_s}|/\mathrm{c}$ for going back to the upstream. Therefore, the particle will obtain energy once it crosses the shock front no matter from downstream to upstream or the other way around. The energy increment is the same for both processes. In order to derive the P and κ in equation 1.15 quantitatively, [22] estimated the energy gain from one acceleration cycle: First,

when a particle passes the shock from upstream to downstream, the energy becomes:

$$E' = \gamma(E + p_x \cdot v_1) \ , \tag{1.17}$$

with v_1 representing the absolute value of gas velocity in upstream. v_1 is equal to $3/4|\mathbf{v_s}|$. The Lorentz factor of v_1 is represented by γ. Since $v_1 \ll c$, $\gamma \simeq 1$. p_x is the x momentum where x-axis is taken to be perpendicular to the shock front. The particle is relativistic, its energy equals pc. Therefore, $p_x = (E/c)\cos\theta$. The ratio between the energy change and the original energy is $\Delta E/E = (v_1/c)\cos\theta$. The probability of a particle passing through the shock front with pitch angle between θ and $d\theta$ is proportional to $2 \cdot \sin\theta \cdot \cos\theta d\theta$ with θ in the range between 0 and $\pi/2$. Thus, the average energy gain for the crossing process is:

$$\left\langle \frac{\Delta E}{E} \right\rangle = \frac{V}{c} \int_0^{\pi/2} \cos^2\theta \cdot \sin\theta d\theta = \frac{2}{3}\frac{V}{c} \ , \tag{1.18}$$

with V equals v_1 here. Then the particle is scattered inside the downstream and may recross the shock front into the upstream, it will gain the same fraction of energy as equation 1.18. Therefore, a complete acceleration cycle (from the downstream enters the upstream then comes back to the downstream) makes the particle gain the energy as:

$$\left\langle \frac{\Delta E}{E} \right\rangle = \frac{4}{3}\frac{V}{c} \ . \tag{1.19}$$

Consequently, the κ in equation 1.15 is:

$$\kappa = \frac{E}{E_0} = 1 + \frac{4}{3}\frac{V}{c}. \tag{1.20}$$

For the escape probability, [22] gives that: the fraction of the escaping particles per unite time equals v_s/c, thus the probability of particles remain inside the acceleration region is:

$$P = 1 - \frac{v_s}{c} \ . \tag{1.21}$$

Since v_s is non-relativistic, we have:

$$\ln P = \ln(1 - \frac{v_s}{c}) \simeq -\frac{v_s}{c}, \quad \ln\beta = \ln(1 + \frac{v_s}{c}) \simeq \frac{v_s}{c}, \tag{1.22}$$

thus, $\ln P/\ln\beta = -1$. Back to equation 1.15, we can result in:

$$N(E)dE \propto E^{-2}dE \tag{1.23}$$

A power-law spectrum with a specific spectral index is derived in equation 1.23. The spectral index is -2 instead of the observed -2.7. This might be due to the CR propagation

and energy loss effects, more detail on this issue can be found in [1, 7].

1.3 The observations on cosmic rays

It has been more than 100 years after the CRs were first discovered. Up to today, more advanced devices are used to make more precised measurements on CR. In general, there are two categories of CR experiments: direct and indirect measurements. Both of them have pros and cons. Direct measurement needs to send detector system out of the Earth atmosphere to avoid CRs interacting with atoms of the air. Direct experiments are normally based on balloon-borne or space-borne detectors which have a relatively better charge and energy resolutions and their results are with less systematic uncertainty. However, due to the limitation of the experiment platform, the sizes of direct detection devices are relatively small, so the geometry acceptances of direct detection experiments are much less than the indirect detection experiments. On the other hand, detectors of indirect CR experiments are built on the ground. This type of the experiment generally have a larger acceptance that guarantees a larger statistics. Besides, indirect experiment can measure the CR energy much higher than direct experiment. The disadvantages of indirect CR measurement include a worse energy resolution and large systematic uncertainty. Moreover, because of the worse charge resolution, they can barely identify the categories of incoming particles.

The equation for computing the measured CR flux is the same for direct and indirect measurements. The differential CR intensity $\Phi(\mathrm{E})$ can be derived as:

$$\Phi(\mathrm{E}) = \frac{\Delta \mathrm{N}}{\mathrm{A} \cdot \mathrm{T} \cdot \Delta \mathrm{E}} \ , \tag{1.24}$$

where ΔN represents the number of collected CR events with their energies inside the interval [E, E+ΔE]. T is the collection time and A represents the geometry acceptance. The differential CR energy spectrum (or simply energy spectrum) measured by various experiments is shown in Fig. 1.3 where both direct and indirect measurement results are included.

The integral intensity of CRs with energy larger than E_0 can be computed as:

$$\Phi(\mathrm{E} > \mathrm{E}_0) = \int_{\mathrm{E}_0}^{\infty} \Phi(\mathrm{E}) \mathrm{dE} \ . \tag{1.25}$$

If a hemisphere is considered as the acceptance surface, the integral flux can be written as [1]:

$$\mathcal{F}(\mathrm{E} > \mathrm{E}_0) = \pi \cdot \Phi(\mathrm{E} > \mathrm{E}_0) \ . \tag{1.26}$$

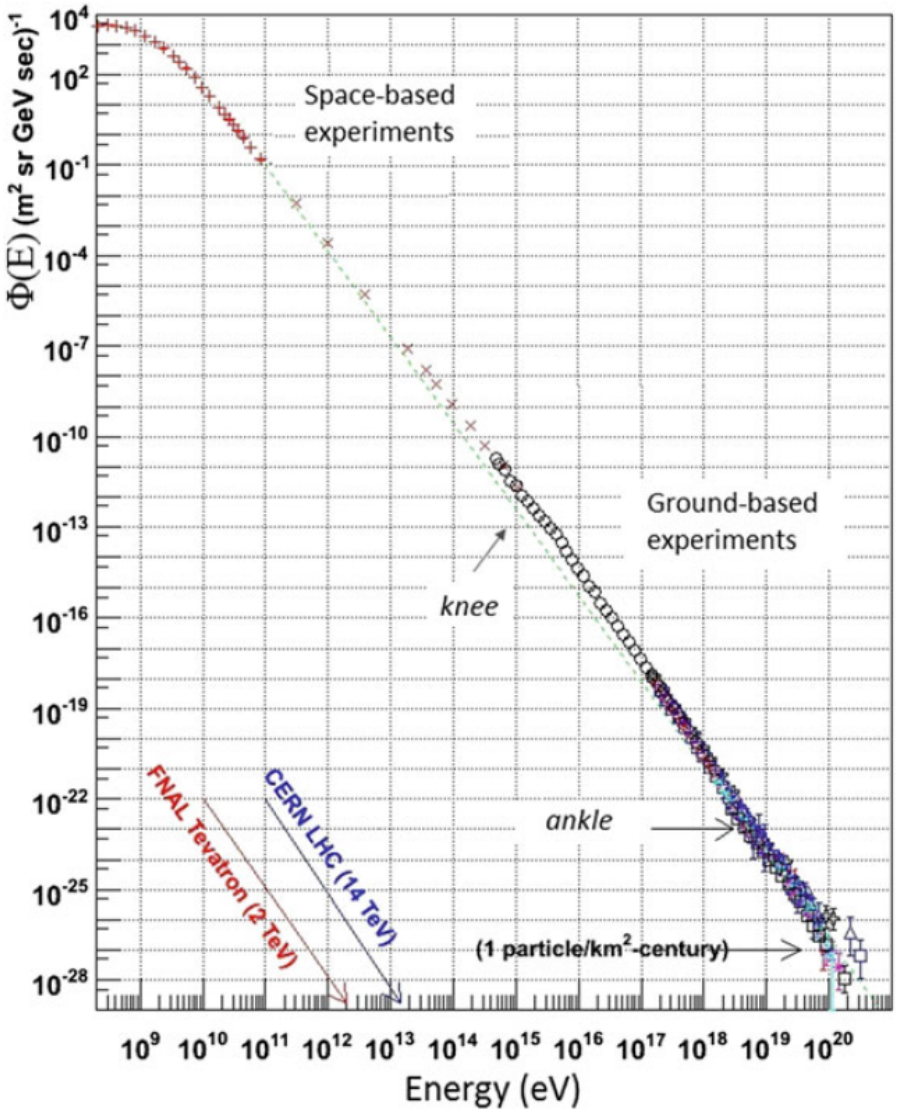

FIGURE 1.3: The CR energy spectrum measured by various experiments. The red arrows marks the energy that can be reached at the Tevatron collider at Fermilab and the blue arrows reflects the reached energy and at the LHC collider at CERN. The plot is taken from [1]

The CR flux is already very low at energy larger than 10^{15}eV (1PeV) according to equation 1.26.The measurements on CR spectrum with energy larger than 1 PeV are generally done by ground-based CR experiments. At lower energy region (less than 100TeV), the direct detection experiments with better charge resolution and less uncertainty are widely used. Various nuclei fluxes measured by direct detection experiments are shown in Fig. 1.4.

The element abundance comparison between CR and the solar system is presented in Fig. 1.5, where a remarkable resemblance can be found. The similarity of the abundances implies that the sources of CR nuclei have a similar composition with our solar system. However, there are still some abundance divergences regarding several elements.

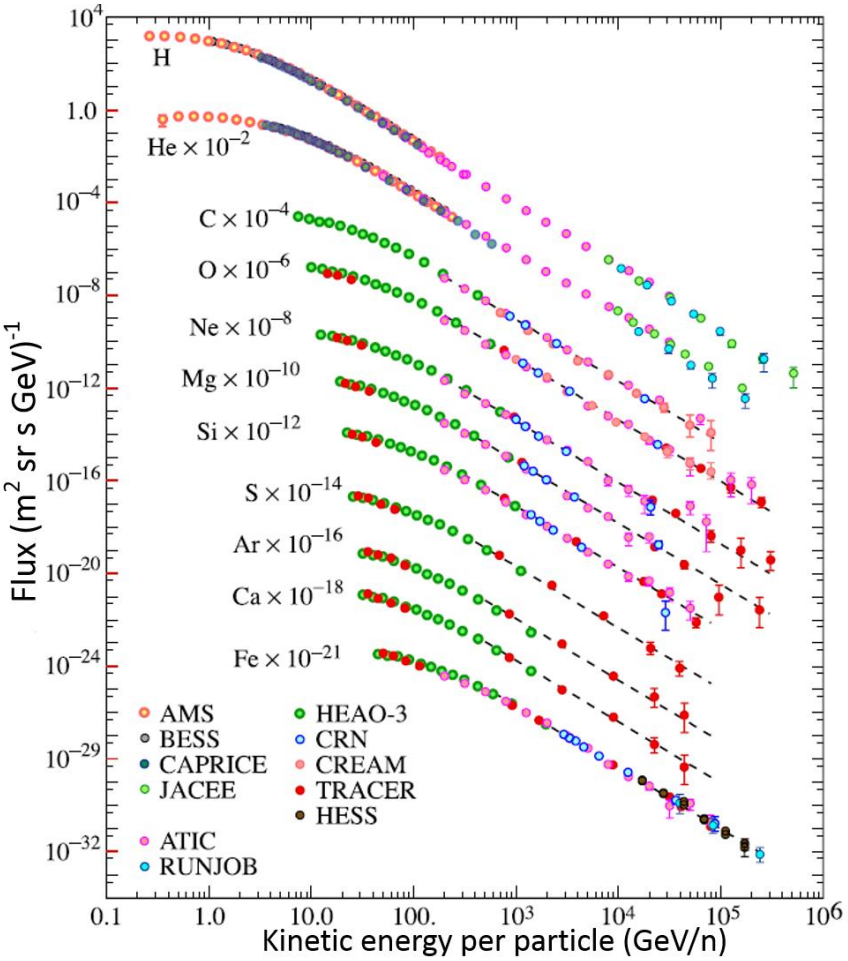

FIGURE 1.4: The CR chemical components measured by various experiments. The fluxes have been multiplied by different numbers to avoid overlap.

For instance, the Li, Be, B nuclei. The divergence can be explained by CR spallation during their propagation. Cosmic ray C, N, O elements have certain probabilities to get fragmentation in interstellar medium and produce secondary Li, Be, B nuclei. A crucial topic for CR is to measure the ratio of the secondary to primary nuclei (for instance, the ratio of B/C), which makes possible the improvement of our understanding on CR propagation.

In the following sub-sections, some recent CR experiments will be introduced. Since the major issue of this thesis is about the measurement on CR light nuclei flux (see chapter three and four), therefore, mainly CR nuclei spectra measured by these experiments will be presented.

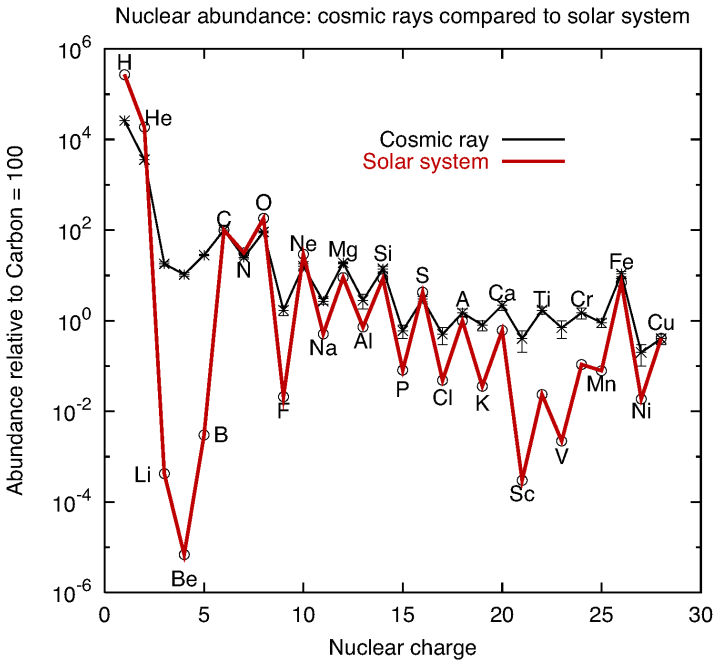

FIGURE 1.5: The comparison of the relative chemical abundance between the CR and the solar system. The abundances are normalized by setting the C compositions into equivalence.

1.3.1 Cosmic ray direct detection experiments

The Alpha Magnetic Spectrometer 02 (AMS-02) [24], the CALorimetric Electron Telescope (CALET) [25] and the DArk Matter Particle Explorer (DAMPE) [26] are chosen as the representatives for CR direct detection experiments and are introduced in this section.

AMS-02

AMS-02 is a space-borne CR experiment. The detector system was installed in the International Space Station (ISS) on May 2011. Its scientific objectives include searching the signs of dark matter particles and measure the fluxes of CR electrons, nuclei and antimatter particles. Up to now, AMS-02 has collected more than 140 billions CR events. A series of significant results involving CR electron/positron, nuclei and anti-proton has been published [27].

The layout of the detector system is presented in Fig. 1.6. The system is composed mainly by six functionality modules: The silicon tracker; the Transition Radiation Detector (TRD); the Time Of Flight (TOF) detector; the Ring Imaging Cherenkov Detector (RICD); the Electronmagnetic CALorimeter (ECAL) and the magnet system. There are nine layers of the silicon tracker. The first tracker layer is located at the top of the TRD, the second tracker layer is placed just above the system magnetic field.

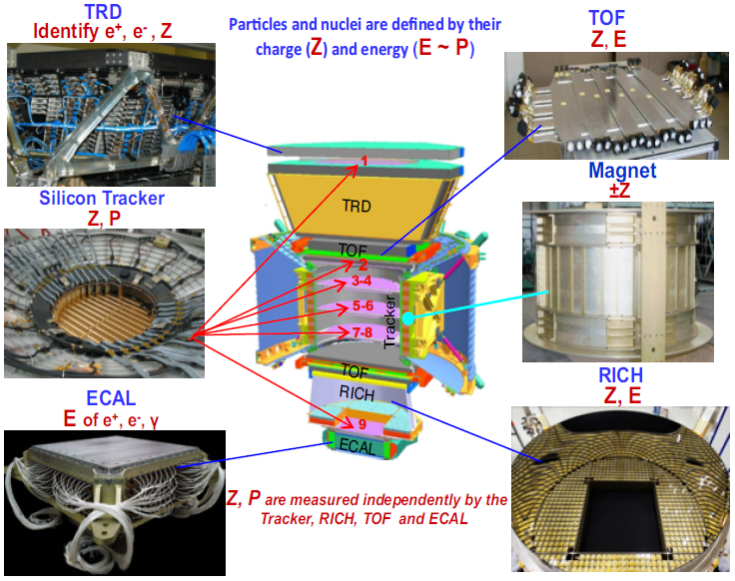

FIGURE 1.6: The layout of the AMS-02.

The third to eighth layers are covered by the magnetic field to measure the gyroradius of charge particles in order to deduce their momenta and energies. The tracker within the magnetic field can be used to identify positive and negative charged particles as well [28–30]. Below the first layer of the tracker, there is the TRD, which plays an essential role in lepton/hadron discrimination [31]. The TOF detectors, composed by four planes of segmented scintillation counter bars, are arranged with two planes on top of the magnet and two planes below the bottom of it. The directions of the counter bars of the neighboring planes are orthogonal. The TOF works for offering trigger for the data acquisition system and measuring charge information of entering CRs. Besides, with an excellent time resolution, the TOF can be used to measure the time information of particles as well. A precise measurement on the arrival time to certain TOF could be used to reject the down-going particles, thus help to select CR candidates [32]. Below the lower TOF, the RICD is located. The RICD can estimate the velocities and charges of entering particles by measuring the Cherenkov cone along the particle trajectories [33]. Going down from the RICD, there is the ninth layer of the tracker, then at the bottom of the whole system, the ECAL is installed. The ECAL is conceived to perform a 3D imaging on the particle showers and measure their energies. The leptons and hadrons can be separated as well by looking at their shower shape in the ECAL [34].

The proton [35] and helium [36] spectra measured by AMS-02 are presented in Fig. 1.7. The spectra deviate from a single power law feature and a spectral hardening have been found at $\sim$ 336 GV for proton and $\sim$ 245 GV for helium.

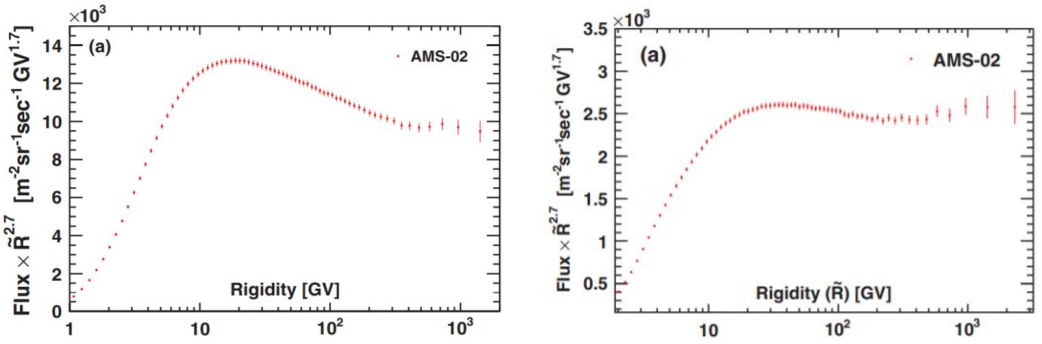

FIGURE 1.7: The CR proton (left) and helium (right) spectra measured by AMS-02.

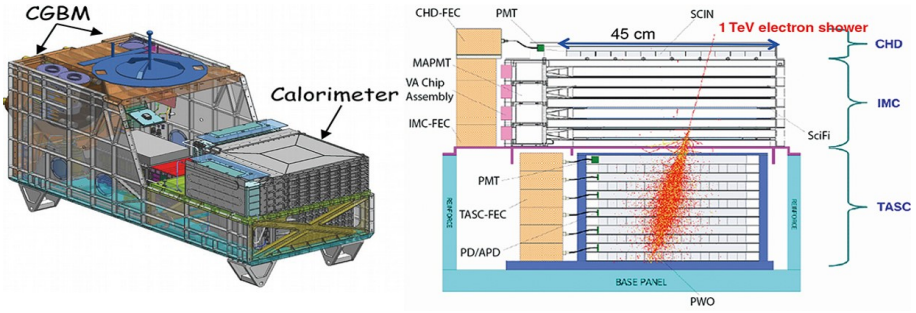

FIGURE 1.8: Left: the schematic view of the CALET with the main calorimeter and the other subsystems. Right: the profile of the CALET calorimeter with an example of the detector response to an electron event with energy of 1 TeV.

CALET

CALET is another high energy astroparticle physics experiment that is installed on the ISS. CALET began to collect data from October 2015. Its major objectives include to measure CR electron + positron spectrum up to few TeVs, and CR nuclei up to hundreds TeV per nucleon. Moreover, searching for high energy gamma ray sources is also one of the main goals of CALET. Up to now, CALET has published its measurements on CR electron + positron and proton fluxes [37, 38].

The detector lay-out of CALET is presented in Fig. 1.8. The major module of CALET is the calorimeter, which is composed by three sub-detectors: the CHarge Detector (CHD), the IMaging Calorimeter (IMC) and the Total AbSorption Calorimeter (TASC). The CHD is used to measure the charge of entering particles [39, 40]. The IMC is an imaging pre-shower detector that can reconstruct the trajectory of entering particles. The energies of particles are measured by TASC. Besides, the TASC can separate the leptons and hadrons as well from their different shower shapes [41].

The proton spectrum with energy from 50 GeV to 10 TeV measured by CALET is presented in Fig. 1.9. The CALET result agrees well with previous measurements at energy below 1 TeV. It confirms the spectral hardening at $\sim$ 300 GeV.

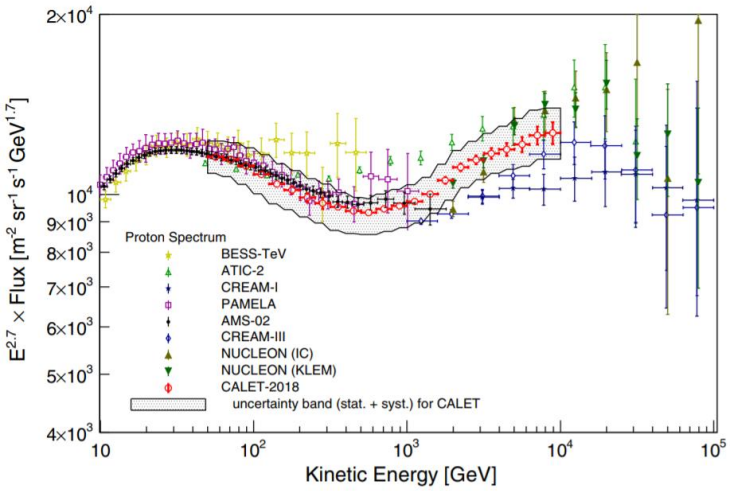

FIGURE 1.9: The CALET proton spectrum with energy from 50 GeV to 10 TeV. The spectrum confirms the spectral hardening at $\sim$ 300 GeV.

DAMPE

DAMPE is a satellite-borne experiment for high energy CR electron, gamma-ray and nuclei. DAMPE is also a calorimeter dominated detectors system, which is similar to CALET. Its scientific goals include to measure CR electron + positron spectrum from few GeV up to 10 TeV, and CR nuclei from few 10 GeV/n up to 100 TeV/n. DAMPE was launched on December 2015 and has been smoothly collecting CR events since then. Due to the fact that this thesis is based on DAMPE data, more details about the DAMPE devices will be described in the following chapters.

The electron + positron spectrum with energy from 25 GeV to 4.6 TeV [42] and the proton spectrum with energy 40 GeV to 100 TeV [6] measured by DAMPE are presented in Fig. 1.10. The significance of the electron + positron spectrum is that it shows for the first time with a direct measurement a spectral break at $\sim$ 0.9 TeV. The DAMPE proton results on one hand confirms the spectral hardening at $\sim$ 300 GeV, and more interestingly, it reveals a spectral softening at $\sim$ 13 TeV with 4.6 σ confidence level. Whether this feature is kinetic energy dependent or rigidity dependent can be studied with helium flux and proton + helium flux measurements. The latter has a larger statistics due to the softer selection criteria, therefore, it provides a reliable cross check on the measured proton flux.

1.3.2 Cosmic ray indirect detection experiments

In this section, the indirect CR detection experiments of Astrophysical Radiation with Ground-based Observatory at YangBaJing (ARGO-YBJ) [43], and the High-Altitude

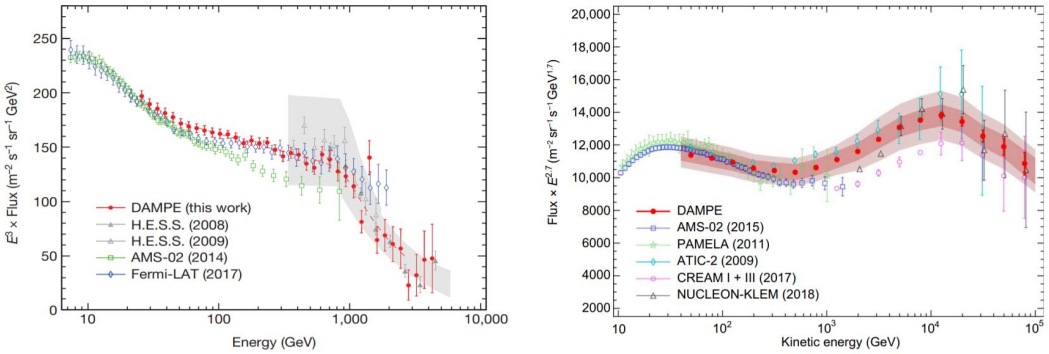

FIGURE 1.10: Left: the CR electron + positron spectrum measured by DAMPE. The red dashed line marks a smoothly broken power-law model that best fits the DAMPE data in the range 55 GeV to 2.63 TeV. The error bars includes both the statistics and the systematic uncertainties. Right: the DAMPE proton spectrum. The error bars only represents the statistical uncertainties, and the inner shadow region represent the systematic uncertainties without considering the effect of different hadronic models, meanwhile the outer shadow region is the total systematic uncertainties.

Water Cherenkov gammma-ray observatory (HAWC) [44, 45] will be introduced since their energy measurement ranges have certain overlaps with DAMPE. Some comparisons between their measurements on CR light nuclei will be made in chapter four.

ARGO-YBJ

The ARGO-YBJ detector array was located at Tibet with an altitude of 4300m. The detector system was composed by a carpet of Resistive Plate Chambers (RPCs) [46]. The total area of the detectors was about 110 × 100 m^2, with central part of 78 × 74 m^2. The detector array is composed by 154 RPCs clusters and each cluster was composed by twelve RPCs (Fig. 1.11). The ARGO-YBJ was able to measure the CR nuclei energy up to several PeVs. The ARGO-YBJ began to take the data from June 2006 and stopped on 2013. The light nuclei (proton + helium) spectra from two publications [47, 48] of ARGO-YBJ collaboration are shown in Fig. 1.12. The uncertainty of absolute energy scale in these measurements are at level of 5-10%.

HAWC

The HAWC observatory is a CR air-shower detector conceived to study the TeV gamma and cosmic ray physics. The detector array is consisted of 300 water Cherenkov tanks. Each tank is with dimension of 4.5 m deep and 7.3 m diameter. There are 4 PMTs for every tank as the signal readout device. The tanks are distributed on an area of 22000 m^2 in Sierra Negra, Mexico. The profile of the HAWC tanks distribution and the diagram of a tank are presented in Fig. 1.13.

The HAWC all-particles spectrum from 10 TeV to 500 TeV is presented in Fig. 1.14. The data taking period for this spectrum is from June 2016 to February 2017 [49].

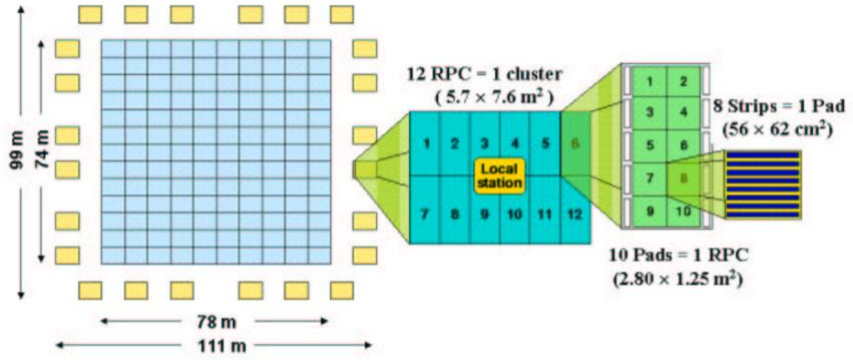

FIGURE 1.11: The profile of the ARGO-YBJ in vertical view. There are 130 clusters in the center part, and another 24 clusters at the four sides of the center part. Each cluster contains twelve RPCs, each RPC contains ten pads and each pad is composed by eight aluminum strips.

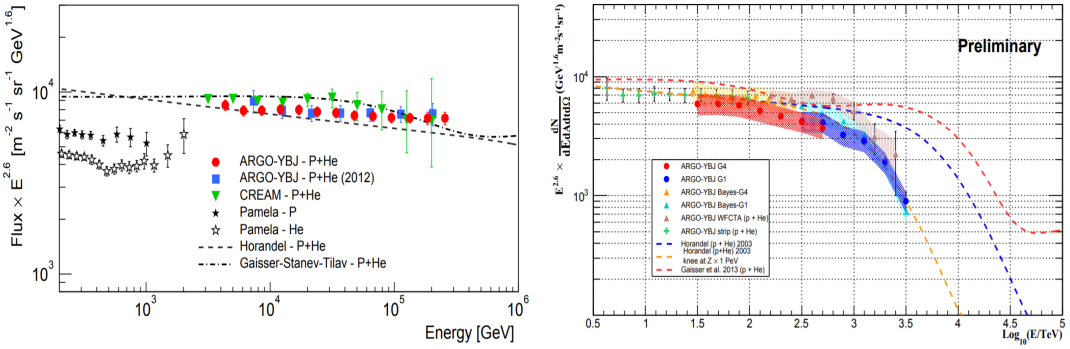

FIGURE 1.12: Left: The light component of CR spectrum with energy from 3 TeV up to 300 TeV measured by the ARGO-YBJ experiment (red points). A previous measurement performed by ARGOYBJ in a narrower energy range by analyzing a smaller data sample is also reported (blue squares) [2]. Right: The Light component CR energy spectrum with energy from 30 TeV to 5 PeV measured by ARGO-YBJ with four different analyses.

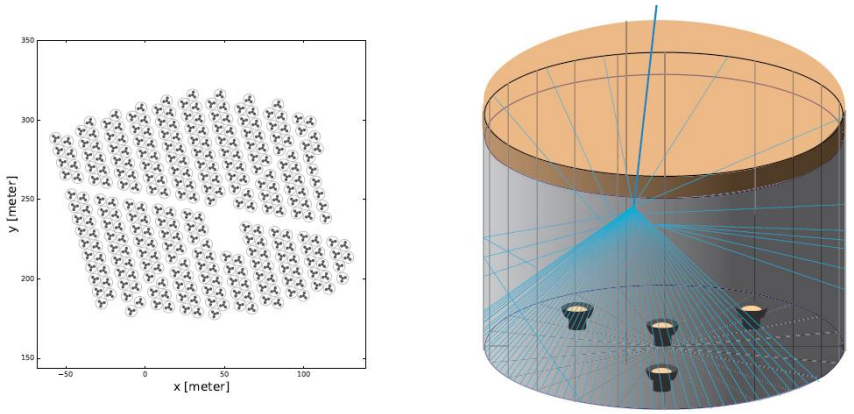

FIGURE 1.13: Left: The HAWC profile in vertical view. There are 300 water tanks in total. Right: a diagram of one tank and its response to an entering particle.

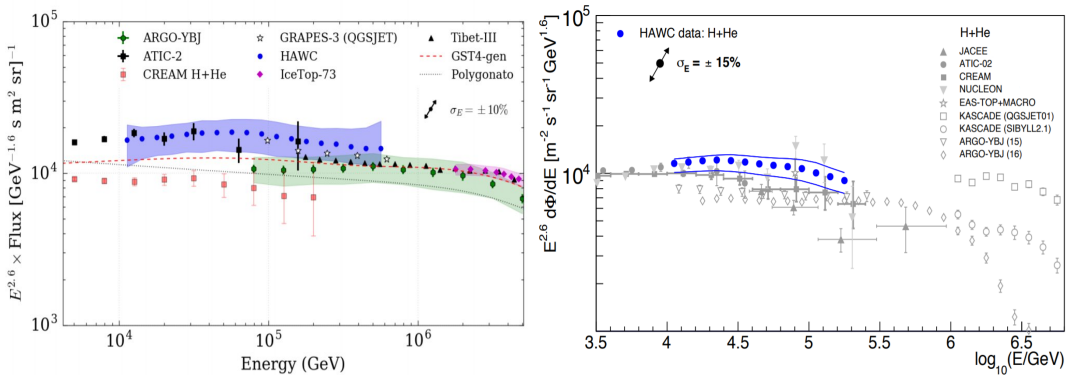

FIGURE 1.14: Left: The HAWC all-particle spectrum. The blue shadow region represents the systematic uncertainties. The double-sided arrow indicates a flux shift might happen due to a ±10% shift in the energy scale. Right: The HAWC proton + helium spectrum. The data taking time for this spectrum is from June 2015 to November 2018. The statistics error is shaded by the data points, and the blue lines on both sides of the data points mark the systematic errors. The double-sided arrow indicates a flux shift might happen due to a ±15% shift in the energy scale.

In 2019, HAWC collaboration presented their proton + helium spectrum in the 36th International Cosmic Ray Conference (ICRC 2019). The spectrum is also plotted in 1.14. The light components spectrum shows that a spectral softening exists at energy of $\sim$ 31 TeV, where the spectral index changes from -2.53 to -2.79 [50].

Given these previous CR measurements, it seems that the feature of CR spectrum can not be well described by a single power law. The subtle spectral features need to be studied by more precise measurements. The measurement of proton + helium spectrum with DAMPE can achieve this goal. In the following chapters, the DAMPE equipment is firstly introduced, then the data analysis procedures for measuring proton + helium spectrum will be described.

Chapter 2

The Dark Matter Particle Explorer

The DAMPE (Dark Matter Particle Explorer), also know as "Wukong" in China, is a state of the art space experiment for direct detection of high energy cosmic rays, electrons and gamma rays [26, 51]. DAMPE was successfully launched on 17th December 2015 in Jiuchuan launch center of China, and has been working smoothly since then. DAMPE has the potential to extend our knowledge on cosmic ray electrons/positrons, nuclei and gamma-ray astronomy to a new level. Some insights results have already been published (as presented in chapter one). In this chapter, we will introduce the DAMPE mission. In section 2.1, the scientific goals and the general parameters of DAMPE will be presented. In section 2.2, each individual sub-detector of DAMPE and their calibration work will be described. The trigger and the data acquisition system will be introduced in section 2.3. In the last section (2.4), we will briefly present the coordinate system of DAMPE.

2.1 Scientific objectives and parameters of DAMPE

The setup of DAMPE make it a multifunctional detector which can be used to study various topics related to astroparticle physics and astronomy. DAMPE is located on a sun-synchronous orbit with an altitude of 500 km, it can observe the full sky four times in two years [26]. The main scientific goals of DAMPE include:

1. Search for the signature of the dark matter particles. According to the current models[52, 53], the annihilation and decay of dark matter particles may produce gamma-rays, electron/positron pairs which can be detected by DAMPE. By using

this indirect detection method, DAMPE has the potential to measure the rest mass and the annihilation cross section of dark matter particles.

2. Measure the spectrum of CR nuclei and electrons and study the mechanism of CR acceleration and propagation.

3. Observe high energy gamma-rays up to 10 TeV. DAMPE can monitor high energy gamma-ray sources such as supernova remnants, pulsars and study the radiation mechanisms and the related physical processes.

DAMPE was conceived with wide energy observation range and large acceptance to meet the requirements for achieving its scientific goals. The energy resolution is also improved compared with the precedent space-borne CR experiments to guarantee a more accurate measurement. In Tbl. 2.1, the main instrument parameters of DAMPE are presented.

Parameters	Values
Energy range for gamma-rays and electrons	5GeV - 10 TeV
Energy resolution for gamma-rays and electrons	$\leq$ 1.5% at 800 GeV
Energy range for nuclei	50 GeV/n - 100 TeV/n
Energy resolution for nuclei	$\leq$ 40% at 800 GeV
Geometric factor for electrons	$0.3\text{m}^2 \cdot \text{sr}$ above 30 GeV
Geometric factor for protons	$0.04\text{m}^2 \cdot \text{sr}$ above 100 GeV
Angular resolution for photons	$\leq$ 0.2° at 100 GeV
Field of View	$\sim$ 1.0 sr

TABLE 2.1: The main instrument parameters of DAMPE.

Comparing with other experiments, DAMPE has advantages on the energy measurement range and resolutions. In Tbl. 2.2, the measurements on electron are used as an example to compare the detector parameters among several space-borne experiments.

Experiments (Launch time)	Energy range ($e^{\pm}$)	Energy resolution ($e^{\pm}$)	Acceptance ($e^{\pm}$) $\text{m}^2 \cdot \text{sr}$
Fermi-LAT (2008)	0.1 GeV - 300 GeV	5%-15%	$\sim$ 1
AMS-02 (2011)	0.5 GeV - 1 TeV	2%	0.055
CALET (2015)	5 GeV - 10 TeV	3%	0.1
DAMPE (2015)	5 GeV - 10 TeV	1.5%	0.3

TABLE 2.2: The comparison of the parameters on electron measurement among the space-borne experiments.

DAMPE is in operation in a sun synchronous orbit, it was equipped with a temperature regularization system to guarantee a stable environment temperature. Thus the impact of the temperature changing on the instruments is negligible [54]. Some of the orbit parameters of DAMPE are shown in Tbl. 2.3.

Orbit parameters	Values
Name	sun synchronous orbit
Height	500 km
Tilt angle	97.4°
Eccentricity	0
Time for one circle	95 mins

TABLE 2.3: The main parameters of DAMPE orbit.

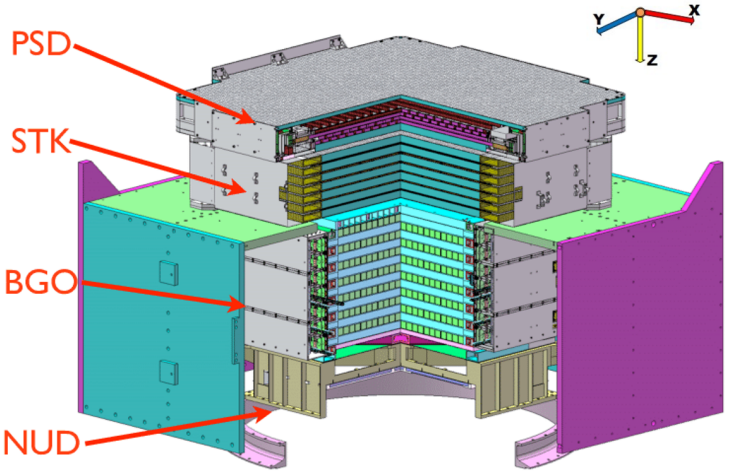

FIGURE 2.1: The layout of DAMPE. The red parts are the two payers of the PSD.

2.2 The DAMPE instrument

DAMPE is consisted of four sub-detectors. The layout of DAMPE is shown in Fig. 2.1, from top to bottom, there are: the Plastic Scintillator Detector (PSD) [55], the Silicon-Tungsten tracKer detector(STK) [56], the Bismuth Germanium Oxide imaging calorimeter (BGO) [57] and the NeUtron Detector (NUD) [58]. The PSD is responsible for the charge measurement and identification between gamma-rays and electrons. The STK is in charge of reconstructing the track of entering particles. Besides, the STK can measure the charge of particles with $Z < 9$ as well. The BGO calorimeter is used to measure the energy of the entering particles and distinguish the protons and electrons by looking at their shower shapes. The NUD is used to collected neutrons generated from the hadronic shower in the BGO, thus the identification power between protons and electrons can be enhanced. Each of the sub-detector will be introduced in the following sub-sections.

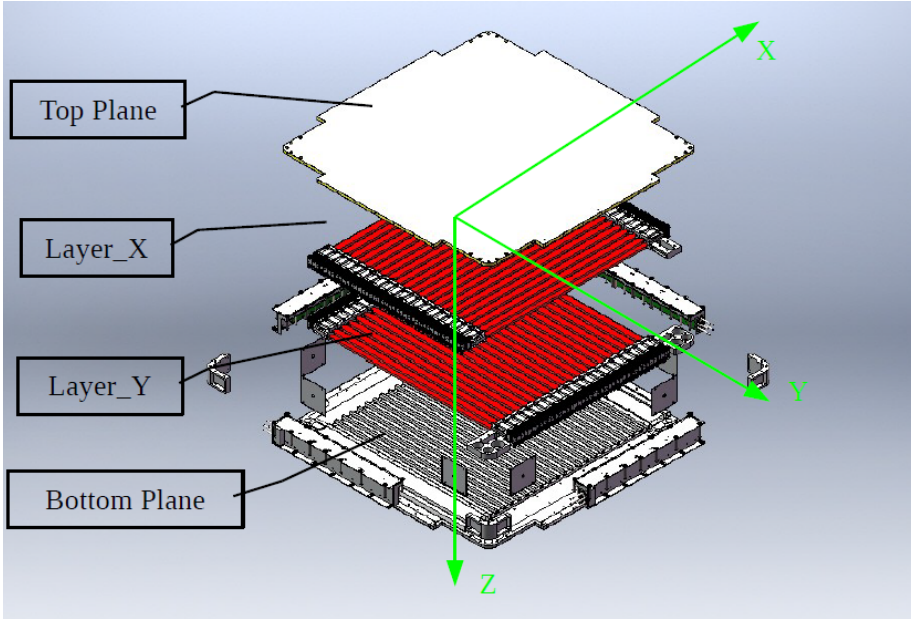

FIGURE 2.2: The layout of the PSD. The red parts are the two lays of the PSD.

2.2.1 The Plastic Scintillator Detector

The PSD is responsible for the measurement of the charge and works as an anti-coincidence detector for the gamma-rays as well. The structure of the PSD is shown in Fig. 2.2. The PSD is composed by two sub-layers of plastic scintillator bars. The PSD bars in one layer are perpendicular to the bars in the other layer, which follow the X and Y axis of the DAMPE coordinate system respectively. Each layer includes 41 bars, and each bar has two PMTs at its both ends as readout instrument for the signals. The bar and its affiliated PMTs make the basic detection module for the PSD. In total, the PSD includes 82 detection modules. In Fig. 2.3, a basic module of the PSD is presented. Moreover, in order to avoid the inefficient detection region (the gap between the adjacent bars), the adjacent modules in one layer are staggered by 8 mm. A side view on the arrangement of the PSD modules is plotted in Fig. 2.4. The size of one PSD bar is 88.4 cm $\times$ 2.8 cm $\times$ 1 cm. The total active detection area for the PSD is 82.5 cm $\times$ 82.5 cm.

There are high demands on the PSD for its detection efficiency and charge resolution due to the important role the PSD plays in DAMPE. Therefore, the PSD is performed various tests regarding its detection efficiency, charge reconstruction ability, and charge resolution etc, before DAMPE was launched. The test result for the detection efficiency shows that for a single module of the PSD, the detection efficiency can reach 95% [1]. Due to the fact that the PSD has two layers, some more precisely tests described in [55]

[1]The detection efficiency is defined as the ratio of the number of the detected events over the number of total events that pass through the PSD.

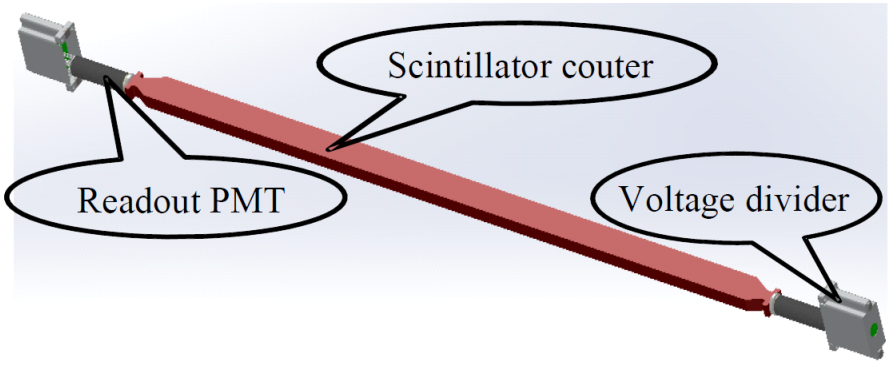

FIGURE 2.3: The basic detection module for the PSD.

FIGURE 2.4: The side view of the PSD modules arrangement.

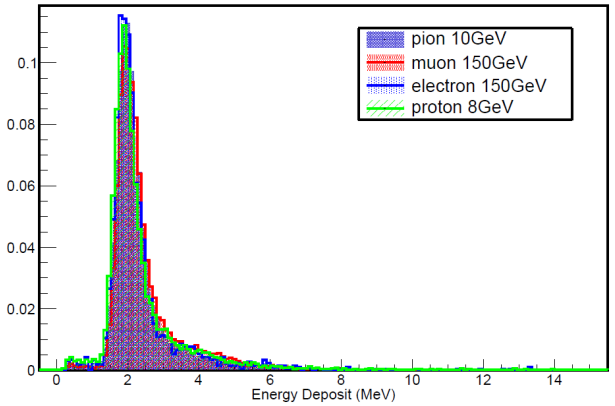

FIGURE 2.5: The measurement on different kinds of particles with Z =1 by the PSD. The counts for each kind of the particle have been normalized.

show that the detection efficiency can be better than 99%. For the charge measurement capacity, the PSD has the charge resolution better than 25% for particles with Z = 1. In Fig. 2.5, the PSD measurement on different particles with common charge of Z = 1 is presented. The PSD can precisely measure the charge of the particles despite the difference of their categories and primary energies.

An important issue about the PSD is the light attenuation. The number of photons produced by interactions between entering particles and PSD bar molecules will attenuate during the propagation to PMTs. This phenomenon leads to a hit-position dependent measurement of the PSD. For example, in Fig. 2.6, the measured CR muon signals (represented by ADC channels) by a PSD module in terms of their hit positions at the bar are presented [59]. The distributions of the ADC regarding each bin of the hit position are fitted with Landau functions. The black triangles marks the Most Probable Vales

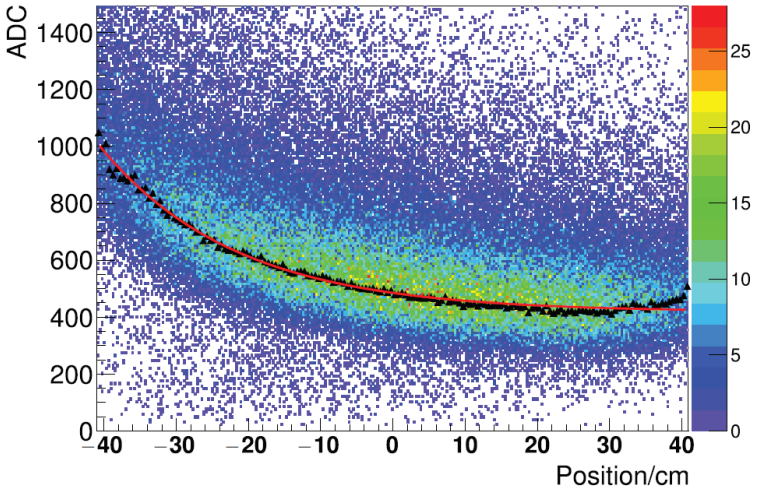

FIGURE 2.6: The ADC channels regarding the hit positions for the muon measurement with a PSD module. The black triangle represents the MPV of the distribution for each position bin. The red line is the best fit of the MPVs regarding hit positions.

(MPVs) of the distributions for each bin. Then the MPVs are fitted as a function of their hit positions as:

$$A(x) = C_0 e^{-x/\lambda} + C_1 x + C_2 x^2 + C_3 x^3 \ , \tag{2.1}$$

where A(x) is the ADC value of the MPV of the event distribution. The λ, C_0, C_1, C_2, C_3 are free parameters waiting to be estimated. x represents the hit position. It can be noticed from the fit function (the red line in Fig. 2.6) that the output signals of the PSD depend on the entering position. With the parameters obtained from the fit function, a correction can be made to have a measurement which is independent from the hit position for an event. The hit positions can be derived from the extrapolation of reconstructed tracks by the STK in practice. In Fig. 2.7, the measured charges of some CR nuclei regarding the hit positions after the correction are presented. In this case the charge for a certain element is nearly a constant which implies the independence of the PSD measurement from the particle hit positions.

Moreover, the effect of different incident angles on PSD signals must be corrected, due to the fact that different incident angles indicate a different path length in the PSD bar and results in different signal amplitudes. The charge of an entering particle must be precisely measured regardless of the particle entering position and angle on a PSD bar. Therefore, a correction is necessary. The final corrected charge measured by PSD should be [59]:

$$Q_{rec} = \sqrt{E_{raw}/A(x) \times D/s} \ , \tag{2.2}$$

where Q_{rec} represents the reconstructed charge of an event, E_{raw} is the raw energy loss measured by the PSD, A(x) is the attenuation function, s is the path length in a PSD

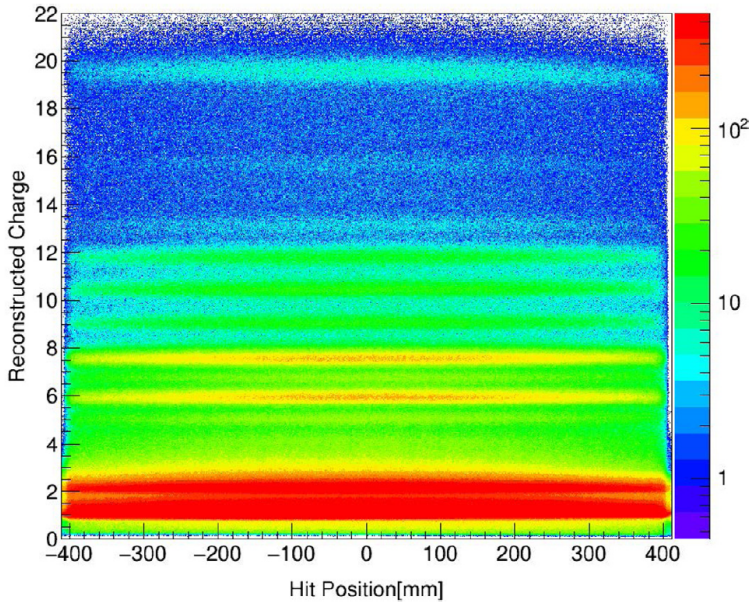

FIGURE 2.7: After the light attenuation correction, the measured charge for various CR nuclei by the PSD regarding the hit positions.

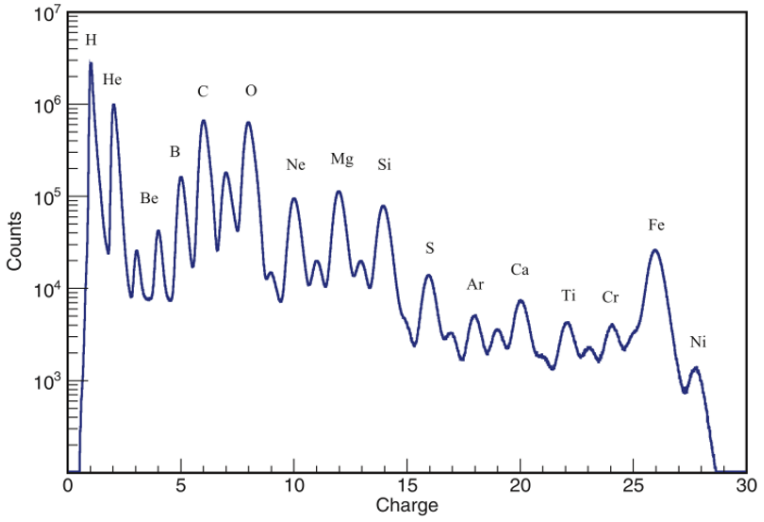

FIGURE 2.8: The charge spectrum reconstructed by the PSD by using of three years of the on-orbit DAMPE data.

bar, D equals to 10 cm, which is the thickness of a PSD bar. The Q_{rec} equals the square root of the reconstructed energy loss, this is due to the well known Bethe-Bloch formula [60] which indicates that the deposit energy of an entering particle in a PSD bar should be proportional to Z^2 of the particle.

After performing the correction on the light attenuation and incident angles (also the quenching effect [61]), the reconstructed charge spectrum with PSD based on three years of on-orbit data is present in Fig. 2.8. The peak for each element (up to Ni) can be easily recognized, which demonstrates the powerful capability on the charge identification of the PSD.

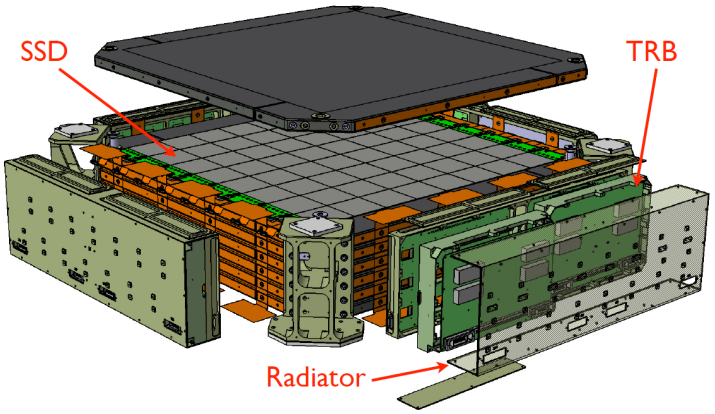

FIGURE 2.9: The exploded view of the STK.

2.2.2 The Silicon-Tungsten Tracker Detector

The STK is in charge of reconstructing the track of entering particles and converting gamma-rays into electron/positron pairs. A similar approach has been used in Fermi and AGILE experiments [62, 63]. Moreover, the STK can measure the charge of nuclei with $Z < 9$ as well [56, 64].

The STK is composed by six planes, each of the plane includes two orthogonal layers that is used to measure the X and Y coordinates of a charge particle separately. The structure of the STK is presented in Fig. 2.9. The basic module of the STK is the ladder (shown in Fig. 2.10), which includes 4 Silicon micro-Strip Detector (SSD) manufactured by Hamamastu Photonics [65]. The dimension of a SSD is $95 \times 95 \times 0.32$ mm^3, and each SSD has 768 p^+-strips implanted in the n-doped bulk [56]. A STK strip has a width of 48 μm, a length of 93.196 mm and a pitch of 121 μm. Two adjacent SSDs in one ladder are bounded as the way shown in Fig. 2.11. Every other strip is readout by a VA160 chip [66] installed at the extremity of the ladder. There are 384 readout channels with a pitch of 242 μm for a ladder. Each layer of the STK includes sixteen ladders, in total there are 192 ladders. The ladders are assigned to seven support trays to compose the twelves layers of the STK. The top and bottom trays are equipped with the ladders only on one side, meanwhile the other five trays are equipped on both sides. The Tracker Readout Board (TRB), mounted at the flank of the trays, is used for signal readout. Each TRB is responsible for 24 ladders, there are in total eight TRBs distributed on the four flanks of STK (two TRBs at each flank).

A Kalman filter algorithm [67] is used to reconstruct the tracks of incident particles. For the reconstruction, a hit cluster is first recognized to be the basis of the algorithm. The cluster is defined as a group of STK channels with one channel having signal-to-noise ratio larger than four, and its neighbor channels having signal-to-noise ratio larger than 1.5. The hit coordinate can be derived from the cluster. Both the charge and track

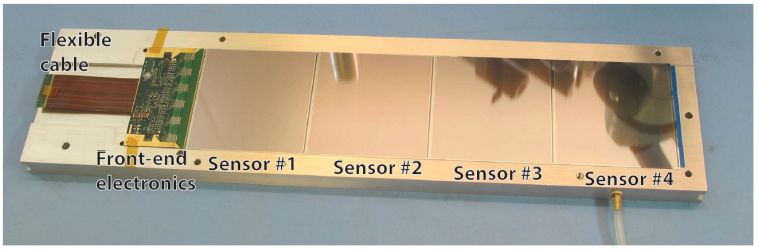

FIGURE 2.10: The detector ladder of the STK, which is compsed by four SSD. Six VA160 chips are installed at the end as the main components of the Front-end electrons.

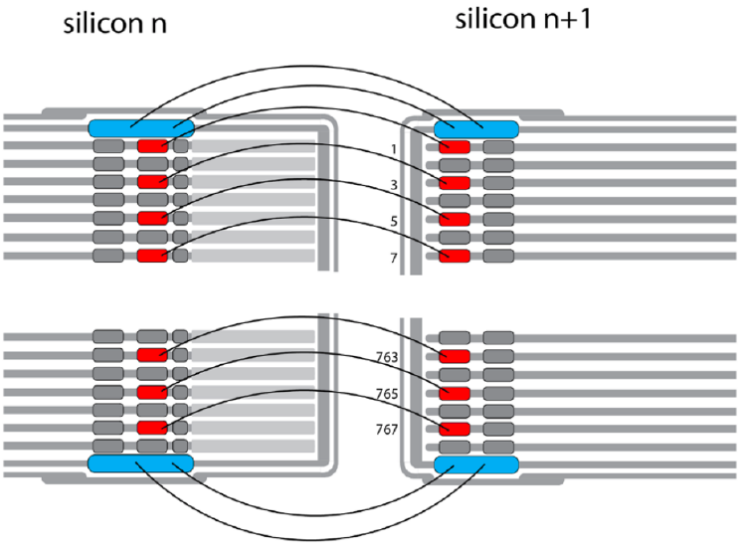

FIGURE 2.11: The way for bonding the adjacent SSDs.

reconstruction of the STK are based on the cluster. More details of the algorithms for finding the cluster can be found in [3].

The cluster is essentially a group of fired strips. The amplitudes of the signals from all the fired strip channels of the cluster are summed up to reconstruct the charge from a cluster. An example of the measurement on some singly charged particles regarding their ADC channels is presented in the left of Fig. 2.12 where two peaks can be found. This is due to the fact that the readout of a signal is done every other strips. When the particle hit the strip of the readout channel perpendicularly, almost 100% of its deposit energy can be collected. Meanwhile, if the hit strip is the floating one (non-readout one), only 65% of its deposit energy can be collected [26]. Therefore, the peak with lower ADC channels in the left of Fig. 2.12 comes from the events hitting the floating strip. Meanwhile the events passing through the readout strip lead to the peak with larger ADC values. The energy loss measurement can be corrected according to the incident angles and the hit positions [56]. On the right of Fig. 2.12, the same data set but with the correction on the energy measurement of the floating strip are presented.

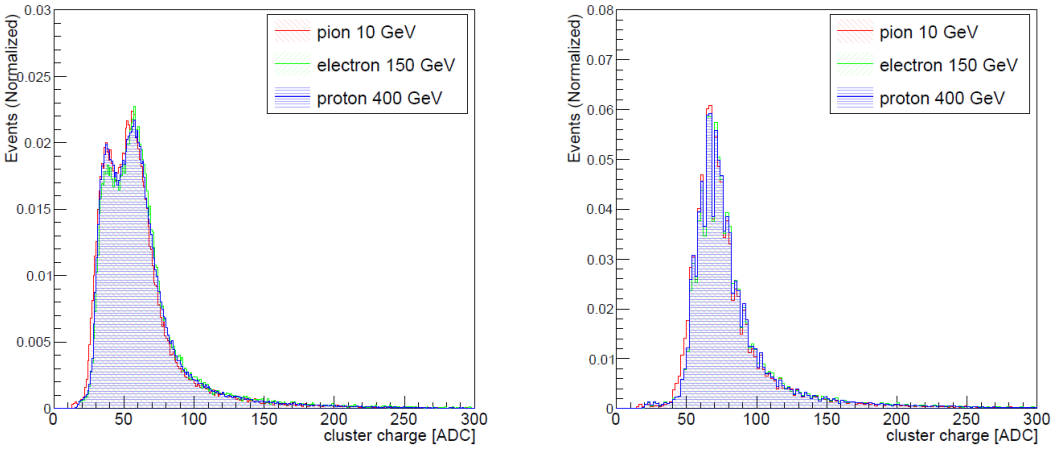

FIGURE 2.12: Measurements on various singly charged particles performed by a STK ladder, before (left) and after (right) the correction on the energy loss of floating strip.

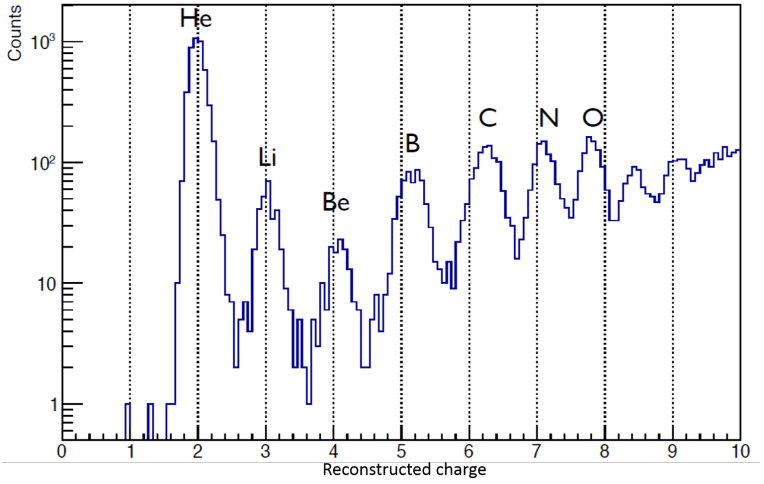

FIGURE 2.13: The reconstructed charge spectrum for the nuclei produced by the spallation of a lead beam. Singly charged particles have been removed.

The identification power on non-singly charged particles of the STK has been tested in CERN by using of a lead beam hitting a target and producing various nuclei due to nuclear spallation. The secondary beam is collected by a ladder of STK, and the charge of the nuclei is reconstructed as $\sqrt{\sum_{i=1}^{n} ADC_i/ADC_{MIP}/n}$ with ADC_i represents ADC counts of i-th cluster after the energy correction, the ADC_{MIP} is the mean ADC value of Minimum Ionization Particle distribution in the ladder. The number of the clusters is n. The signal amplitude in the form of ADC counts are scaled into the energy by using this transformation. The reconstructed charge spectrum is presented in Fig. 2.13. The nuclei can be easily recognized up to oxygen (Z=8).

To estimate the position resolution of the STK, a residual value is defined as the difference between the measured position and the projection of the track in a certain layer where the track is reconstructed without using the cluster in that layer. Moreover,

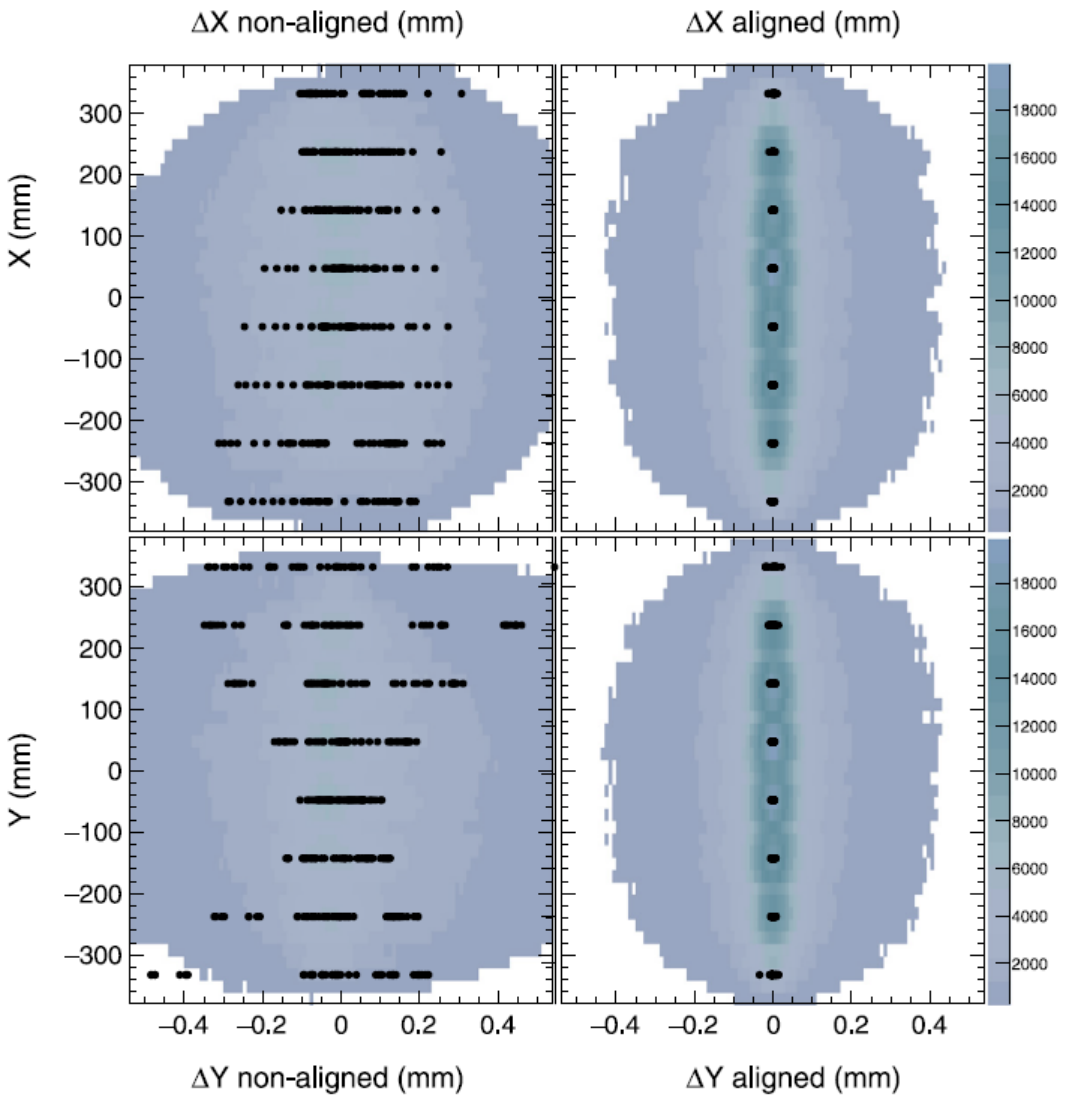

FIGURE 2.14: The residual values of X and Y direction layers before (left) and after (right) the alignment correction. The black circles represent the mean values of the residual distributions of the SSDs.

an alignment algorithm is used to correct the displacement and rotation of each SSDs regarding their nominal positions [3, 68]. In Fig. 2.14, the effect of the alignment correction is presented with ΔX represents the residual value of X direction layer and ΔY for the same of Y direction layer. After the alignment, the residual values are more compact around zero, which implies a better resolution for the position measurement.

The distribution of the residual value for a SSD can be fitted with a Gaussian function. The sigma of the fitting result reflects the position resolution. In Fig. 2.15, the distributions (fitted with a Gaussian function) of the residual value with two different incident angles are presented. The position resolutions for each layers regarding different angles are presented in Fig. 2.16 where the MC simulation is shown as well [3]. After the

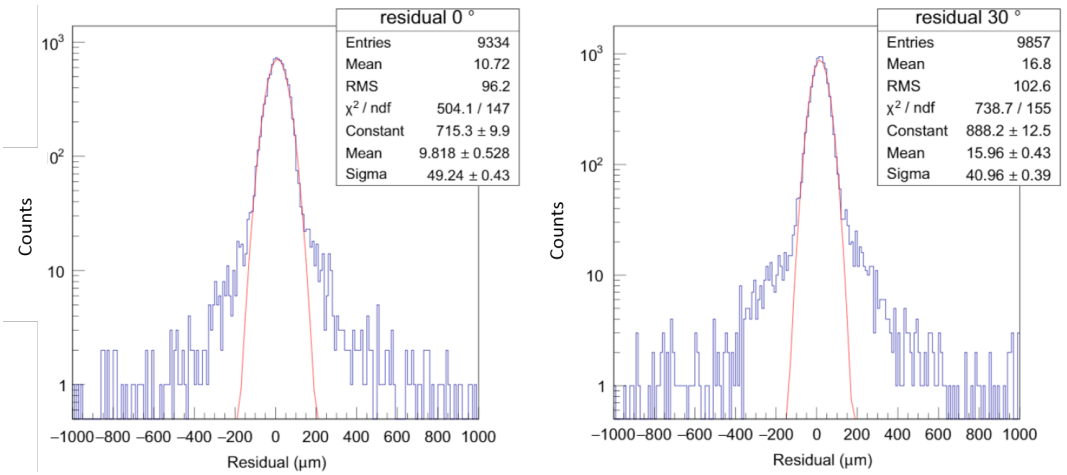

FIGURE 2.15: The distributions of the residual values for the two different incident angles.

alignment correction, the position resolutions of most of the STK layers is better than 60 μm, which is in agreement with the MC simulation.

2.2.3 The Bismuth Germanium Oxide imaging calorimeter

The BGO calorimeter is located below the STK in the DAMPE system. The BGO has three primary purposes: 1) to measure the energy of an incident particle; 2) to distinguish lepton and hadron events by using their 3D profile images of the shower; 3) to offer the 0-level trigger for the data acquisition system [26, 69, 70].

The BGO is composed by 14 layers of the bismuth germanium oxide bars and each layer has 22 bars. The directions of the bars are arranged following the X and Y axis of the DAMPE coordinate system. Each BGO bar is in dimension of 25 × 25 × 600 mm with both ends coupled by a PMT produced by Hamamatsu [65] as the read-out device. The layout of the BGO calorimeter is presented in Fig. 2.17. The main parameters of the BGO is presented in Tbl. 2.4

Parameters	Values
Active area	60 cm × 60 cm
Depth	32 radiation lengths
Sampling	$\leq$ 90%
Longitudinal segmentation	14 layers ($\sim$ 2.3 radiation length each)
Lateral segmentation	1 Moliere radius

TABLE 2.4: The conceived parameters of the BGO.

In order to perform a large range of the energy measurement. The signals from an event are read out by three different dynodes of a PMT: Dy2, Dy5 and Dy8. The final readout

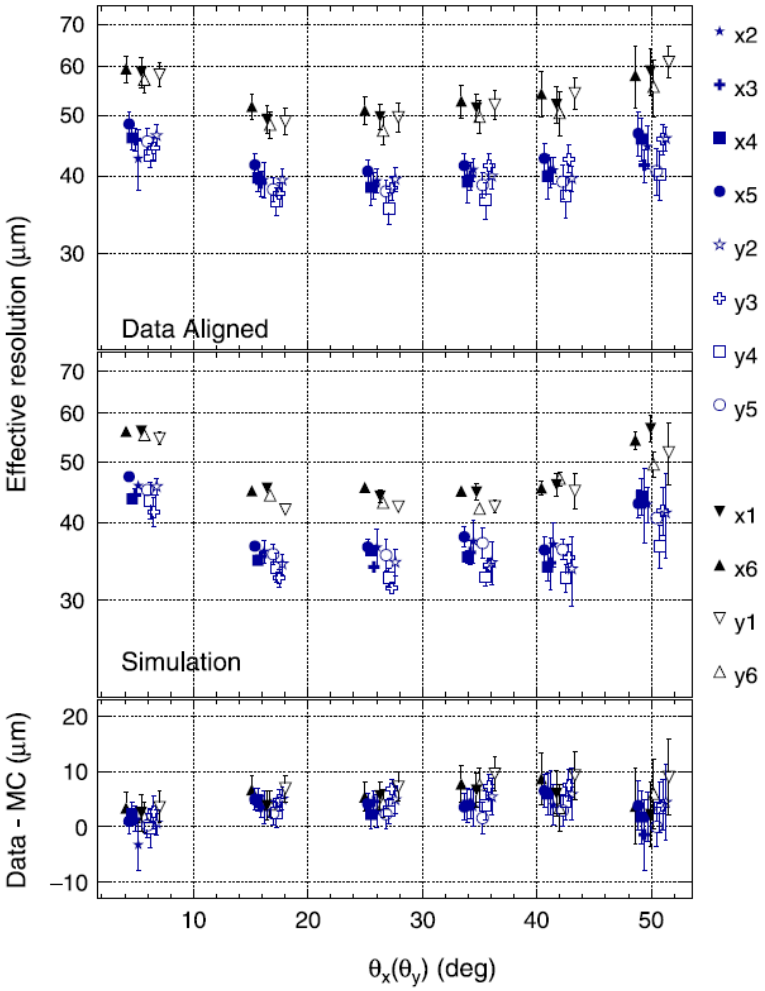

FIGURE 2.16: The effective spatial resolution of the STK layers regarding different incident angles. The error bars of the data include the statistics uncertainty and the systematic uncertainty due to the on-orbit variation of the alignment and multiple scattering summed in quadrature [3]. The error bars in MC only include the statistics uncertainty.

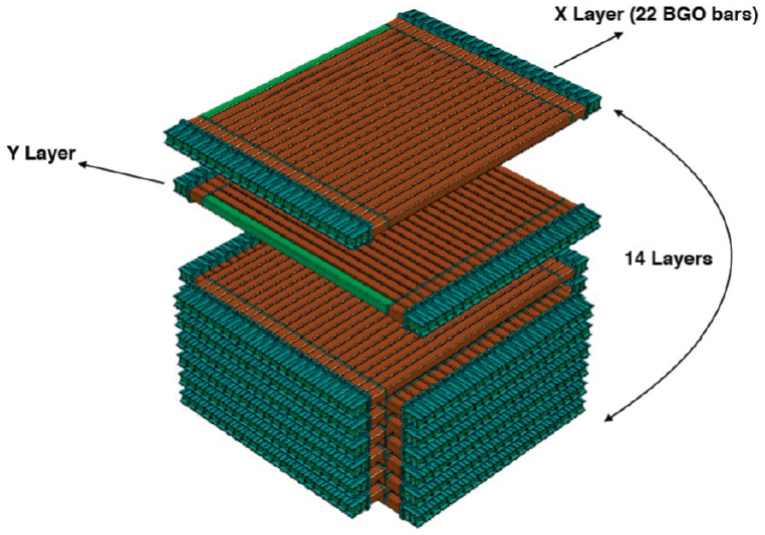

FIGURE 2.17: The layout of the BGO calorimeter.

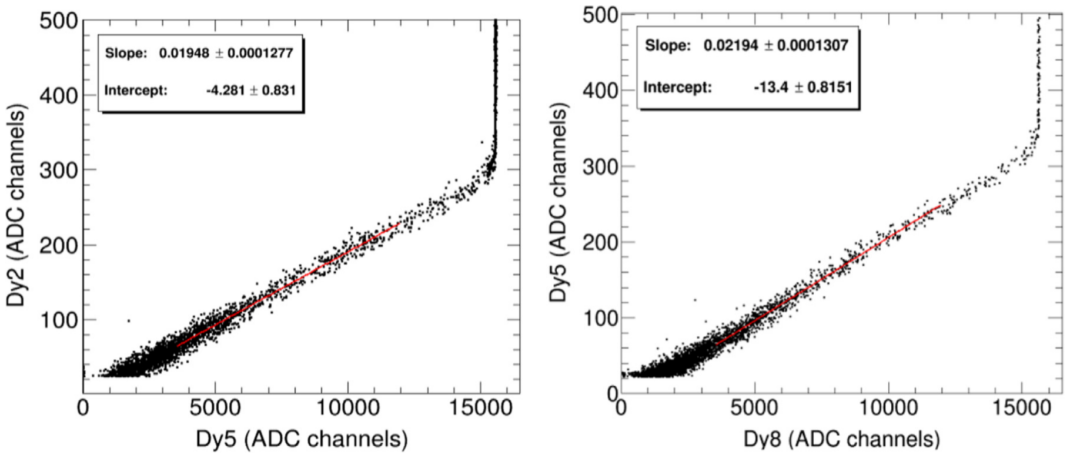

FIGURE 2.18: The relation for different dynode readout signals of a PMT. The left one is for the Dy2-Dy5 relation, and the right one is for the Dy5-Dy8 relation. The slopes are around 0.02.

signals (ADC channels) are decided as:

$$\mathrm{ADC} = \begin{cases} \mathrm{Dy8} & \mathrm{Dy8} \leq 12000 \\ \mathrm{K_1} \times \mathrm{Dy5} + \mathrm{C_1} & \mathrm{Dy8} > 12000 \text{ and } \mathrm{Dy5} \leq 12000 \\ (\mathrm{K_2} \times \mathrm{Dy2} + \mathrm{C_2}) \times \mathrm{K_1} + \mathrm{C_1} & \mathrm{Dy5} > 12000 \end{cases}, \tag{2.3}$$

where $\mathrm{K_1}$, $\mathrm{C_1}$ represent the slope and intercept of the relation function between Dy8 and Dy5. The same holds for the $\mathrm{K_2}$, $\mathrm{C_2}$ for Dy5 and Dy2. The 12000 is choosen as the threshold to change the readout dynode since the saturation effect becomes significant when the ADC channels is larger than that in a dynode. The relation of the signal amplitude of Dy5-Dy8 and Dy2-Dy5 from a PMT are presented in Fig. 2.18.

The signals is in form of ADC channels by using of the equation 2.3. Therefore, an energy scale calibration is necessary to obtain a signal with standard energy unit. This work is fulfilled by referring to the MIP distribution of each BGO bar. More details of the calibration procedure can be found in [59].

Since measuring CR nuclei is one of the main goals of DAMPE, the performance of the BGO in measuring the hadronic particles energy plays an important role. The capability of the BGO on measuring the hadron energy was tested in CERN with proton beams. Due to the large uncertainties for a hadronic shower process, a special energy reconstruction algorithm is needed to unfold the detector response and obtain the primary energies of entering particles. More details about the unfolding algorithm will be introduced in chapter three. The deposited energies and reconstructed energies for various proton beam data are plotted in Fig. 2.19. The reconstructed energy distributions have the mean values which are in agreement with the true energies of the beams.

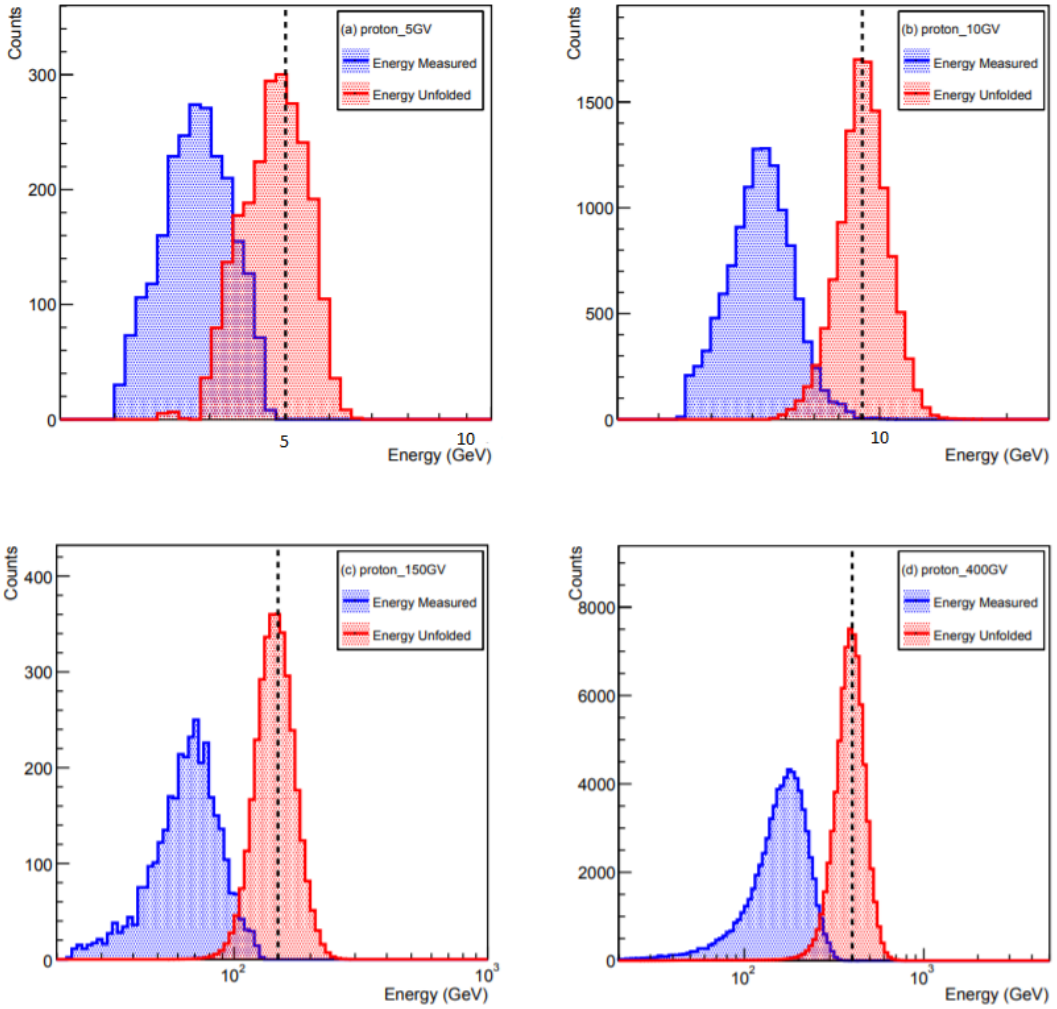

FIGURE 2.19: The measured energies by the BGO and reconstructed energies by the unfolding algorithm for proton beam with various primary energies.

The energy resolution, defined as σ/E_{mean}, of the BGO is also studied by using of both MC simulation and the beam data. In Fig. 2.20, the energy resolution for protons as a function of their energy is presented. The available beam data are in agreement with the simulation. The simulation shows that the resolution varies from 10% at few 10 GeVs to 30% at 100 TeV. The simulation is fulfilled by the GEANT4 toolkit [71].

The BGO calorimeter can reconstruct the track of entering particles as well with a limited spatial resolution. The reconstruction procedures are based on the cluster of fired bars in each layer of the BGO. The search for a BGO cluster in a layer starts from the bar with maximum energy and then extend to its neighboring bars on both side. The extrapolation on the bars for finding a cluster will stop when: 1) the edge of the layer is reached; 2) a non-fired bar is found; 3) a bar with deposit energy larger than its precedent neighboring bar is found. Moreover, the cluster must be symmetric, which means that if the extrapolation process on one side is stopped, the same has also to be done on the other side even without meeting the three conditions above. Only one

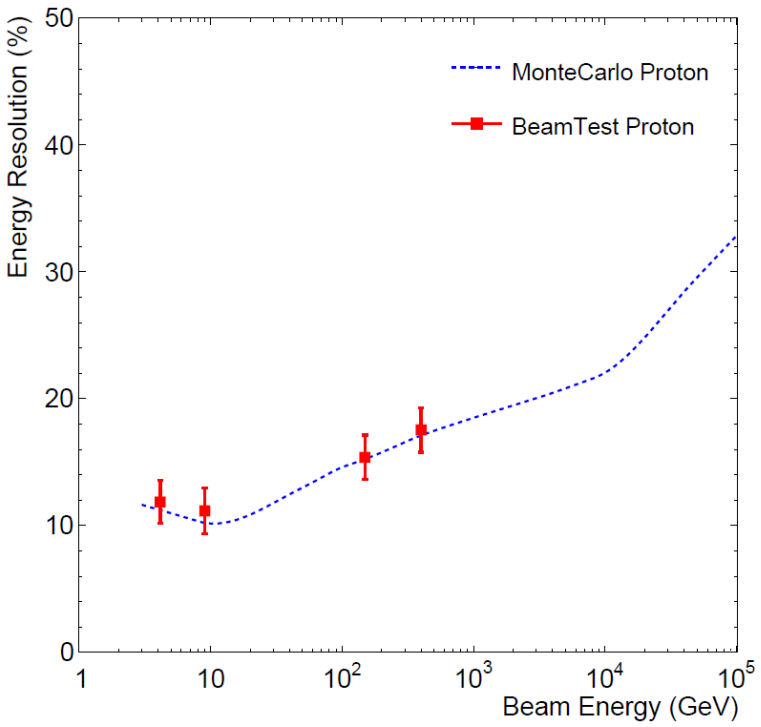

FIGURE 2.20: The BGO energy resolution for proton measurement, the dash line is the simulation, and the red points are the available beam data results.

cluster is allowed for each layer. After the size of the cluster is determined, a Center of Gravity (CoG) is defined as the sum of center coordinate of each bar in the cluster weighted with their deposited energies and divided by the sum of the deposit energies. For instance, if there are three bars in the cluster, the CoG for X (or Y) coordinate in i-th layer can be derived as:

$$\mathrm{X(Y)_{CoG_i}} = \frac{\mathrm{E_{max-1}} \cdot \mathrm{X(Y)_{max-1}} + \mathrm{E_{max}} \cdot \mathrm{X(Y)_{max}} + \mathrm{E_{max+1}} \cdot \mathrm{X(Y)_{max+1}}}{\mathrm{E_{max-1}} + \mathrm{E_{max}} + \mathrm{E_{max+1}}} , \qquad (2.4)$$

where $\mathrm{E_{max}}$ is the maximum deposit energy and $\mathrm{X(Y)_{max}}$ is the center X(Y) coordinate of the corresponding bar, $\mathrm{E_{max\pm1}}$ and $\mathrm{X(Y)_{max\pm1}}$ are the deposit energies and X(Y) coordinate of the neighboring two bars respectively. The track is obtained by fitting the CoG of each layer [26]. The reconstructed BGO track will be used as the reference to select the STK track (see chapter four). In Fig. 2.21, an example is shown on the track selection work: There are several tracks that can be reconstructed by using the STK, in order to determine which one is the best track, the BGO track can be used to match with the STK track.

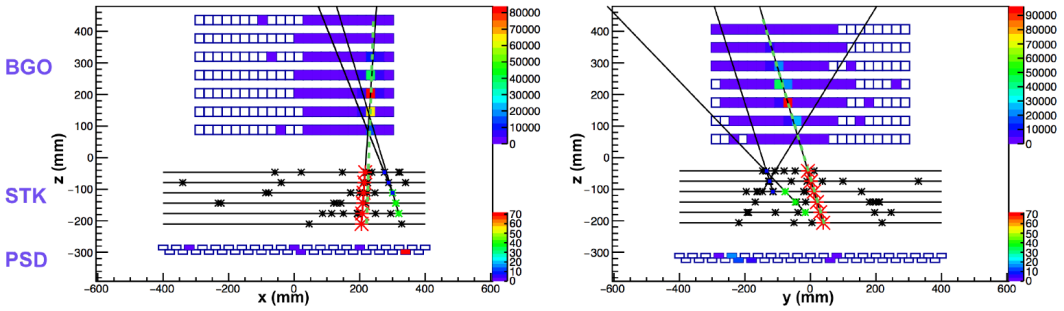

FIGURE 2.21: An example of the reconstructed tracks for an event by BGO and STK on both XZ view (left) and YZ view (right). The green dash line is the track from the BGO extrapolated to STK, the black lines are from the STK alone. The best track of the STK can be determined as the one that is closest to the BGO track.

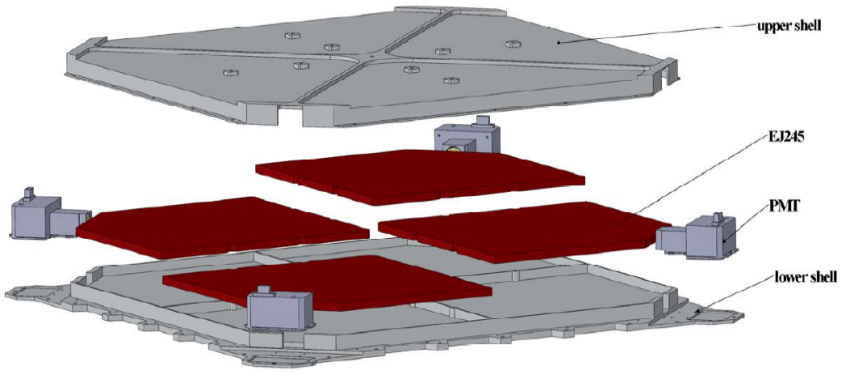

FIGURE 2.22: The layout of the neutron detector.

2.2.4 The Neutron Detector

The NUD is located below the BGO calorimeter, which is at bottom of DAMPE system. The purpose of the NUD is to detect the neutrons produced by the hadronic shower initialized in the BGO calorimeter, which could be used to enhance the capacity for identifying the electromagnetic and hadronic showers. The NUD is composed by four blocks of plastic scintillators doped with ^{10}B nuclei [58]. Boron accounts for 5% of the total weight of the scintillator tiles. Four PMTs are installed at the four corners of the NUD for the readout of the signals. The layout of the NUD is shown in Fig. 2.22.

The neutron capture process is the dominant source for generating scintillation light. When a neutron reach the NUD, it will interact with the NUD as:

$$^{10}\mathrm{B} + \mathrm{n} \longrightarrow {}^{7}\mathrm{Li} + \alpha + \gamma \tag{2.5}$$

The probability for triggering this reaction is inversely proportional to the speed of the neutrons [72].

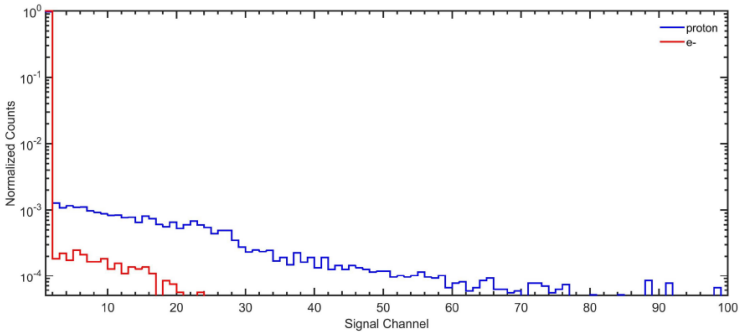

FIGURE 2.23: The performance of the NUD tested with electron and proton beam.

In order to test the performance of the NUD, the beam tests of electron and proton are used. The responses of the NUD to these two types of particle are presented in Fig. 2.23. The signals from the electron events are much smaller than that from the proton events. Most of the electron events have signal amplitude less than 2 ADC channels in the NUD. On the other hand, the proton signals are widely spread between 0 and 100 ADC channels. Results of test based on on-orbit data show that the NUD has a proton rejection power about 12.5 for showers with deposited energy larger than 800 GeV in the BGO calorimeter [59].

2.3 The data acquisition system of DAMPE

The Data AcQuisition System (DAQ) of DAMPE [73] is responsible for receiving commands from the satellite computer, determining trigger logic, collecting science and housekeeping data and transferring them to the ground. The functionality diagram of DAQ is presented in Fig. 2.24. The DAQ has two functional modules: the Payload Data Process Unit (PDPU) and the Payload Management Unit (PMU). The PMU is the control center of DAMPE, it receives commands from the ground through a satellite computer then decodes and distributes them to the PDPU and Front End Electronics (FEE) -X/-Y sides. The PDPU receives signals from the BGO and use them to determine trigger type within 1 μs. The decided trigger logic will be sent to the PMU and the FEE. Once a trigger signal is received by the PMU, it will begin to collect scientific data from -X/-Y sides of the FEE. Meanwhile, scientific data from +X/+Y sides are collected by the PDPU. All data will be temporarily stored in the 16GB flash memory storage device in DAMPE then transferred to the ground by the PMU.

The PDPU uses signals from the eight layers of the BGO to decide trigger logic, which include the UnBiased Trigger (UBT), the Minimum Ionizing Particle Trigger (MIPT), the Low Energy Trigger (LET) and the High Energy Trigger (HET). The four types of trigger follow the OR-ed logic to decide a global trigger. The decision logic is presented

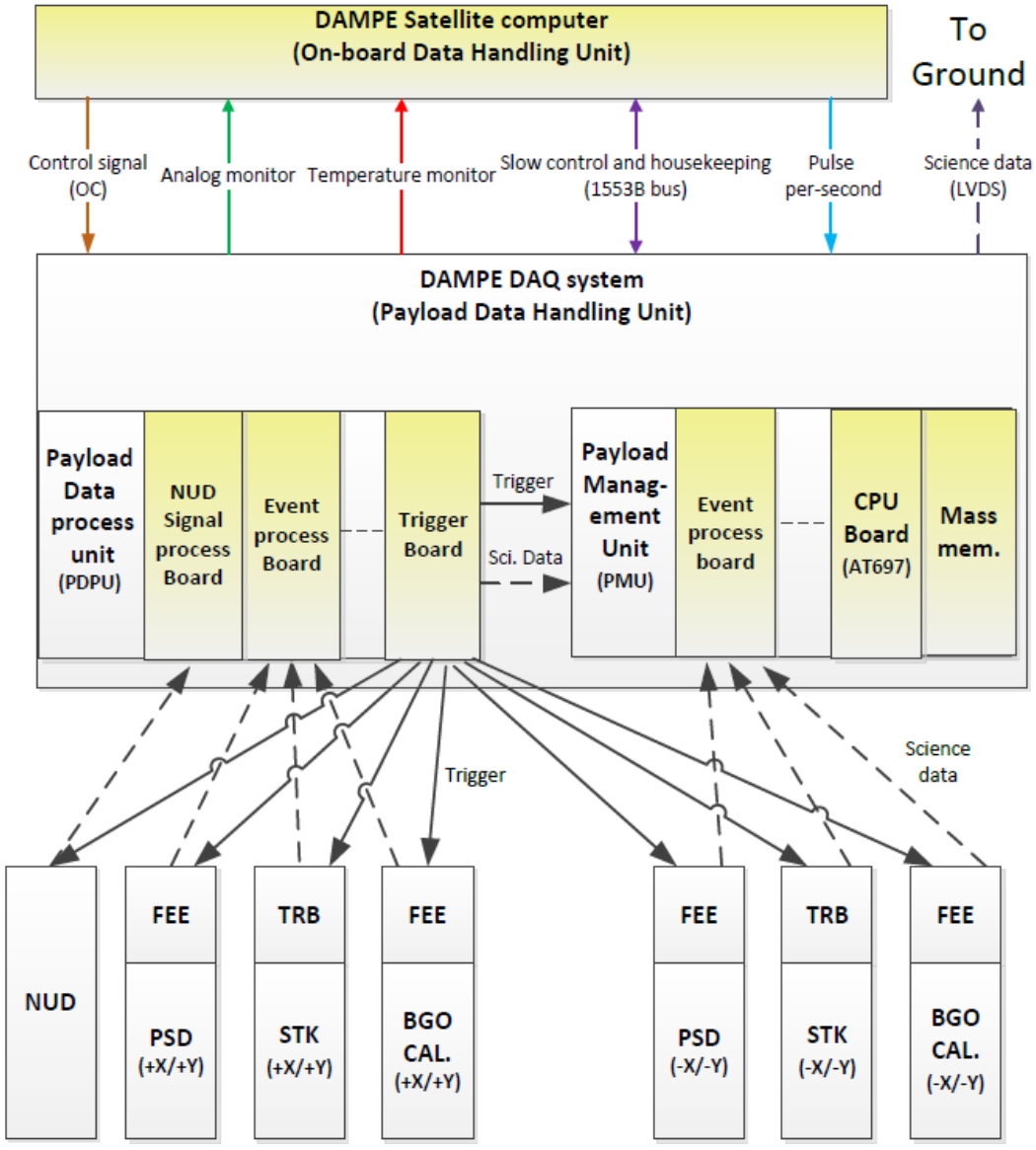

FIGURE 2.24: The diagram and control stream of the DAQ.

in Fig. 2.25. The requirement for each type of the trigger is based on the amplitude of MIP signals on each used BGO layer. The UBT requires that each fired bar in the first two layers has the signals larger than 0.4 MIPs; The MIPT requires each fired bar has the signals larger than 0.4 MIPs in the first two plus penultimate two (or the second two plus last two) layers of the BGO. The MIPT is in purpose of selecting the events that pass through the whole BGO calorimeter. Finally, the LET requires a threshold of 0.4 MIPs in the first two layers and of 2 MIPs in the second two layers of the BGO. The HET has the most stringent requirement which demands that each fired bar has a signal larger than 10 MIPs in the first three layers and larger than 2 MIPs in the fourth layer of the BGO.

The UBT, MIPT and LET are pre-scaled with ratios of 512:1, 4:1 and 8:1 respectively

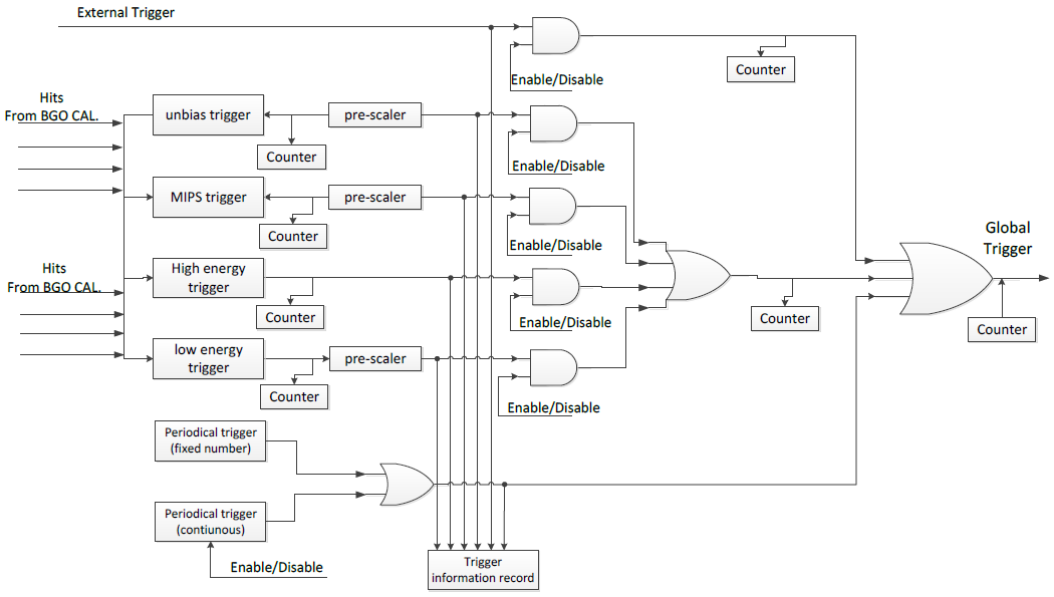

FIGURE 2.25: Diagram of the trigger logic of DAMPE.

when the satellite is within the geographical latitude [-20°, 20°]. For the other parts of the latitude, the UBT and LET are pre-scaled with ratio of 2048:1 and 64:1 respectively, and the MIPT is disabled. The HET is the only type of trigger that dose not have any reduction on the trigger rate during the flight. In total, the average global trigger rate of DAMPE is about 70 Hz.

2.4 The DAMPE Coordinate system

The origin point of the coordinate system of the DAMPE is located between the STK and BGO, and it is straight above the center point of the BGO along the Z direction of the coordinate. The Z axis overlaps with the center axis of the DAMPE system and points to the bottom of the BGO. As it was shown in Fig. 2.26 where we can see the location of each detectors: the PSD is located within [-375 mm, -275 mm] for Z coordinate and [-425 mm, 425 mm] for X/Y coordinate; the STK is located within [-200 mm, 30 mm] for Z coordinate and [-400 mm, 400 mm] for X/Y coordinate; the BGO is placed within [46 mm, 550 mm] for Z coordinate and [-280 mm, 280 mm] for X/Y coordinate; and the NUD is located within the Z coordinate [750mm, 780mm] and X/Y coordinate [-300mm, 300mm].

After the introduction on the DAMPE device, we will analyze the data collected by DAMPE in the following two chapters. In order to measure a CR spectrum, a crucial work is to precisely reconstruct the primary energy of nuclei candidates, thus the energy

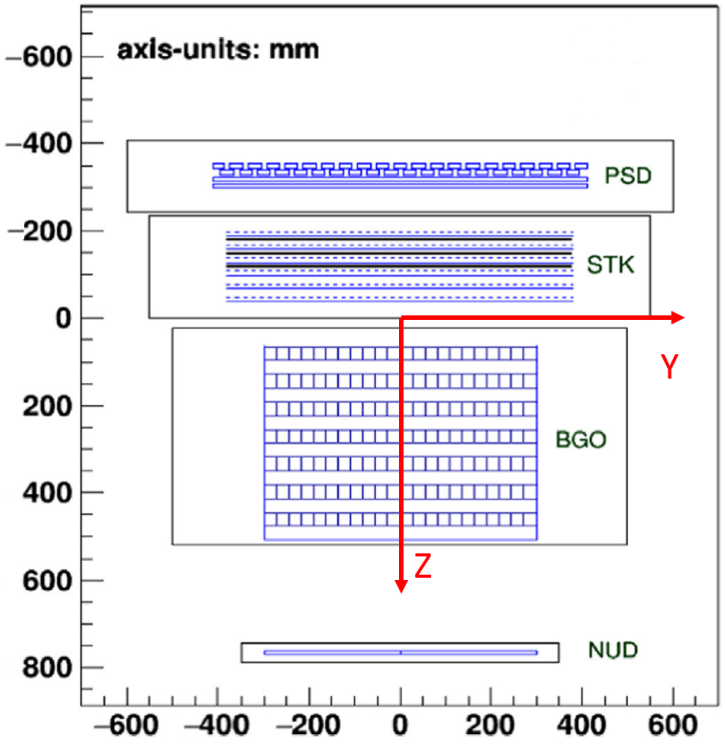

FIGURE 2.26: The coordinate system on YZ view for DAMPE.

reconstruction method will be discussed in chapter three, then the detailed analysis procedures on measuring the proton + helium spectrum will be shown in chapter four.

Chapter 3

The energy reconstruction procedures

The measurement of cosmic ray nuclei is one of the main objectives of DAMPE. The precision of a hadronic measurement is determined by various aspects, the reconstruction of hadron energy plays a critical role among them. In this chapter, the methods used in hadron energy reconstruction are discussed. The features of hadronic showers will be introduced in section 3.1. Then the challenges in reconstructing hadron energy with DAMPE will be discussed in section 3.2, following with the introduction on three widely used methods in section 3.3. The reliability of these methods will be tested by using MC samples to produce a pseudo spectrum in section 3.4. The performances of these methods will be compared (through the produced spectra) to find the most effective one. It turns out that the method based on Bayes theorem has the best performance. Besides, the Bayes method has also been verified with data of the proton beam tests performed by DAMPE at CERN. This will be the content of section 3.5. The results show that the Bayes method can reconstruct the energy of the proton beam with good quality as well.

3.1 Hadronic shower development in the BGO

The BGO calorimeter of DAMPE is in charge of measuring the energy of entering particles and distinguishing electromagnetic from hadronic cascades. A high energy particle will initiate a particle shower in the BGO in which a large number of secondary particles will be produced. These particles will lose their energies in the BGO bars and produce scintillation light that will be collected by the PMTs installed on both ends of BGO bars. Since the scintillation light is proportional to the deposited energy, the output signals

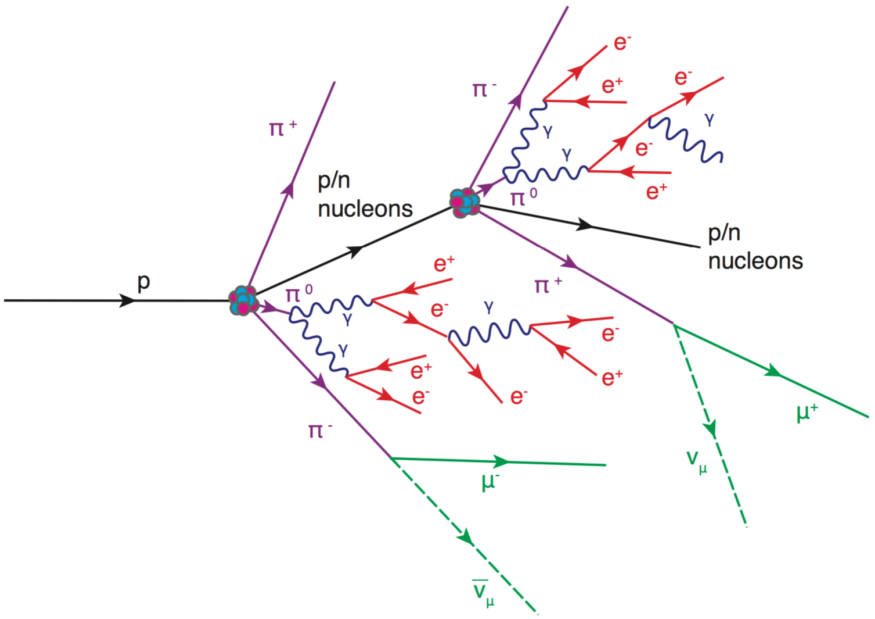

FIGURE 3.1: The diagram of a hadronic shower induced by a proton event.

of PMTs reflect the deposited energy of an event. Summing the measurements from all BGO bars, the total deposited energy of an entering particle can thus be obtained. This is the standard routine for energy measurement in the BGO calorimeter [74].

There are two types of shower that might be induced in the BGO: electromagnetic and hadronic showers. The electromagnetic cascade consists of electron-positron pairs and photons [75], meanwhile the hadronic shower has a more complicated process regarding its product components. When a hadron with high energy enters the calorimeter, the possible interactions with the BGO material include ionization, elastic and inelastic collisions. A shower will be induced once the hadron collides inelastically with nuclei in the BGO. Through nuclear excitation or spallation, a number of secondary particles will be generated, assumed a high enough energy could be obtained, they could interact with the detector material and generate additional secondary particles, a particle cascade is then formed (as shown in Fig. 3.1). The development and the inherent components of the hadronic shower are complicated, hence imposing difficulties on understanding the shower process [76].

The development of a hadronic shower depends on hadron production and pion decay of the shower. Secondary hadrons will behave like their predecessors and continue the shower, if they have high enough energy. As one of the components of secondary hadrons, neutral pions (π^0) have a very short lifetime ($\sim 8.5 \times 10^{-17}$s), and consequently decay immediately into a pair of photons [77]. The photons will initiate an electromagnetic cascade that can be well-measured by the BGO (with $32X_0$). On the other hand, $\pi^{\pm}$

and other hadronic products might interact with detector again and produce another group of secondary particles or escape from the detector (given the fact that the dimension of the BGO is insufficient for fully containing a hadronic shower). The number of secondary particles would reach the maximum at a certain time after the shower is initiated, then the particle number would decrease until being totally absorbed. It is also possible that the secondaries would reach the bottom and escape from the calorimeter. Technically, the hadronic shower contains both electromagnetic (from π^0) and hadronic components. The positions of particles generated in electromagnetic cascades will be generally distributed close to the central axis of the shower. Meanwhile, particles generated in hadronic showers have a wider and deeper distribution. An important parameter used to describe the development of hadron-induced showers is the nuclear interaction length λ_I, which is defined as:

$$\lambda_{\mathrm{I}} = \frac{1}{\mathrm{n}\sigma_{\mathrm{I}}} , \tag{3.1}$$

where n is nucleon number density of target material (the BGO), σ_{I} represents inelastic interaction cross-section. According to parameters extracted from [78], λ_{I} equals to 22.3 cm for BGO material. The calorimeter of DAMPE corresponds to 1.6 nuclear interaction lengths [26]. More details about the development of the hadronic shower can be found in [79, 80].

The characteristic of a hadronic shower impose challenges on measuring the energy of a hadronic particle with DAMPE, which will be presented in the following section.

3.2 Challenges in energy reconstruction of hadrons

To measure the energy of a hadron particle with DAMPE calorimeter is more challenging than measuring then energies of a electron or gamma-ray particles. The radiation length of the BGO is $32X_0$, which enables an electromagnetic shower initiated by an event with energy up to 10 TeV to be fully contained [26]. However, the thickness of the DAMPE calorimeter corresponds to 1.6 λ_I, which indicates that a hadronic shower can only be partly retained. Moreover, large uncertainties regarding hadronic processes impose additional difficulties in energy reconstruction. In general, the main difficulties concerning hadronic energy measurements with DAMPE include:

- About 20% of the entering particles will only lose their energy through ionization [81]. These through-going particles have similar behavior with MIP particles (as introduced in chapter two). Due to the independence of deposited energy of a MIP event from its primary energies, the latter can not be reconstructed by referring to the deposited energy.

- A hadronic shower is activated when an inelastic interaction occurs between the impinging hadron and molecules of the BGO material. However, when the first inelastic interaction will happen is stochastic. If the interaction happens in a deeper position, the energy leakage will be larger.

- Due to tungsten boards being installed in the STK, an incident particle might induce a shower even before reaching the calorimeter. These "early" shower imposes challenges on track reconstruction and increases back-splash particle numbers to the PSD.

- The energy of π^0 can be well-measured in the calorimeter, however, its fraction in a shower has a larger fluctuation. On average, π^0 accounts for 1/3 of all secondaries [82, 83]. The large fluctuation of π^0 fraction implies a larger variation on the deposited energies for hadrons even with the same primary energies.

- The MC simulation plays an important role in reconstructing a hadron energy. Currently, experimental data referring to the behavior of hadrons with energy larger than 1 TeV are scarce. Various theoretical models show discrepancies with each other. These factors contribute to the uncertainties in hadron energy measurement.

Because of these challenges, the energy reconstruction result of hadrons has larger uncertainties than that of leptons and photons. In order to decrease the uncertainties and reconstruct hadron energy with accuracy, a set of selection cuts are used to pick up the candidates with less uncertainties concerning their showers (A specific introduction on the used cuts will be presented in chapter four). To see the influence of the selection cuts, the distributions of the deposited energy (referred to as BGO energy with symbol E_{BGO}) of 400 GeV proton beam data with and without the selections are presented in Fig. 3.2. The selection cuts will eliminate the through-going events (The MIP events due to a similar behaviour of them.) and events with their showers being not well contained by the calorimeter. The quality of the energy reconstruction will be improved based on the selected events.

3.3 Methods for reconstructing the hadron energy

The deposited energy ratio for hadronic nuclei in the BGO is only 35%-40% and with a large fluctuation [26], it is impossible to correct the energy of event through dividing by a certain number which refers to the ratio of the energy deposition. Instead, an effective method is needed to reconstruct the primary energy with accuracy. In this section,

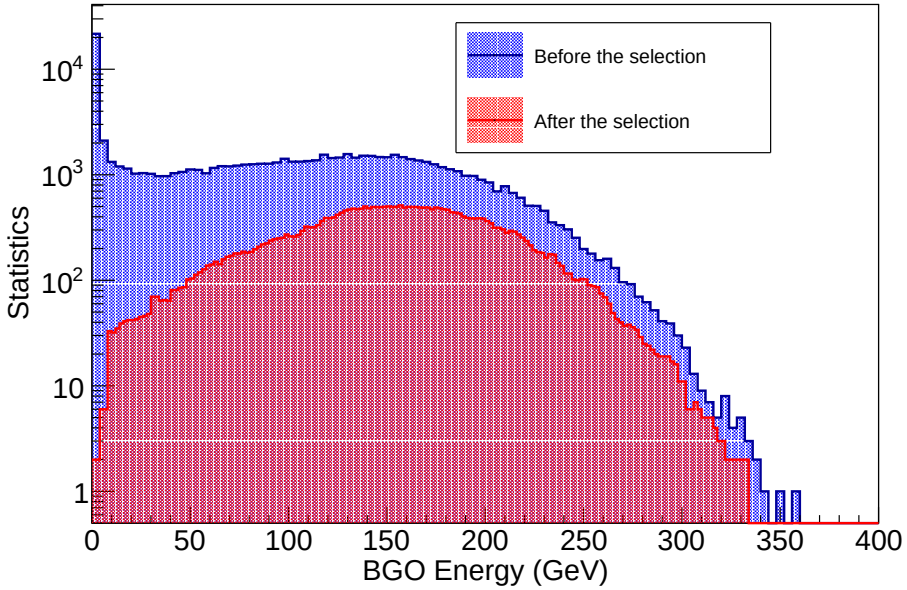

FIGURE 3.2: The distributions of the BGO energy of the 400 GeV proton beam data. The blue part represents the distribution without the event selection, the red part is the same set of data but after the events selection.

the relation between the energy reconstruction and the spectrum will be introduced. Then three methods used for the reconstruction will be described. The performance of a method on reconstructing a spectrum could be referred to as the test for its effectiveness.

The obtained spectrum from the BGO is actually the primary spectrum convoluted with the response of the detector. It can be expressed as:

$$\Phi(E_{BGO}) = \int R(E_{BGO}, E_T) \cdot \Phi(E_T) dE_T \ , \tag{3.2}$$

where E_T is the primary energy (or true energy) of particles and $\Phi(E_T)$ represents the primary spectrum, $\Phi(E_{BGO})$ is the primary spectrum after the response of detector (referred to as observed spectrum), $R(E_{BGO}, E_T)$ is response function which is determined by properties of the detector. In order to get the primary spectrum we need to reconstruct the primary energy E_T by using of the observed energy (the deposited energy in the BGO , referred to as E_{BGO}). This is an unfolding issue in mathematics, the effect of the detector need to be unfolded in this case. The distribution of CR spectra follows a power-law, therefore, we use logarithmic bins in this chapter (Also in chapter 4). Assuming that the energy axis of the observed spectrum is split into m bins and primary spectrum into n bins. The new form of Eq. 3.2 with energy being discrete can be written as:

$$N(E^j_{BGO}) = \sum_{i=1}^{n} P(E^j_{BGO}|E^i_T) \cdot N(E^i_T), \quad j = 1, 2, ..., m, \tag{3.3}$$

$N(E^j_{BGO})$ is the number of the events in j-th energy bin of the observed spectrum, $N(E^i_T)$ is the number of the event in i-th energy bin of the primary spectrum. Furthermore, $P(E^j_{BGO}|E^i_T)$ represents the probability matrix which reflects the response effect of the detector. Since $P(E^j_{BGO}|E^i_T)$ can only be obtained from MC simulation, $P(E^j_{BGO_{MC}}|E^j_{T_{MC}})$ (with $E_{BGO_{MC}}$ and $E_{T_{MC}}$ being distinguished from the real data counterparts) is used to represent the probability matrix.

There are various unfolding algorithms [84, 85], the three widely used methods: The one based on Bayes theorem [86], Singular Value Decomposition method [87] and Iterative Dinamically Stabilized method [88, 89] will be tested by producing a spectrum based on pure MC simulation. In this section, the principles and procedures to produce a spectrum will be introduced, the performances of the three methods will be checked with MC samples.

3.3.1 Method based on the Bayes theorem

The unfolding method based on the Bayes theorem has been widely used by other CR and particle physics experiments [90–93]. The Bayes theorem can be written as:

$$P(A|B) = \frac{P(B|A) \cdot P(A)}{P(B)} , \tag{3.4}$$

where P(B|A) is a conditional probability that represents the likelihood of event B happening given the event A is true. P(A|B) is the converse version of P(B|A). P(A) or P(B) is the probability of event A or B happening independently, which are named as margin probability.

In our case, the primary spectrum and observed spectrum can be used to compute the margin probabilities. Meanwhile, the MC simulation must be used to determine the detector response thus to derive the conditional probability. The equation. 3.4 can be rewritten as:

$$P(E^i_{T_{MC}}|E^j_{BGO_{MC}}) = \frac{P(E^j_{BGO_{MC}}|E^i_{T_{MC}}) \cdot P_0(E^i_T)}{\sum_{i=1}^{n} P(E^j_{BGO_{MC}}|E^i_{T_{MC}}) \cdot P_0(E^i_T)} . \tag{3.5}$$

The $P_0(E^i_T)$ represents prior probability. In general, the $P_0(E^i_T)$ is determined according to experience (for example from precedent experiments or theoretical models). $P(E^i_{T_{MC}}|E^j_{BGO_{MC}})$ is the conditional probability that is needed to unfold the detector response. It reflects the probability of one event has the primary energy inside i-th bin of $E_{T_{MC}}$ given that this event is observed in j-th bin of $E_{BGO_{MC}}$. Meanwhile $P(E^j_{BGO_{MC}}|E^i_{T_{MC}})$ is the inverse version of $P(E^i_{T_{MC}}|E^j_{BGO_{MC}})$ and can be computed

through the MC simulation by the equation of:

$$P(E^{j}_{BGO_{MC}}|E^{i}_{T_{MC}}) = \frac{N(E^{j}_{BGO_{MC}}|E^{i}_{T_{MC}}, sel)}{N(E^{i}_{T_{MC}})} , \tag{3.6}$$

where $N(E^{i}_{T_{MC}})$ is the number of MC generated events in i-th bin of true energy, $N(E^{j}_{BGO_{MC}}|E^{i}_{T_{MC}}, sel)$ is the number of events that are observed in j-th bin of $E_{BGO_{MC}}$ given their true energy belongs to the i-th bin of $E_{T_{MC}}$ after performing the selection cuts. Once $P(E^{j}_{BGO_{MC}}|E^{i}_{T_{MC}})$ and $P_0(E^{i}_{T})$ are determined, the $P(E^{i}_{T}|E^{j}_{BGO_{MC}})$ can be derived. Then the primary spectrum can be calculated as:

$$\hat{N}(E^{i}_{T}) = \frac{1}{\epsilon_i} \sum_{j=1}^{n} P(E^{i}_{T_{MC}}|E^{j}_{BGO_{MC}}) \cdot N(E^{j}_{BGO}) , \tag{3.7}$$

where ϵ_i is the measurement efficiency and equals to $\sum_{j=1}^{n} P(E^{j}_{BGO}|E^{i}_{T})$, $\hat{N}(E^{i}_{T})$ is the number of events in i-th bin of E_T, it represents the primary spectrum as well. $\hat{N}(E^{i}_{T})$ will be computed iteratively. After one iteration, we will use the new $\hat{N}(E^{i}_{T})$ to update the prior probability of $P_0(E^{i}_{T})$ by using the equation of:

$$\hat{P}(E^{i}_{T}) = \frac{\hat{N}(E^{i}_{T})}{\sum_{i=1}^{n} \hat{N}(E^{i}_{T})} , \tag{3.8}$$

$P_0(E^{i}_{T})$ will be replaced by $\hat{P}(E^{i}_{T})$ in equation 3.5. Then another iteration starts by going through equation. 3.5, and 3.7 until the $\hat{N}(E^{i}_{T})$ is stable, which means the number of event in each bin of E_T change less than a threshold after an iteration.

The calculation of the statistical error

The statistical error propagated to $\hat{N}(E^{i}_{T})$ by the unfolding procedure need to be calculated carefully. In order to figure out the errors propagated by the Bayes unfolding method, the equation. 3.5, 3.7, 3.8 are combined and get:

$$\hat{N}(E^{i}_{T}) = \sum_{j}^{n} M_{ij} \cdot N(E^{j}_{BGO}) , \tag{3.9}$$

where

$$M_{ij} = \frac{P(E^{j}_{BGO_{MC}}|E^{i}_{T}) \cdot N(E^{i}_{T_{MC}})}{\epsilon_i \cdot \sum_{l=1}^{n} P(E^{j}_{BGO_{MC}}|E^{l}_{T_{MC}}) \cdot N(E^{l}_{T})} . \tag{3.10}$$

The error comes from two parts according to equation 3.9: $N(E^{j}_{BGO})$ and M_{ij}. The method of computing the covariance matrix introduced by [94] is used to calculate the error. The total covariance V_{kl} equals $V_{kl}(N(E_{BGO})) + V_{kl}(M)$. For the part of

$V_{kl}(N(E_{BGO}))$, according to 3.9 there is:

$$\frac{\partial \hat{N}(E_T^i)}{\partial N(E_{BGO}^j)} = M_{ij} + \frac{\hat{N}(E_T^i)}{N(E_T^i)} \cdot \frac{\partial N(E_T^i)}{\partial N(E_{BGO}^j)} - \sum_{k=1}^{n}\sum_{l=1}^{n} \frac{N(E_{BGO}^k)\epsilon_l}{N(E_T^l)} \cdot M_{ik} \cdot M_{lk} \cdot \frac{\partial N(E_T^l)}{\partial N(E_{BGO}^j)} \ . \tag{3.11}$$

For the first iteration, the $N(E_T^i)$ is independent with $N(E_{BGO}^j)$. Hence $\partial N(E_T^i)/\partial N(E_{BGO}^j)$ equals 0, and $\partial \hat{N}(E_T^i)/\partial N(E_{BGO}^j)$ equals M_{ij}. By using the error propagation matrix, the covariance matrix of the spectrum after unfolding can be derived as:

$$V(\hat{N}(E_T^k), \hat{N}(E_T^l)) = \sum_{i=1}^{n}\sum_{j=1}^{n} \frac{\partial \hat{N}(E_T^k)}{\partial N(E_{BGO}^i)} \cdot V(N(E_{BGO}^i), N(E_{BGO}^j)) \cdot \frac{\partial \hat{N}(E_T^l)}{\partial N(E_{BGO}^j)} \ . \tag{3.12}$$

In equation. 3.12, $N(E_{BGO})$ follows a Poisson distribution independently in each bin. Therefore:

$$V(N(E_{BGO}^i), N(E_{BGO}^j)) = N(E_{BGO}^i) \cdot \delta_{ij} \tag{3.13}$$

with:

$$\delta_{ij} = \begin{cases} 1 & i = j \\ 0 & i \neq j \end{cases} \tag{3.14}$$

combing the Eq. 3.12, 3.13 we get:

$$V(\hat{N}(E_T^k), \hat{N}(E_T^l)) = \sum_{i=1}^{n} \frac{\partial \hat{N}(E_T^k)}{\partial N(E_{BGO}^i)} \cdot N(E_{BGO}^i) \cdot \frac{\partial \hat{N}(E_T^l)}{\partial N(E_{BGO}^i)} \ . \tag{3.15}$$

The second part of the error comes from the response matrix (or M_{ij}). Since the statistics of MC is not infinitely large, and the response matrix is filled by MC samples, thus a statistics uncertainty exists for each bin of the matrix. With the unfolding procedures, the statistics uncertainty will be propagated to the spectrum. Considering the dependency of the $N(E_T^i)$ on the response matrix, the error due to the response matrix is:

$$\begin{aligned} \frac{\partial \hat{N}(E_T^i)}{\partial P(E_{BGO_{MC}}^j | E_{T_{MC}}^k)} = \frac{1}{\epsilon_i} \cdot \Big(& \frac{N(E_T^i) \cdot N(E_{BGO}^j)}{\sum_{l=1}^{n} P(E_{BGO_{MC}}^j | E_{T_{MC}}^l) \cdot N(E_T^l)} - \hat{N}(E_T^i) \Big) \cdot \delta_{ik} - \\ & \frac{N(E_T^k) \cdot N(E_{BGO}^j)}{\sum_{l=1}^{n} P(E_{BGO_{MC}}^j | E_{T_{MC}}^l) \cdot N(E_T^l)} \cdot M_{ij} + \frac{\hat{N}(E_T^i)}{N(E_T^i)} \cdot \frac{\partial N(E_T^i)}{\partial P(E_{BGO}^j | E_T^k)} - \\ & \frac{\epsilon_i}{N(E_T^i)} \cdot \sum_{l=1}^{n}\sum_{r=1}^{n} N(E_{BGO}^l) \cdot M_{il} \cdot M_{rl} \cdot \frac{\partial N(E_T^r)}{\partial P(E_{BGO}^j | E_T^k)} \ , \end{aligned} \tag{3.16}$$

where the $\partial N(E_T^i)/\partial P(E_{BGO_{MC}}^j | E_{T_{MC}}^k)$ represents the error propagation matrix from the previous iteration. Considering the complexity of the calculation, the statistical error is derived through a TOY-MC method (see chapter four) in practice. An analogous calculation for the error can be found in the other two methods, we will not describe

them in the following contents.

In general, the procedures to proceed the Bayes unfolding method include the follows:

1. Compute the probability matrix $P(E^{j}_{BGO_{MC}}|E^{i}_{T_{MC}})$ with equation 3.6;
2. Set the prior probability $P_0(E^{i}_{T})$ and compute the unfolding probability matrix with matrix equation 3.5;
3. Use the equation 3.7 to unfold the data;
4. After the unfolding, check the result, if it is good enough (agree well with the expectation or the unfolding has only minor effect on the energy distribution of events), stop the iteration. If not, go to step 5;
5. Update the prior probability with equation 3.8 and use it in equation 3.5 to get an new unfolding probability matrix;
6. Repeat the step 3, 4, 5 until the result is good enough or stop when the maximum iteration constraint is reached.

3.3.2 Singular Value Decomposition method

The Singular Value Decomposition (SVD) method is to perform singular value decomposition no the response matrix, thus to obtain its inverse matrix and use it to unfold the detector response. The related derivations and procedures to perform the SVD method is briefly introduced in this section. More details can be found in [87].

According to equation 3.3, the detector response can be expressed as $P(E^{j}_{BGO_{MC}}|E^{i}_{T_{MC}})$ which represents the probability of one event that is generated in i-th bin of the true energy and detected in j-th bin of the observed energy, we will simply refer to it as P_{ji}. The equation 3.3 in form of matrix can be written as:

$$\boldsymbol{N_O} = \hat{P}\boldsymbol{N_T} \ , \tag{3.17}$$

where $\boldsymbol{N_O}$ and $\boldsymbol{N_T}$ are the vectors that represent the counts of event in each observed energy bin ($N(E^{j}_{BGO})$) and true energy bin ($N(E^{j}_{T})$). $\hat{P}$ is the matrix with element of P_{ji}, which is obtained from the MC simulation.

In practice, instead of using equation 3.17 directly, a normalization will be performed as $w_i = N(E^{i}_{T})/N(E^{i}_{T_{MC}})$. The $N^{i}_{T_{MC}}$ is the number of MC generated events in i-th bin of true energy. With the vector of $\boldsymbol{w}$ for w_i, the equation 3.17 can be re-written as:

$$\boldsymbol{N_O} = \hat{P}\boldsymbol{w} \ , \tag{3.18}$$

with the $\boldsymbol{N_T}$ being replaced by $\boldsymbol{w}$, the $\hat{\mathrm{P}}$ also need to multiply $\mathrm{N}(\mathrm{E}^{\mathrm{i}}_{\mathrm{T_{MC}}})$ correspondingly to guarantee the correctness of 3.18. After multiplying the factors, the $\hat{\mathrm{P}}$ is no longer the probability matrix, but a matrix with elements of the number of event in corresponding energy bins. Equation 3.18 instead of equation 3.17 is used so that a large error introduced by the unfolding procedures can be avoided [87].

The weighted least square issue should be considered to reach the optimal solution of the unfolding process, which can be done by minimizing the quantity

$$\sum_{\mathrm{j=1}}^{\mathrm{n}}\left(\frac{\sum_{\mathrm{i=1}}^{\mathrm{m}}(\mathrm{P_{ji}N}(\mathrm{E}^{\mathrm{i}}_{\mathrm{T}}))-\mathrm{N}(\mathrm{E}^{\mathrm{j}}_{\mathrm{BGO}})}{\Delta\mathrm{N}(\mathrm{E}^{\mathrm{j}}_{\mathrm{BGO}})}\right)^2 . \tag{3.19}$$

Supposing that the the observe energy has m bins and true energy has n bins, which have an equal width in exponential space. $\Delta\mathrm{N}(\mathrm{E}^{\mathrm{j}}_{\mathrm{BGO}})$ is the error in $\mathrm{N}(\mathrm{E}^{\mathrm{j}}_{\mathrm{BGO}})$. Then, the equation 3.19 can been written as:

$$(\hat{\mathrm{P}}\boldsymbol{N_O})^{\boldsymbol{T}}\boldsymbol{N}^{-\mathbf{1}}_{\boldsymbol{O_E}}(\hat{\mathrm{P}}\boldsymbol{N_O}) = \min . \tag{3.20}$$

$\boldsymbol{N_{O_E}}$ is the covariance matrix of the measured spectrum $\boldsymbol{N_O}$. Due to the propriety of the covariance matrix, $\boldsymbol{N_{O_E}}$ should be symmetric and positive-definite. The SVD is performed on matrix $\boldsymbol{N_{O_E}}$ and yields:

$$\boldsymbol{N_{O_E}} = \boldsymbol{QRQ^T},\ \mathrm{R_{jj}} \equiv \mathrm{r_j^2} \neq 0,\ \mathrm{R_{ji}} = 0 \text{ for } \mathrm{j} \neq \mathrm{i},\ \boldsymbol{N^{-1}_{O_E}} = \boldsymbol{QR^{-1}Q^T} . \tag{3.21}$$

Substituting $\boldsymbol{N^{-1}_{O_E}}$ with $\boldsymbol{QR^{-1}Q^T}$ in equation 3.20:

$$\tilde{\mathrm{P}}_{\mathrm{ji}} = \frac{1}{\mathrm{r_j}}\cdot\sum_{\mathrm{x=1}}^{\mathrm{m}}(\mathrm{Q_{jx}}\cdot\mathrm{P_{xi}}),\quad \tilde{\mathrm{N}}(\mathrm{E}^{\mathrm{j}}_{\mathrm{BGO}}) = \frac{1}{\mathrm{r_j}}\sum_{\mathrm{x=1}}^{\mathrm{m}}(\mathrm{Q_{jx}}\cdot\mathrm{N}(\mathrm{E}^{\mathrm{x}}_{\mathrm{BGO}})) . \tag{3.22}$$

With $\mathrm{P_{ij}}$ replaced by $\tilde{\mathrm{P}}_{\mathrm{ij}}$ ($\hat{\mathrm{P}}$ replaced by $\tilde{\mathrm{P}}$ correspondingly), and $\mathrm{N}(\mathrm{E}^{\mathrm{j}}_{\mathrm{BGO}})$ replaced by $\hat{\mathrm{N}}(\mathrm{E}^{\mathrm{j}}_{\mathrm{BGO}})$ ($\boldsymbol{N_O}$ replaced by $\tilde{\boldsymbol{N}}_{\boldsymbol{O}}$), the expression of the equation 3.20 becomes simple:

$$(\tilde{\mathrm{P}}\cdot\boldsymbol{w}-\tilde{\boldsymbol{N}}_{\boldsymbol{O}})^{\mathrm{T}}(\tilde{\mathrm{P}}\boldsymbol{w}-\tilde{\boldsymbol{N}}_{\boldsymbol{O}}) = \min . \tag{3.23}$$

The minimization of equation 3.23 leads to:

$$\sum_{\mathrm{i}}^{\mathrm{n}}\tilde{\mathrm{P}}_{\mathrm{ji}}\mathrm{w_i} = \tilde{\mathrm{N}}(\mathrm{E}^{\mathrm{j}}_{\mathrm{BGO}}) . \tag{3.24}$$

The solution of equation 3.24 is usually with large fluctuation, thus meaningless in practice [95]. In [96, 97], a regularization part to the item that need to be minimized is proposed to solve this problem. According to this proposal, the equation 3.23 can be

modified into:

$$(\tilde{\mathrm{P}}\boldsymbol{w} - \tilde{\boldsymbol{N}}_{\boldsymbol{O}})^{\mathrm{T}}(\tilde{\mathrm{P}}\boldsymbol{w} - \tilde{\boldsymbol{N}}_{\boldsymbol{O}}) + \tau(\boldsymbol{C}\boldsymbol{w})^{\mathrm{T}}(\boldsymbol{C}\boldsymbol{w}) = \min \ . \tag{3.25}$$

τ is the weight of the regularization item. $\boldsymbol{C}$ is a matrix which represents a prior condition. According to [87], the $\boldsymbol{C}$ should be chosen to suppress the bin-to-bin variation. Equation 3.25 leads to a liner equation:

$$\begin{bmatrix} \tilde{\mathrm{P}} \\ \sqrt{\tau}\boldsymbol{C} \end{bmatrix} \boldsymbol{w} = \begin{bmatrix} \tilde{\boldsymbol{N}}_{\boldsymbol{O}} \\ 0 \end{bmatrix} \ . \tag{3.26}$$

Since the τ is with the $\boldsymbol{C}$, we need to perform the SVD on $\sqrt{\tau}\boldsymbol{C}$ every time when trying to test a new value of τ. This is somehow inconvenient. This can be solved by transforming equation 3.26 into:

$$\begin{bmatrix} \tilde{\mathrm{P}}\boldsymbol{C}^{-1} \\ \sqrt{\tau}I \end{bmatrix} \boldsymbol{C}\boldsymbol{w} = \begin{bmatrix} \tilde{\boldsymbol{N}}_{\boldsymbol{O}} \\ 0 \end{bmatrix} \ , \tag{3.27}$$

where τ is with the unit matrix I and allows to express the solution for equation 3.26 for any values [97]. Moreover, for the determination of $\boldsymbol{C}$, [87] suggests to use the form of:

$$\boldsymbol{C} = \begin{bmatrix} -1+\xi & 1 & 0 & 0 & \dots \\ 1 & -2+\xi & 1 & 0 & \dots \\ 0 & 1 & -2+\xi & 1 & \dots \\ & \dots & & & \dots \\ & \dots & 1 & -2+\xi & 1 \\ & \dots & & 1 & -1+\xi \end{bmatrix} \ . \tag{3.28}$$

The reason for using a ξ is to guarantee the $\boldsymbol{C}$ can be inversed and do not affect the stability of the $\boldsymbol{w}$. In general, a small number should be choosen as the value of ξ. In this work, ξ equals 10^{-4}.

With all these preparations, the equation 3.27 can be solved. Then the value of $\boldsymbol{w}$ can be derived and used into the unfolding procedure. In order to simplify the calculation, the unfolding starts with $\tau = 0$ and perform singular value decomposition on the product of $\tilde{\mathrm{P}}\boldsymbol{C}^{-1}$:

$$\tilde{\mathrm{P}}\boldsymbol{C}^{-1} = \boldsymbol{U}\boldsymbol{S}\boldsymbol{V}^{\boldsymbol{T}} \ , \tag{3.29}$$

with $\boldsymbol{U}$ and $\boldsymbol{V}$ are orthogonal matrix and $\boldsymbol{S}$ is diagonal matrix with the singular values decreasingly ranked, if we define:

$$\boldsymbol{d} \equiv \boldsymbol{U}^{\boldsymbol{T}}\tilde{\boldsymbol{N}}_{\boldsymbol{O}} \ , \ \boldsymbol{z} \equiv \boldsymbol{V}^{\boldsymbol{T}}\boldsymbol{C}\boldsymbol{w} \ , \tag{3.30}$$

and combining with equation 3.27, there are:

$$\boldsymbol{d} = \boldsymbol{S}\boldsymbol{z} \text{ , thus } d_i = s_{ii} \cdot z_i \text{ ,} \tag{3.31}$$

s_{ii} is referred to as s_i since the matrix $\boldsymbol{S}$ is diagonal.The solution of equation 3.27 can be obtained with $\tau = 0$ (non-regularized) as:

$$z_i^{(\tau=0)} = \frac{d_i}{s_i} \text{ , } \boldsymbol{w}^{(\tau=0)} = \boldsymbol{C^{-1}V}\boldsymbol{z}^{(\tau=0)} \text{ .} \tag{3.32}$$

The distribution of $N(E_T^i)$ can be obtained by using w_i of $\boldsymbol{w}$ multiplying the corresponding $N(E_{T_{MC}}^i)$. However, this solution is obtained with condition of $\tau = 0$, in this case, $\boldsymbol{w}$ is with large uncertainty. According to [97], importing a non-zero τ in the calculation is equivalent to change d_i as:

$$d_i^{(\tau)} = d_i \cdot \frac{s_i^2}{s_i^2 + \tau} \text{ ,} \tag{3.33}$$

the solution becomes:

$$z_i^{(\tau)} = \frac{d_i s_i}{\cdot} s_i^2 + \tau \text{ , } \boldsymbol{w}^{(\tau)} = \boldsymbol{C^{-1}V}\boldsymbol{z}^{(\tau)} \text{ .} \tag{3.34}$$

The value of $\boldsymbol{w}$ can be obtained once the τ is determined. A precise discussion on how to decide the τ has been made in [87], we will follow its procedures and describe the principle briefly here: In general, only the first few items, say k, of the $\boldsymbol{S}$ matter significantly. Thus a critical value of i should be taken as i=k, after which d_i is so small that it can barely affect the final results. The value of the k can be clear seen on the distribution of $\log(d_i)$ as a function of i. The d_i decays exponentially with increasing i, and at certain point, becomes a constant. The k is taken equaling the value of i at that point. Then the regularization parameter τ should be the square of the k-th singular value of matrix $\tilde{P}\boldsymbol{C}^{-1}$, which is:

$$\tau = s_k^2 \text{ .} \tag{3.35}$$

With equation 3.35, 3.34, the value of $\boldsymbol{w}$ can be derived. Then the unfolded spectrum can be written as:

$$N(E_T^i) = w_i \cdot N(E_{T_{MC}}^i) \text{ .} \tag{3.36}$$

In general, in order to perform SVD method to unfold the detector response, the following procedures should be applied:

1. Generate MC 2-dimensional histogram $\tilde{P}$ by using of the true energy ($E_{T_{MC}}$) and observed energy ($E_{BGO_{MC}}$) as its axes. The elements of $\tilde{P}$ contain the numbers of generated events rather than the probabilities.

2. Build the matrix $\boldsymbol{C}$ according to equation 3.28, and calculate its inverse matrix $\boldsymbol{C}^{-1}$.

3. Fill the histogram of $\boldsymbol{N_O}$ and calculate its covariance matrix $\boldsymbol{N_{O_E}}$.

4. Perform singular value decomposition on covariance matrix $\boldsymbol{N_{O_E}}$ according to equation 3.21 and get its inverse matrices

5. Use the decomposed matrices of $\boldsymbol{N_{O_E}^{-1}}$ to obtain the $\tilde{\mathrm{P}}$ according to equation 3.22

6. Multiply the $\tilde{\mathrm{P}}$ and $\boldsymbol{C}^{-1}$ and perform the SVD on the product according to equation 3.29

7. Calculate the $\boldsymbol{d}$ according to equation 3.30.

8. Determine the value of τ through the distribution of $\mathrm{d_i}$ as a function of i.

9. Calculate the $\boldsymbol{w}^{(\tau)}$ according to equation 3.33, 3.34

10. Calculate the $\mathrm{N(E_T^i)}$ according to equation 3.36, and $\mathrm{N(E_T^i)}$ is the unfolded result.

3.3.3 Iterative Dinamically Stabilized method

In this section, the IDS method will be introduced. The IDS method can deal with the new structures, like a spectrum bump that exist in the data but absent in the MC simulation. We will briefly introduce the necessary procedures to implement the method. More details about the toning of the parameters and the validation of the method can be found in [89].

The IDS method is based on a premise that the MC simulation provides a good description on real data and detector response, therefore, one can trust the response matrix obtained from MC and use it to reconstruct the energy of events. If this is not the case, [89] provides a normalization method on the MC to improve the agreement between the data and the MC during the iteration process.

A regularization function that is used during the iteration process will be introduced first. The function can dynamically reduce the data fluctuations due to the event selection procedures. The selections lead to a deduction on the statistics, thus the fluctuation of the data due to statistics uncertainty will increase. Since we will perform a set of selections on the data before performing the unfolding procedures, the regularization function is meaningful in improving the quality of the energy reconstruction. The regularization function $\mathrm{f}(\Delta \mathrm{x}, \sigma, \lambda)$ can be utilized to provide a weight on event number deviation Δx between each bins of the data and the MC. σ is the corresponding error of

Δx, λ is a scaling factor. The f(Δx, σ, λ) must be a smooth monotonous function with f(Δx, σ, λ) =0 when Δx =0, and f(Δx, σ, λ) =1 when Δx $\gg$ σ. Several forms of the f(Δx, σ, λ) are available. It has been proved in [89] that the choose of the function has little impact on the final unfolding results. In this chapter, we choose the f(Δx, σ, λ) as:

$$\mathrm{f}(\Delta\mathrm{x}, \sigma, \lambda) = 1 - \mathrm{e}^{-(\frac{\Delta\mathrm{x}}{\lambda\sigma})^2} \ . \tag{3.37}$$

With the regularization function, the normalization can be performed on the MC to make it approaching to the data. A variable $\mathrm{NE_{data}}$ is defined as:

$$\mathrm{NE_{data}} = \sum_{\mathrm{i}=1}^{\mathrm{m}} (\mathrm{N}(\mathrm{E^i_{BGO}}) - \mathrm{eN}(\mathrm{E^i_{BGO}})) \ , \tag{3.38}$$

with $\mathrm{N}(\mathrm{E^i_{BGO}})$ is the number of event in i-th bin of the data after the selections. $\mathrm{eN}(\mathrm{E^i_{BGO}})$ is the number of event in i-th bin due to the fluctuation of the events that is eliminated by the selection cuts. Analogously, $\mathrm{NE_{mc}}$ is defined for the MC. The normalization factor for the MC is taken as $\mathrm{NE_{data}}$ divided by $\mathrm{NE_{mc}}$. $\mathrm{NE_{data}}$ will be updated during the iteration as:

$$\mathrm{NE^{'}_{data}} = \mathrm{NE_{data}} + \sum_{\mathrm{k}=1}^{\mathrm{m}} (1 - \mathrm{f}(|\Delta\mathrm{N}(\mathrm{E^k_{BGO}})|, \hat{\sigma}(\mathrm{N}(\mathrm{E^k_{BGO}})), \lambda)) \cdot \Delta\mathrm{N}(\mathrm{E^k_{BGO}}) \ , \tag{3.39}$$

where $\Delta\mathrm{N}(\mathrm{E^k_{BGO}})$ equals:

$$\Delta\mathrm{N}(\mathrm{E^k_{BGO}}) = \mathrm{N}(\mathrm{E^k_{BGO}}) - \mathrm{eN}(\mathrm{E^k_{BGO}}) - \frac{\mathrm{NE_{data}}}{\mathrm{NE_{mc}}} \cdot \mathrm{N}(\mathrm{E^k_{BGO_{MC}}}) \ , \tag{3.40}$$

and $\hat{\sigma}(\mathrm{N}(\mathrm{E^k_{BGO}}))$ can be written as:

$$\hat{\sigma}(\mathrm{N}(\mathrm{E^k_{BGO}})) = \sqrt{\sigma^2(\mathrm{N}(\mathrm{E^k_{BGO}})) + (\frac{\mathrm{NE_{data}}}{\mathrm{NE_{mc}}})^2 \cdot \sigma^2(\mathrm{N}(\mathrm{E^k_{BGO_{MC}}}))} \tag{3.41}$$

In equation 3.41, $\sigma(\mathrm{N}(\mathrm{E^k_{BGO}}))$ and $\sigma(\mathrm{N}(\mathrm{E^k_{BGO_{MC}}}))$ represent the error in k-th bin of data and MC respectively. Besides, $\mathrm{eN}(\mathrm{E^i_{BGO}})$ can be computed as:

$$\mathrm{eN}(\mathrm{E^i_{BGO}}) = (1 - \mathrm{f}(|\Delta^{'}\mathrm{N}(\mathrm{E^i_{BGO}})|, \hat{\sigma}(\mathrm{N}(\mathrm{E^i_{BGO}})), \lambda))\Delta^{'}\mathrm{N}(\mathrm{E^i_{BGO}}) \tag{3.42}$$

with $\Delta^{'}\mathrm{N}(\mathrm{E^i_{BGO}}) = \mathrm{N}(\mathrm{E^i_{BGO}}) - \mathrm{NE_{data}}\mathrm{NE_{mc}} \cdot \mathrm{N}(\mathrm{E^i_{BGO_{MC}}})$.

With these preparations, an iteration for the unfolding can be performed, then $N(E^i_{BGO})$ will be changed into $N^{'}(E^i_{BGO})$ as:

$$\begin{aligned} N^{'}(E^i_{BGO}) =& N(E^i_{T_{MC}}) \cdot \frac{NE_{data}}{NE_{mc}} + eN(E^i_{BGO}) + \sum_{k=1}^{m} f(|\Delta N(E^k_{BGO})|, \hat{\sigma}(N(E^k_{BGO})), \lambda) \\ & \Delta N(E^k_{BGO}) \cdot \hat{P}_{kj} + (1 - f(|\Delta N(E^k_{BGO})|, \hat{\sigma}(N(E^k_{BGO})), \lambda)) t \Delta N(E^k_{BGO}) \\ & \cdot \delta_{kj} \ , \end{aligned} \tag{3.43}$$

where $\hat{P}_{kj}$ represents the probability of one event that has the primary energy inside k-th bin of $E_{T_{MC}}$ and is observed in j-th bin of $E_{BGO_{MC}}$. $\hat{P}_{kj}$ has the same meaning with the $P(E^i_{T_{MC}}|E^j_{BGO_{MC}})$ in Bayes method. Equation. 3.43 can be used when $N(E_{BGO_{MC}})^k \neq 0$ and $N(E^k_{BGO}) - eN(E^k_{BGO}) > 0$, otherwise, equation 3.44 need to be used:

$$N^{'}(E^i_{BGO}) = \Delta N(E^k_{BGO}) \cdot \delta_{kj} \ . \tag{3.44}$$

We have a high quality of the MC simulation available in the analysis, which can well describe the data and detector response. Thus, we meet the conditions to use IDS method for unfolding the DAMPE data. The general procedures to use the IDS method can be described as follows:

1. Compute the $eN(E^k_{BGO})$ with equation 3.37 3.41 3.42 for each bin of the data. According to [89], the value of λ can be set as 5;
2. Compute the normalization factor with equation 3.38 for NE_{data} and NE_{mc};
3. Unfold the data with equation 3.43 or 3.44;
4. Check the unfolded results, if it is good enough, stop the iteration. if not, go to step 5 (The criteria for judging a unfolding result to be "good" is the same with the one used in the Bayes method, see text in the last part of section 3.3.1);
5. Update the normalization factor with 3.39;
6. Update the response matrix with:

$$A^{'}_{ij} = A_{ij} + f(|\Delta N(E^j_{BGO})|, \hat{\sigma}(N(E^j_{BGO})), \lambda) \cdot \Delta N(E^j_{BGO}) \cdot \frac{NE_{data}}{NE_{mc}} \cdot P_{ij} \ , \tag{3.45}$$

   A_{ij} represents the number of the events that are generated in i-th bin and transferred in j-th bin after the response of the detector. P_{ij} is the probability matrix which reflects the response effect of the detector, it can be calculated with equation 3.6. The way we update the response matrix can make the MC approach to the data without introducing a spurious fluctuations [89].

3.4 Methods validation with Monte Carlo simulation

The MC simulation can be used to validate the aforementioned unfolding methods. The idea is that a pseudo spectrum is simulated and used as an input spectrum (also called true spectrum) to the simulated DAMPE system. Therefore, an observed spectrum (or BGO spectrum) can be obtained by simulating the detector response. Basing on the same BGO spectrum, we use the three unfolding methods to reconstruct the energy of the simulated samples, thus, to obtain the reconstructed spectra, which are compared with the true spectrum. The differences between the reconstructed spectra and the true spectrum can be regarded as a reference for the performance of the unfolding method.

The AMS-02 proton result [35] are used to simulate the spectrum. In Fig. 3.3, the proton spectrum measured by AMS-02 is presented, where the blue line marks the fitting function (only concerning the hardening energy region, i.e. above 100 GeV) of the spectrum, and it can be written as:

$$\Phi = \mathrm{C} \cdot (\mathrm{E}/45)^{\mathrm{d}} \cdot [1 + (\mathrm{E}/\mathrm{E}_0)^{\Delta \mathrm{d}/\mathrm{s}}]^{\mathrm{s}} \ , \tag{3.46}$$

where E represents the energy, C is the constant item in the flux, it equals 0.4544 m^{-2} sr^{-1} $\mathrm{sec}^{-1}\mathrm{GeV}^{-1}$, s represents the smoothness of the transition of the spectral index d from -2.849 for energy below E_0 (336 GeV) to d + Δd (0.133) for energy above E_0. Equation 3.46 will be used to weight our MC proton samples, a simulated proton flux that can be described by equation. 3.46 can be obtained. The simulated proton spectrum is based on 12.8×10^8 MC samples. Half of the sample will be used to produce the response matrix which is the basis for all the three unfolding methods. The other half of the sample will be used as the input spectrum. As discussed in section 3.2, a group of selections are made on the events before the unfolding in order to reduce the uncertainty factors. The used selection are the same as we will use for selecting the proton + helium candidates in next chapter where a precise description on the cuts will be given. The response matrix after the selection is shown in Fig. 3.4, the counts of event have been normalized. The event numbers regarding different energy bins (the BGO spectrum) is shown in Fig. 3.5.

Based on the response matrix, the unfolding methods can be used to migrate the events among different energy bins. In Fig. 3.6, the change of the event number in each energy bin after the unfolding is presented.

The reconstructed spectra by the Bayes, SVD and IDS methods are shown in Fig. 3.7. The fluxes have been multiplied by a factor of $\mathrm{E}^{2.7}$ in order to enhance the visibility. All

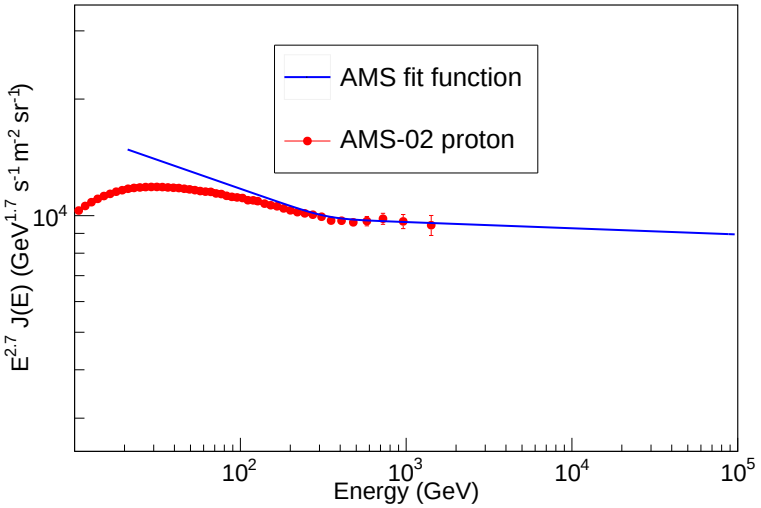

FIGURE 3.3: The CR proton spectrum measured by the AMS-02 experiment. The blue line marks the fit on the spectrum (equation 3.46, see text).

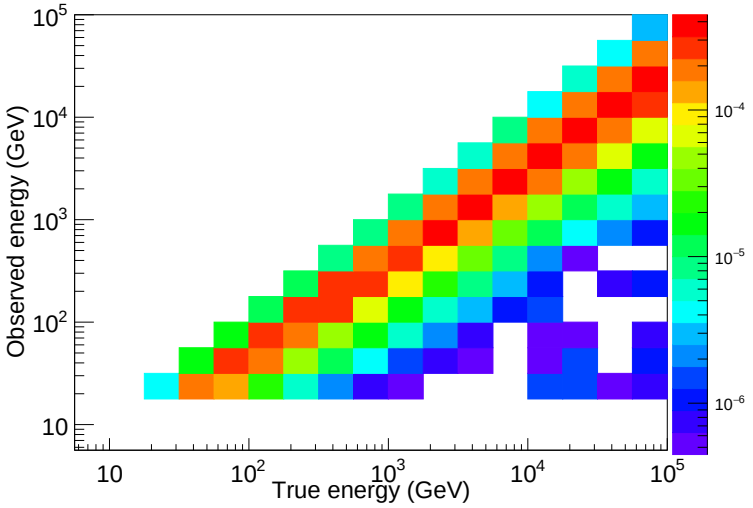

FIGURE 3.4: The response matrix of MC proton which is weighted according to the fitting function of AMS-02 proton flux.

the three methods can produce a spectrum that is close to the true spectrum (represented by the blue line).

The reconstructed spectra is divided by the value of the equation 3.46 at corresponding energies to check the divergence between the true and reconstructed spectra. The results is presented in Fig. 3.8. The spectral difference are within 5% for all the three methods, however, the Bayes method has a better behaviour with divergence less than 2% with the true spectrum.

The reconstructed spectra shown in Fig. 3.7 are the best results after tuning of various parameters of unfolding methods (For example, the spectral index of the MC samples used to produce the response matrix and the value of τ in the SVD method). These

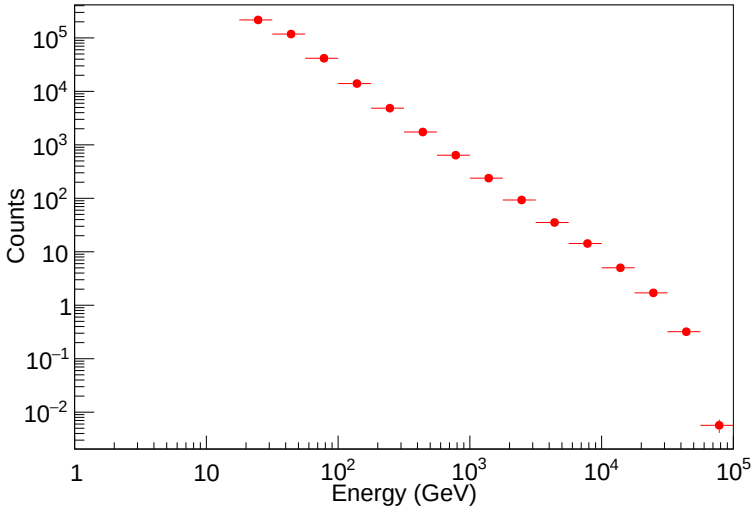

FIGURE 3.5: The event numbers in different BGO energy bins.

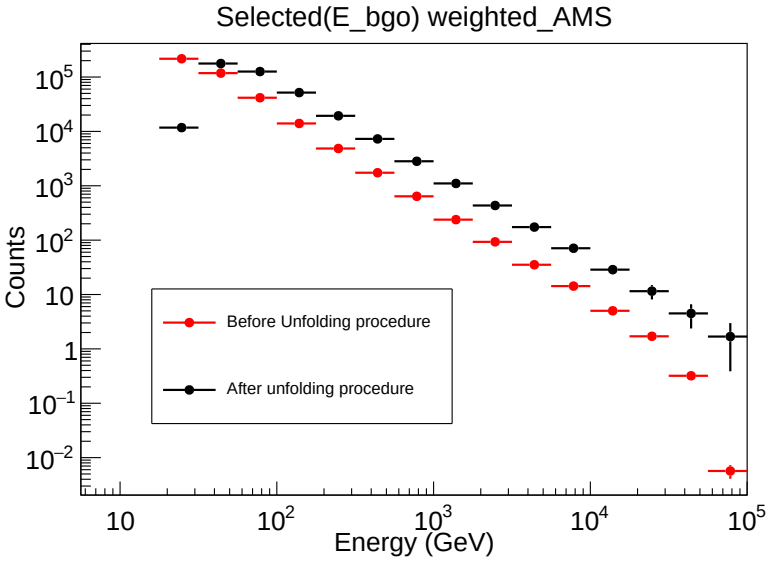

FIGURE 3.6: The event numbers in each energy bin before (red points) and after (black points) the data unfolding performed by the Bayes method.

types of parameters could affect the unfolding results and would be referred to as hyper parameters to distinct with these result from the unfolding. The idea for tuning a hyper parameter is to change its value and perform the unfolding process, then check whether the reconstructed spectrum is approaching to the true spectrum. The tuning process of the spectral index used to produce the response matrix will be presented to illustrate the processes for adjusting a hyper parameter. The Bayes method will be used in this example.

The response matrix (shown in Fig. 3.4) is the critical element of an unfolding method. Therefore, how to set the response matrix to obtain an optimal unfolding result is an issue of hyper parameter tuning. In Fig. 3.4, the response matrix is filled with the MC

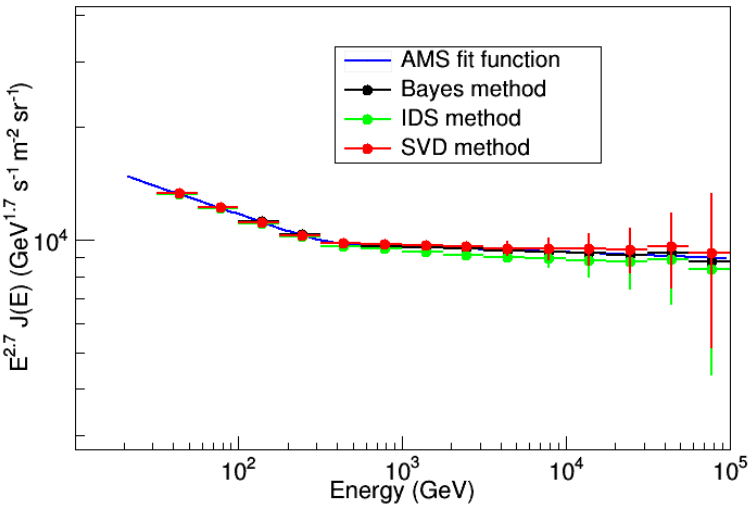

FIGURE 3.7: The reconstructed spectra by the three different unfolding methods. The blue line is from the equation 3.46, which reflects the true spectrum used in the simulation.

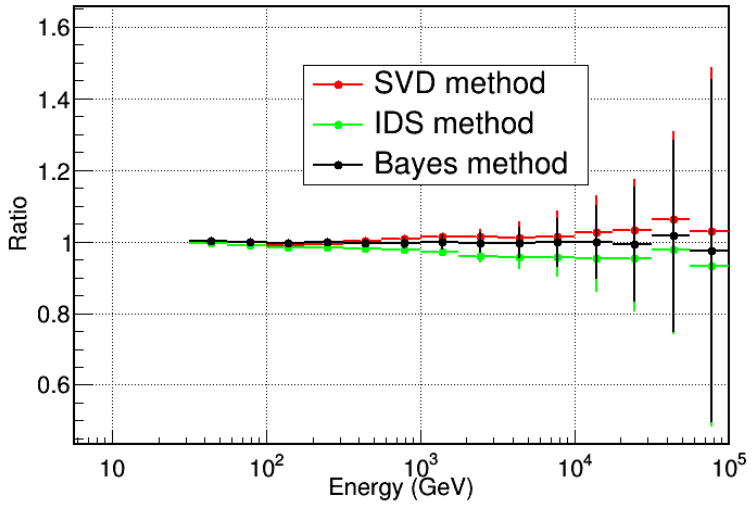

FIGURE 3.8: The ratios between the three reconstructed spectra and the true spectrum.

proton samples weighted with equation 3.46 which leads to a spectrum with index of -2.85 below the energy of 336 GeV and -2.72 above it. This index will be changed and the response matrix is refilled with the new spectrum. The impact of this change on the unfolding results (the reconstructed spectrum) will be the reference to adjust the parameter. We choose a single power law spectrum with index of -1, -2, -2.7, -3, -3.5 and -4 respectively to fill the response matrix, the reconstructed spectra are compared in two groups with -1, -2, -2.7 as one group since it is numerical larger than the index of the true spectrum (-2.72 – -2.85). The other group then includes the results from the indices of -3, -3.5 and -4.

The spectra reconstructed based on different response matrices, which are numerical less indices, are presented in Fig. 3.9. The ratios of the spectra over the corresponding

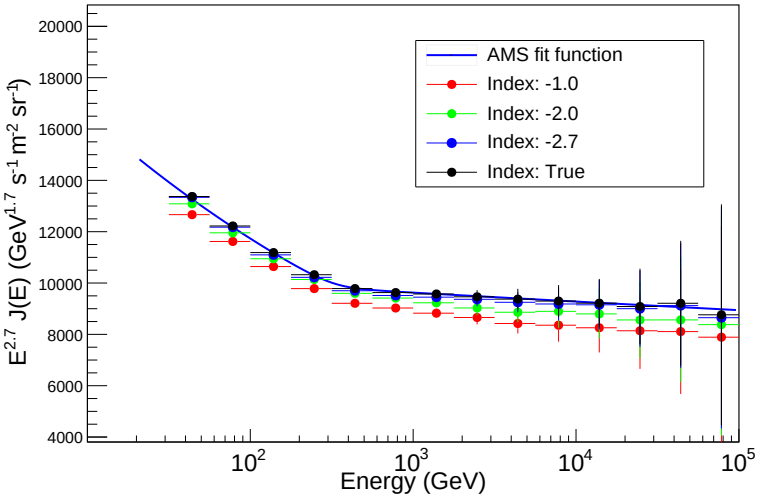

FIGURE 3.9: The reconstructed spectra based on various response matrices with the spectral index of -2.7, -2 and -1. The Bayes method is used as the unfolding method.

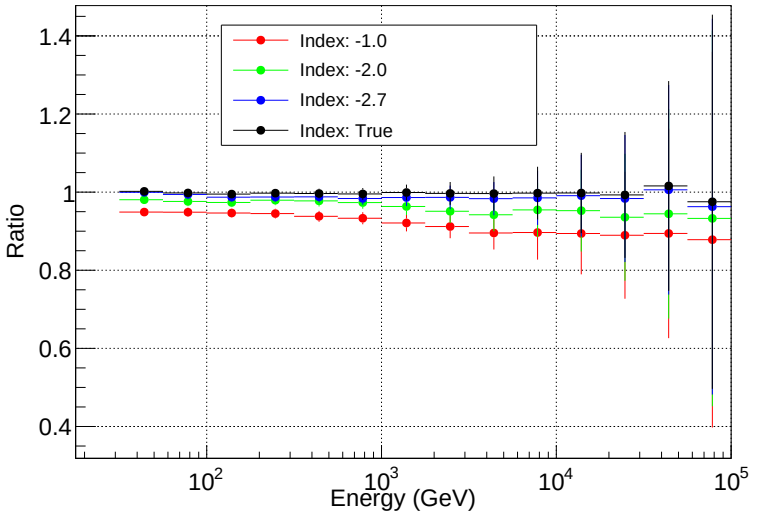

FIGURE 3.10: The ratio of the spectra reconstructed by the response matrices with numerical larger indices over the values of the function used to produce the spectrum.

values of the spectrum function (equation 3.46) is plotted in Fig. 3.10. The ratios show that the best result comes from the one that are using the same spectral index with the true input spectrum. This is plausible, however, we do not know the true spectrum in practice. An alternative solution is to use a spectral index in the response matrix close enough to the true one. For example, in Fig. 3.9, if the response matrix is filled with the spectrum with index of -2.7, then the reconstructed result has only a minor divergence with the true spectrum (within 1%). In reality, the "closer" index could come from the measurements of precedent experiments, thus the systematic uncertainties due to the response matrix can be reduced.

The other set of the spectra reconstructed by the response matrices with spectral index of -3, -3.5, -4 are shown in Fig. 3.11. The ratios with the spectrum function (equation

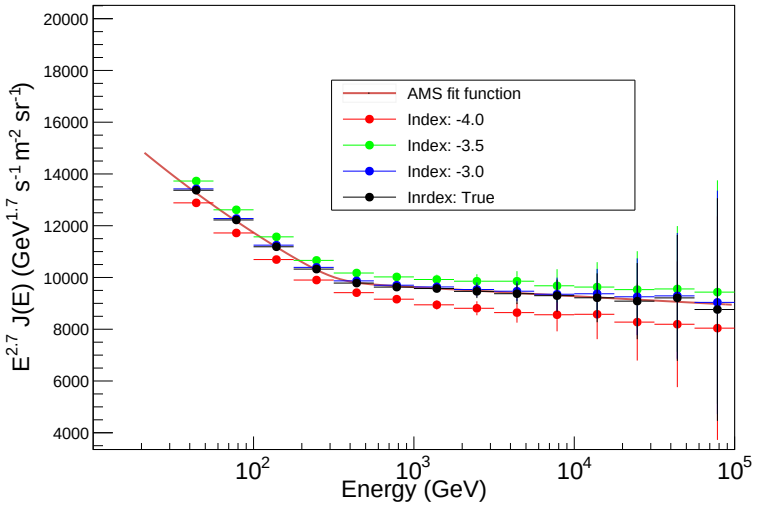

FIGURE 3.11: The reconstructed spectra based on various response matrices with the spectral index of -3, -3.5 and -4. The Bayes method is used as the unfolding method.

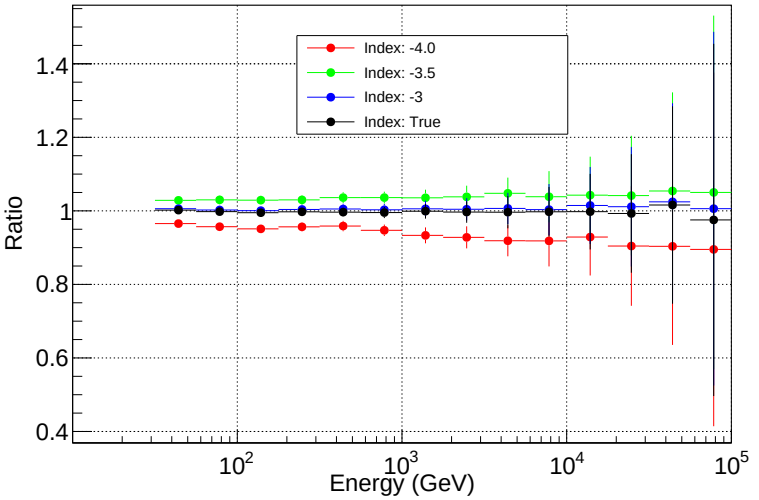

FIGURE 3.12: The ratio of the spectra reconstructed by the response matrices with numerical less indices over the values of the function used to produce the spectrum.

3.46) are presented in Fig. 3.12. An analogous situation with Fig. 3.10 is founded in this case: a better result can be obtained if the spectral index in response matrix is closer to the true spectral index.

Through the discussion in this section, the Bayes unfolding method is proved to have a better performance (with a spectral biases less than 2%) than the other two methods (with spectral biases within 5%) as shown in Fig. 3.8. However, since in this section, only MC sample is used to test the methods, it will be more convincing if the Bayes method can be validated with some real data as well. In next section, the beam experiment data will be used to test the Bayes method as an additional validation.

3.5 Test on the Bayes method with beam data

A full prototype of the DAMPE detector was exposed to several types of beams in the CERN north area. In this section, the proton beam data with energies 150 GeV and 400 GeV will be used to test the performance of the Bayes unfolding method.

3.5.1 Energy reconstruction on the 400 GeV proton beam

For the 400 GeV proton beam test, two entering angles of the beam were used: one follows the direction of Z axis of DAMPE coordinate system, which is perpendicular to the BGO surface. The other one has an angle of 15° with the Z axis. Both beams impinged on DAMPE from the center point of the PSD. An corresponding simulation was performed for the Z direction proton beam. The energy scale of DAMPE sub-detectors were calibrated by using of MIP events [59], therefore, the distribution of MIP events in each BGO layer can reflect the quality of its calibration. In Fig. 3.13, the MIPs distribution (from the 400 GeV proton beam data) in the first four BGO layers are plotted together with the corresponding MC. The distributions are fitted with a Landau function convoluted with a Gauss function, which will be referred to as Lan-Gaus function. The fit results show that there is a fair agreement between the data and MC in each layer of the BGO indicating the reliability of the reconstruction procedures.

As it has been done in section 3.4, a selection on the events is performed before starting the unfolding process. After the selection, the distributions of the deposited energy for data and MC are presented in Fig. 3.14. Based on the selected data, the Bayes method are used to reconstruct their primary energies.

The response matrix as the same with in Fig. 3.4 but change the weight from the AMS-02 to a flat distribution (spectral index equals to 0)are used for the unfolding process. Since the primary energy of the beam events are unique (400 GeV), if a response matrix produced by the spectrum with index of -2.7 is still used, a larger bias would be caused (as discussed in section 3.5). Besides, the $P_0(E_T^i)$ in equation 3.5 is set as an unique value as:

$$P_0(E_T^i) = \begin{cases} 1 & E_T = 400 \text{ GeV} \\ 0 & E_T \neq 400 \text{ GeV} \end{cases}, \tag{3.47}$$

to adjust the unique energy situation.

With these preparation, the Bayes unfolding can be performed based on the distributions shown in Fig. 3.14. The unfolded results for MC and data are presented in Fig. 3.15. For the MC, after the unfolding, the mean value of the distribution is 402.3 GeV with

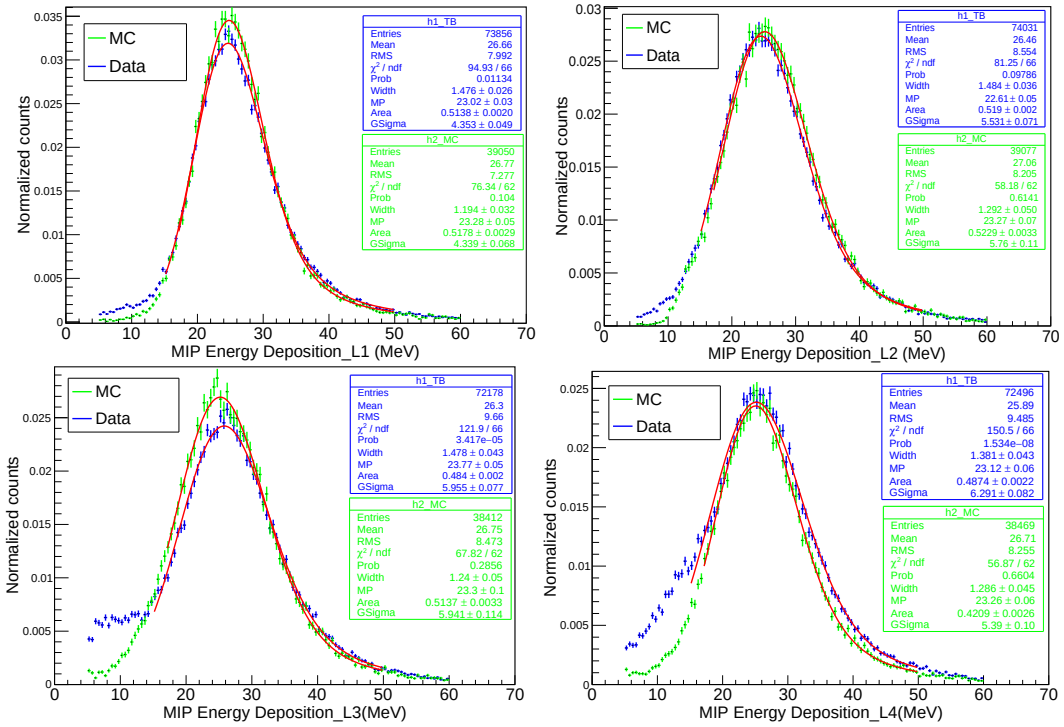

FIGURE 3.13: The distributions of MIP events in the first four layers of the BGO calorimeter. Both the 400 GeV proton beam data and MC are shown.

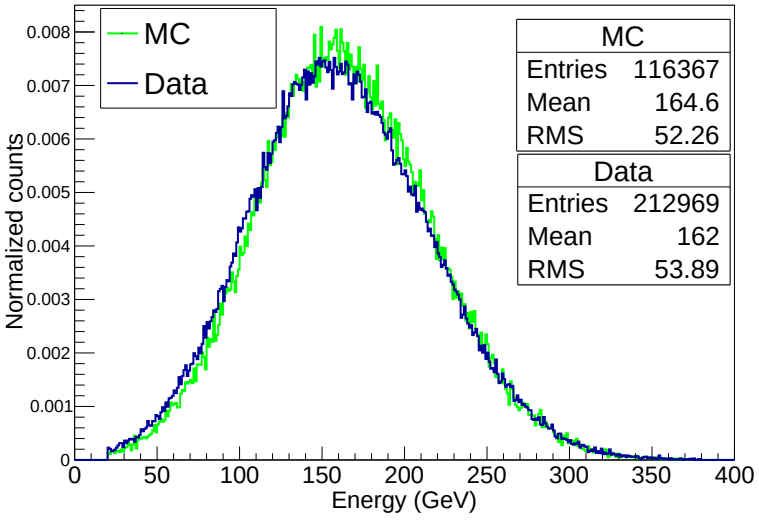

FIGURE 3.14: The distribution of the BGO energy for the 400 GeV proton beam of both MC and data. The beam direction is perpendicular to the PSD surface (following the Z axis of the DAMPE coordinate system).

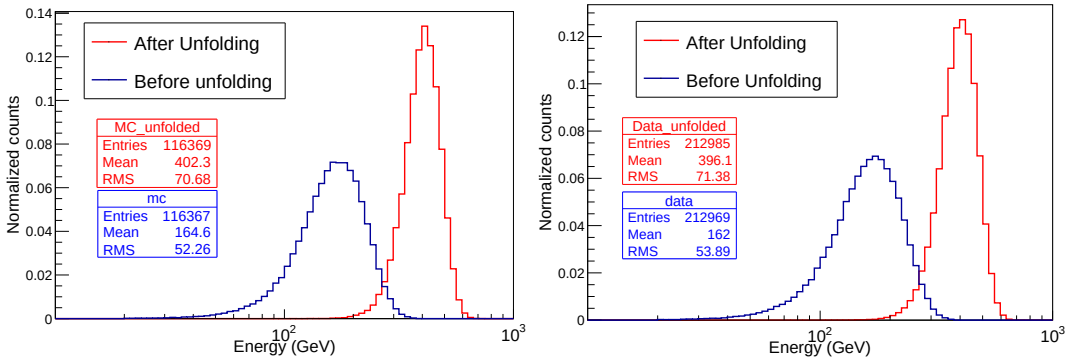

FIGURE 3.15: The energy distributions for the MC (left) and the data (right) of the 400 GeV proton beam before and after the unfolding procedures.

only 0.5% drift from its true value of 400 GeV. For the data, the mean value of the distribution after unfolding is 396.1 GeV, the drift is $\sim$ 1%. We can roughly calculate the energy resolution by dividing the mean value with RMS value shown in the Fig. 3.15. For the MC, the energy resolution after unfolding is $\sim$ 17%, the energy resolution of the data is $\sim$ 18% after unfolding. The resulting resolutions are in agreement with the BGO simulation performed along the whole energy measurement range (see Fig. 2.20). This result illustrates that the Bayes unfolding method can reconstruct the energy of hadron with a good accuracy.

The BGO energy distribution and the unfolded result for the data of 400 GeV proton beam with 15° incident angle are presented in Fig. 3.16. The unfolding method can reconstruct its energy with high accuracy (with bias of $\sim$0.5%) as well. Compared with the perpendicular incident beam (blue histogram in the right of Fig. 3.15), the 15° beam data before unfolding is even with less RMS and larger mean value. This is due to the fact that when beam particles enter the detector with a given angle, their path length inside the BGO is longer than the perpendicular incident particles, therefore, a larger ratio of their primary energy can be collected.

3.5.2 Energy reconstruction on the 150 GeV proton beam

DAMPE performed a beam test with 150 GeV protons as well. The incident angle of the 150 GeV beam is perpendicular to the surface of the PSD (following the Z axis). In order to perform the unfolding procedures on the 150 GeV proton beam data, the response matrix used here is filled with a proton spectrum with spectral index of 0 which is a flat spectrum (the same with the one used in section 3.5.1 for the 400 GeV proton

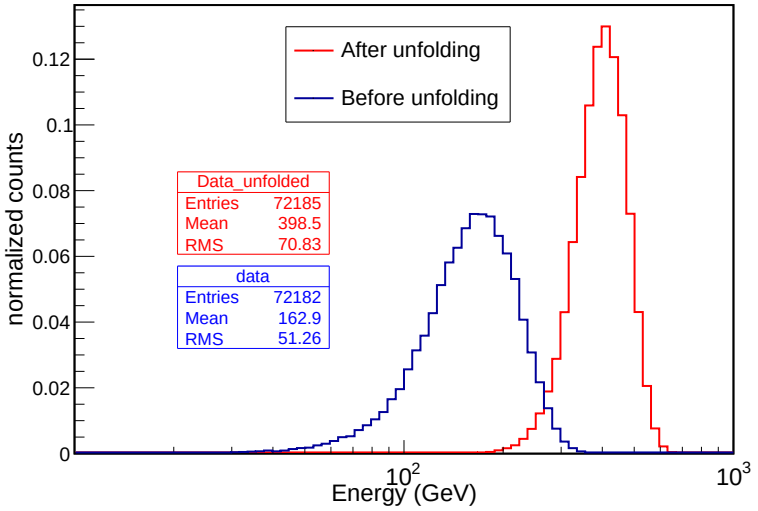

FIGURE 3.16: The energy distributions for the 400 GeV proton beam with 15° entering angle before and after the unfolding procedures.

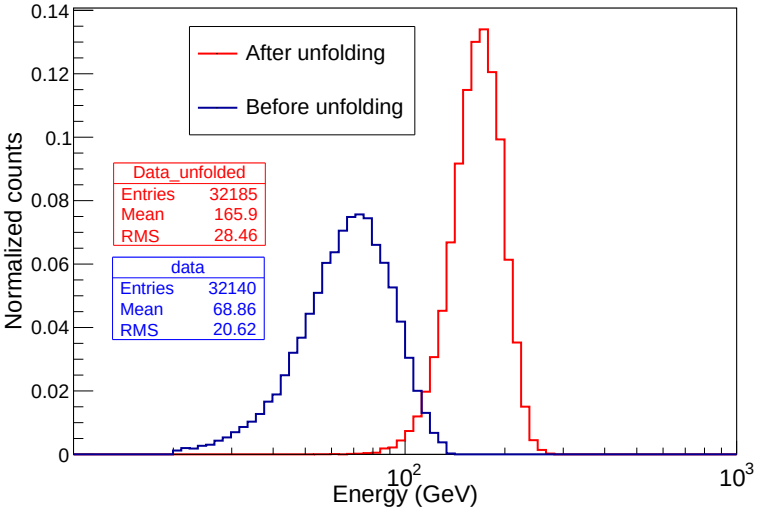

FIGURE 3.17: The energy distributions for the 150 GeV proton beam data before and after the unfolding procedures.

data). The prior probability $P_0(E_T^i)$ in equation 3.5 is set as:

$$P_0(E_T^i) = \begin{cases} 1 & E_T = 150 \text{ GeV} \\ 0 & E_T \neq 150 \text{ GeV} \end{cases} . \tag{3.48}$$

In Fig. 3.17,the energy distributions of the data before and after the unfolding are presented. The mean value of the reconstructed data has a non-negligible shift of 16 GeV compared with the incident energy (150 GeV). Since the reliability of the Bayes method has been tested with both MC and the 400 GeV proton beam data, the potential problems in data calibration are first considered as the reason that results in this energy shift.

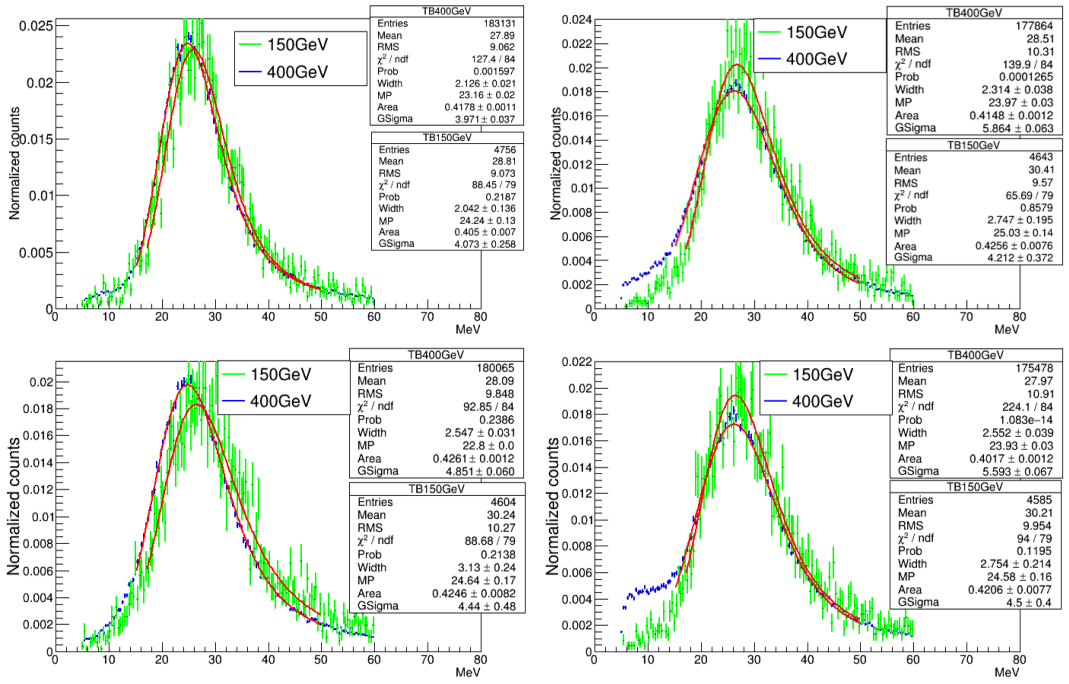

FIGURE 3.18: The MIP distributions of the first four BGO layers. The blue points represent the 400 GeV data set, while the green points represent the 150 GeV data set. Since we have less events from the 150 GeV beam data, the corresponding statistics errors are larger.

A poor calibration leads to an incorrect energy scale of the detector thus causing an erroneous energy measurement. The calibration on the BGO energy scale are fulfilled by using of the distribution of the MIP signals in each layer. Since the deposited energy of a MIP event is roughly independent from their primary energy, and the correctness of the MIP distributions from the 400 GeV proton beam has been proved through the MC (Fig. 3.13), therefore, the 400 GeV MIP data can be used to cross check the calibration of the 150 GeV beam data. The MIP distributions of the 150 GeV and 400 GeV proton beam for the first 4 BGO layers are presented in Fig. 3.18. By fitting the distributions with the Lan-Gaus function, a disagreement between the two sets of the data can be found. In Fig. 3.19, the Most Probable Values (MPVs) and σ of the fitting for all 14 layers of the BGO are presented. Since the fitting function contains both Gauss and Landau functions, the σ in this case is calculated as:

$$\sigma = \sqrt{\sigma_{\text{Gaus}}^2 + \sigma_{\text{Lan}}^2}\ , \tag{3.49}$$

where the σ_{Gaus} and σ_{Lan} represent the sigma of the Gauss and Landau distributions respectively.

The divergence of the MIP distributions between the 150 GeV beam data and the verified 400 GeV beam data indicates a calibration problem which can be the reason for the incorrect reconstructed energy of 150 GeV beam data (as shown in Fig. 3.17).

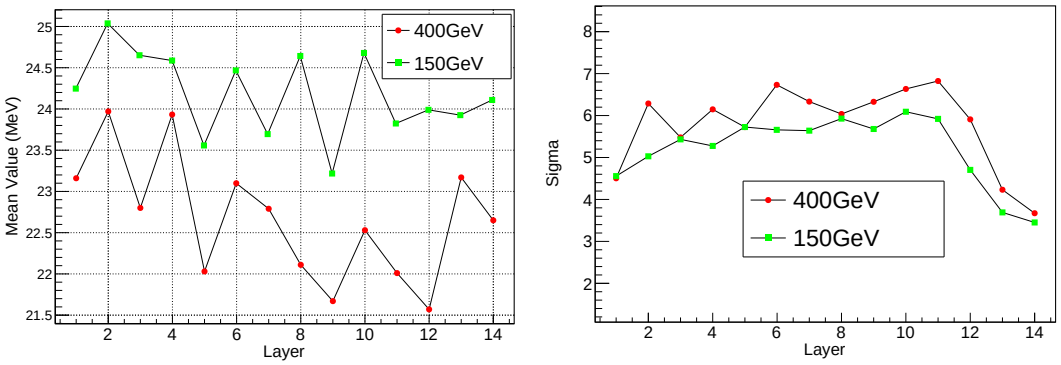

FIGURE 3.19: The MPV (left) and σ (right) of the MIP distribution for each layer of the BGO.

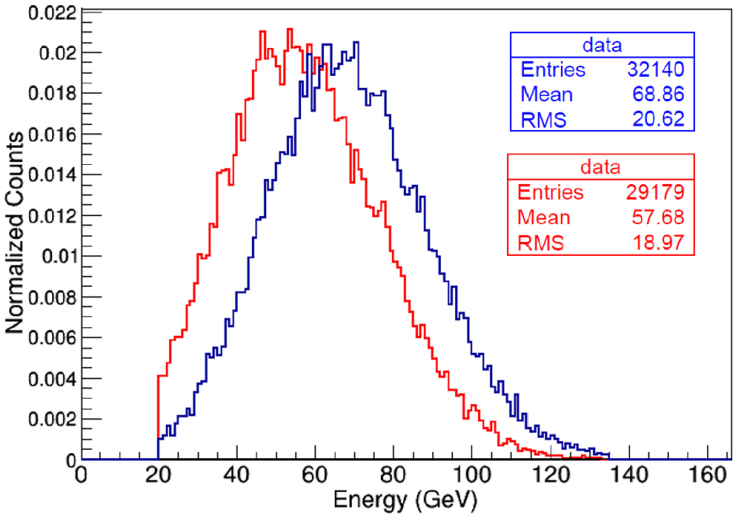

FIGURE 3.20: The distributions of the total deposited energy for 150 GeV proton beam data before (blue) and after (red) the energy correction.

Through the comparison of the MIP distributions (Fig. 3.19), the quantity of the energy scale shift for each BGO layer can be obtained, which provides a method to correct the deposited energy for each event. The correction can be done layer by layer by multiplying a factor which equals the ratio of the MPVs of 400 GeV beam and 150 GeV beam MIP distributions (the values of the MPV for each BGO layer are shown in the left of Fig. 3.19). After the correction, the distribution of the deposited energy of the 150 GeV beam data is presented in Fig. 3.20 (the data before the correction is also presented to have a comparison). Performing the unfolding on the corrected data, the unfolded result is shown in Fig. 3.21. The mean value of the reconstructed energy after the correction is 154.1 GeV with a minor shift of 2.7% from the incident energy (150 GeV). The RMS of the reconstructed energy is 17.83% which is also consistent with the simulation as shown in Fig. 2.20.

The reliability of the Bayes method has been proved from the unfolding results of the 400 GeV and 150 GeV proton beam data. The energy reconstruction of the 400 GeV

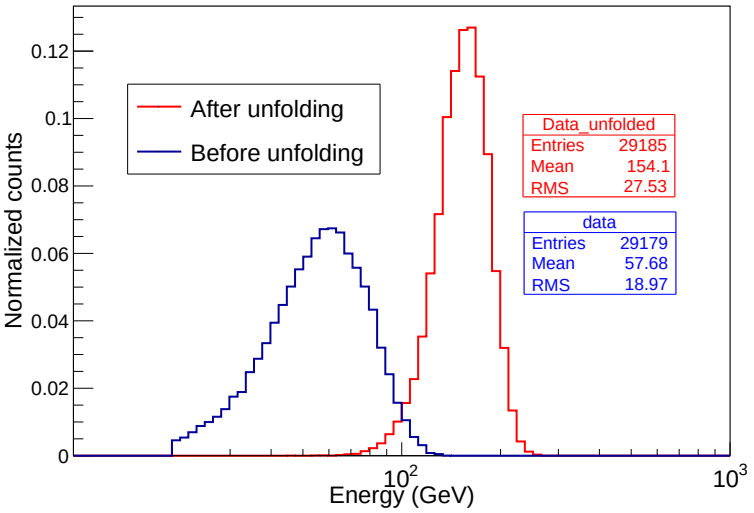

FIGURE 3.21: The unfolded result for the 150 GeV beam data after the correction on the deposited energy,

beam with different incident angles shows that the method can work properly for the particles entering the detector with various angles. The unfolding-correction-unfolding-again routine for the 150 GeV data illustrate that as long as the acquired data is reliable, the Bayes method can always reconstruct the primary energy of hadrons precisely.

3.5.3 Summary

In this chapter, we first introduced the features of a hadronic shower. Due to the shower shape and leakage, only 30% - 40% of hadron primary energy can be collected in the BGO calorimeter and the deposited energy is with a large fluctuations. These factors impose challenges on hadron energy reconstruction. In order to measure the energy spectrum of cosmic ray proton and nuclei, a precise measurement on the primary energy is highly demanded. Three unfolding methods (discussed in section 3.3) were studies and tested by reconstructing a MC pseudo spectrum (section 3.4). The results showed that the Bayes method could reconstruct the primary energy of hadron particles with minimum biases. In order to have a further validation on the Bayes method with some real data, the proton beam data with primary energies of 400 GeV and 150 GeV were used. The unfolding results of 400 GeV beam data showed that the Bayes method could precisely reconstruct its primary energy. Though the unfolding result of the 150 GeV beam data presented a shift of around 10% from its incident energy, it turned out that it was due to the calibration issue of the BGO. After the correction on the energy, the unfolding result has only a minor drift ($\sim$ 2.7%) regarding the incident energy of the beam.

Given the results of various tests and validations, the Bayes method showed its capacity on reconstructing the energy of hadron particles with good accuracy. Therefore, the Bayes unfolding method will be used for reconstructing the primary energy of CR proton + helium nuclei in the next chapter.

Chapter 4

Measurement of the Cosmic-Ray proton + helium flux

Various observations of galactic CR spectra have revealed a deviation from the single power law feature. For instance, a spectral hardening at ∼300 GeV/n have been observed by PAMELA [98], AMS-02 [35, 36], CALET [38] and ATIC-02 [99] for hadronic spectra. At higher energy (between 1 TeV and 100 TeV), several observations on proton spectrum also show a spectral softening (As described in chapter one). However, more measurements on this energy range are needed to enhance our understanding of the spectrum features. Thanks to the thick, fine-grained calorimeter and its large acceptance, DAMPE can cover the energy region up to 100 TeV with good statistics and limited systematic uncertainties. In this chapter, the spectral measurement of CR proton (H) + helium (He) with energy up to 100 TeV will be discussed. Selecting H + He nuclei has advantages of almost no background and very high purity. As it was shown in chapter one, the proton flux measured by DAMPE revels a spectral softening at around 13 TeV, the H + He spectrum could help to have a further study on this spectral feature. Selecting H or He candidates separately requires more stringent selections than picking up H and He nuclei together, thus, a more reliable result can be obtained with H + He spectrum. The light nuclei spectrum could be used as a cross check for H and He spectrum. Moreover, since the DAMPE light nuclei spectrum can reach such a high energy , a comparison on the H + He spectra between the direct and indirect measurements can be performed.

In section 4.1, the equation for computing the spectrum will be introduced. As one of the main components of the equation, the detector exposure time and its calculation will be described in section 4.2. The MC simulation for DAMPE plays an essential role in measuring a CR spectrum, as well as the used hadronic interaction models. They

will be introduced in section 4.3. In section 4.4, we will explain the used selection cuts for selecting the H + He candidates. The corresponding efficiencies and the effective acceptance will be presented in section 4.6 and section 4.5. In section 4.7, the energy reconstruction by using the Bayes unfolding method (introduced in chapter three) for H + He candidates will be discussed. Finally, in section (4.8), the H + He spectrum with the systematic uncertainties will be shown, along with some comments on spectral features and comparison with other analogous measurements.

4.1 Introduction on flux measurement

The differential flux Φ of CR H + He nuclei with energy inside the interval of $[E, E + \Delta E]$ is computed as follows:

$$\Phi(E, E + \Delta E) = \frac{N_{H+He}(E, E + \Delta E)}{\Delta T \cdot A_{acc} \cdot \Delta E}, \tag{4.1}$$

where $N_{H+He}(E, E + \Delta E)$ is the number of selected H + He candidates with their energy being reconstructed (see section 4.7 for more details), and ΔT is the exposure time for DAMPE collecting data (see section 4.2). Furthermore, A_{acc} is the effective acceptance, which is derived from Monte Carlo (MC) simulations as the product of geometric factor and selection efficiencies (see section 4.6). Finally, ΔE is the width of the energy bin. In this analysis, each bin has equal width in logarithm scale, and for each decade, there are 5 bins. The equation 4.1 can be derived as each component being known. The calculation of these components is discussed in the following sections.

4.2 Computation of the detector exposure time

In this analysis, the used on-orbit data (simply referred as "data", meanwhile the MC data will be mentioned as "MC" for distinction) were taken in the period from first of January, 2016 to 31st March, 2019. In Fig. 4.1, the cumulative number of events collected by DAMPE during this period is presented. On average, DAMPE can collect about 5 million events every day. The effective data-collecting time (so-called exposure time), is computed by subtracting the contribution of event-non-recording time (dead time) from the total on-orbit time.

One of the main contributions to the dead time is the period when DAMPE passed through the region known as the South Atlantic Anomaly (SAA), an area with reduced magnetic intensity [100], where the inner radiation belts (Van Allen belts) come close to the surface of the Earth. This leads to the fluxes of protons and electrons (with energies

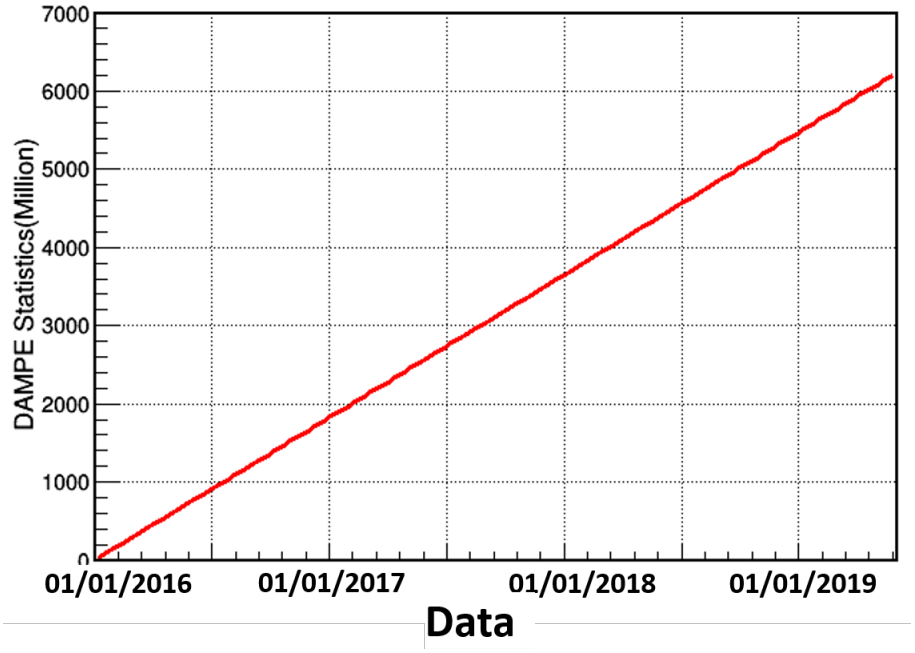

FIGURE 4.1: The accumulative number of events as function of time for DAMPE. The time period of the data used by this analysis ends at March 2019.

lower than 100 MeV mainly) captured by the geomagnetic field being two times higher than the fluxes outside of this region [101]. SAA has an obvious impact on satellites with lower height orbit [102]. DAMPE is with a orbit altitude of 500 km, and will cross SAA 6 or 7 times per day. The energies of most particles in SAA are lower than the trigger threshold energy of DAMPE [26], so the data acquisition system will not be activated. However, the electronic system can not recover efficiently enough with such a large amount of charged particles hitting the detector so frequently. As a result, the electronic baseline of each data channel becomes abnormal, which leads to an increasing electronic noise. The behavior of two PSD electronic baselines inside and outside of SAA region are presented in Figs. 4.2. To avoid the uncertainty associated to the SAA region, the events collected in this area have been removed. The contribution of this deduction accounts to 4.5% of the total time. The determination of the boundary of SAA region can be found in [59].

Besides SAA, the other factors that contributes to the dead time includes:

- The response time of DAMPE electronics. When DAMPE is under the normal observation mode, the data acquisition system needs 3.0725 ms for each entering particle to finish reading and storing their signals, then recover the electronics of the detector unit preparing for next collection. During this period, the trigger system will be vetoed with no response to upcoming particles. Since the general

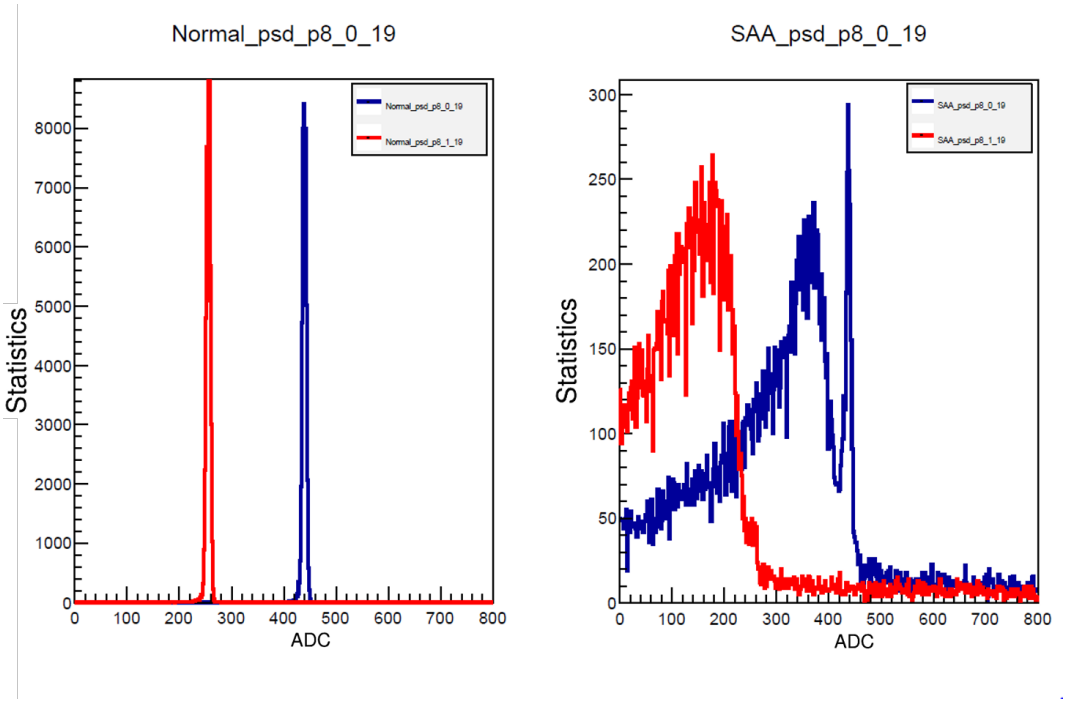

FIGURE 4.2: Example of two channels of the PSD electronic baselines (red and blue lines) when the satellite flying inside the normal region(left) and inside the SAA region (right). An obvious abnormality with large noise can be found in the baseline obtained in the SAA region.

trigger rate of DAMPE is around 70 Hz, the corresponding dead time accounts for 18% of the total time.

- The on-orbit calibration. An on-orbit calibration of each sub-detector is performed every day in order to guarantee a high quality of the measurement [59]. The calibration includes: the STK baseline calibration (30 times per day, each of them lasts 40 s); The PSD, BGO and NUD baseline calibrations (once per day, each lasts 100 s). Moreover, a calibration on the electronics linearity for every sub-detector is carried out once per month standing 30 minutes. During the calibration operations, the trigger system is shut off, thus the dead time due to the calibrations represents 1.8% of the total time.

To sum up, the event-recording time accounts for 75.54% of the total operation time. Moreover, we have excluded the days of 8-13 September, 2017 due to an intense solar flare and the days of 29-30 December, 2017 due to high voltage reset in DAMPE. Consequently, the total exposure time in this analysis equals 5.9×10^7 s, which is equivalent to $\sim$ 683 days.

4.3 Monte Carlo simulation

MC simulation plays a crucial role in measuring a CR spectrum due to the fact that an accurate simulation for detector system will help in understanding the detector response and computing the acceptance precisely. The DAMPE MC simulation is performed mainly with the GEANT4 tookit [71, 103]. Two widely used models are adopted for high-energy hadronic interactions: Quark-gluon String with Precompound (QGSP) model [104] and Fritiof String with Precompound (FTFP) model [105]. In particular, for H samples with primary energy of E $<$ 100 TeV and He samples with primary energy of E $<$ 200 TeV, two physics lists in GEANT4 based on the mentioned string models are used: FTFP_BERT and FTFP_QGSP_BERT. We will refer to them as FTFP and QGSP for simplicity. For proton samples with primary energy of 100 TeV $<$ E $<$ 1 PeV, the simulation combines DMPJET [106] and FTFP models with Cosmic Ray Monte Carlo (CRMC) package [107]. In addition, the FLUKA [108] toolkit is also employed to produce H samples that are used as a cross check for the other simulation.

In order to decide which model between the QGSP and FTFP should be used as default, some comparisons are made based on the model behaviours in different scenarios. In Fig. 4.3, the comparison between the 400 GeV proton beam data and its MC counterparts with both FTFP and QGSP models are shown. At low energy region (E $<$ 200 GeV), both FTFP and QGSP of MC have a good agreement with the beam data (discrepancy within 5%). As the energy increases, the difference between QGSP model and beam data rises to $\sim$ 25% at 300 GeV (the particle deposited energy or BGO energy). Meanwhile, the difference between the FTFP model and beam data is within $\sim$ 10%. Thus the FTFP model describes better the beam data. In addition, a cross check between GEANT4 and FLUKA simulations is also carried out by comparing their energy deposition in the calorimeter. The comparison procedures are as follows: for both GEANT4 and FLUKA samples, the distributions of the ratio between primary and deposited energy in the BGO are obtained regarding different energy bins. The proton samples with primary energy between 2511.89 GeV and 3981.07 GeV is shown in Fig. 4.4 as an example. The distribution is fitted with a reformed Gauss distribution. The mean values of the fit for different energy bins and MC sets (the FTFP, QGSP and FLUKA based result) are compared as shown in Fig. 4.5. The comparison shows that the behaviour of FTFP model agrees better than QGSQ model with the FLUKA simulation.

The MC proton samples with primary energy between 100 TeV and 1 PeV are generated with the CRMC package [107] by using of a dynamic model-invoking mechanism: the DPMJET model is used when a particle deposits energy more than 300 GeV in the BGO. Otherwise, the FTFP model is used. The energy-deposition ratio regarding primary energy (as the same with in Fig .4.5) for FTFP and CRMC-based samples is shown in

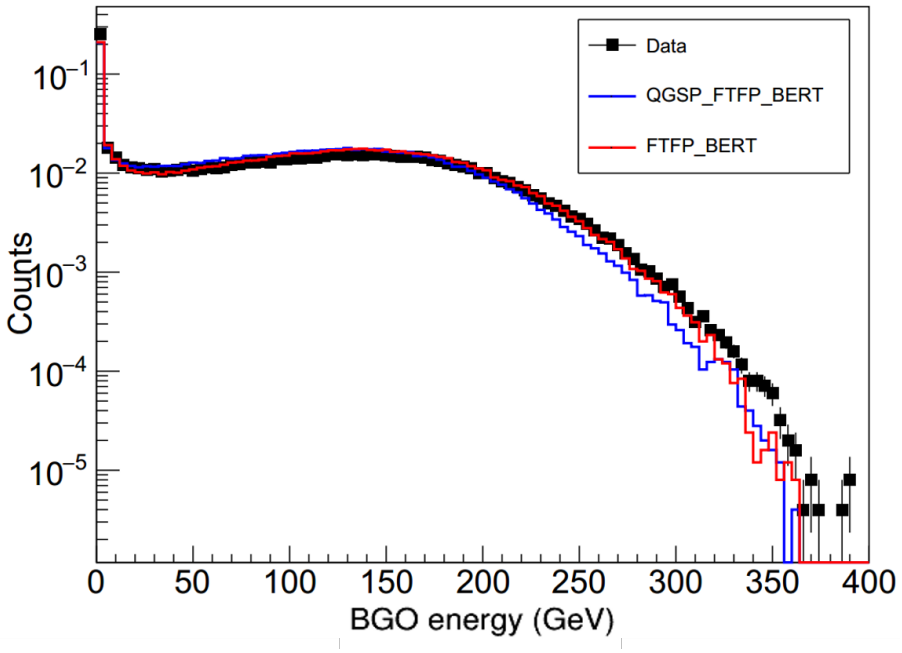

FIGURE 4.3: Energy deposition in the BGO for the 400 GeV proton test beam data and the MC simulations with FTFP and QGSP models. A normalization is made regarding their statistics to have a clear comparison.

4.6. In the overlapping energy region (between 100 GeV and 100 TeV), these data sets are in good agreement.

Considering the aforementioned comparisons above, we decided to use the MC samples based on the FTFP model at energy E $<$ 100 TeV for protons and E $<$ 200 TeV for helium. At higher energy range (between 100 TeV and 1 PeV), the MC proton samples based on DPMJET + FTFP models produced by CRMC package are used.

4.4 Selections of the proton and helium samples

Before using the collected CR events to produce the spectrum, a selection procedure on both MC and data is required to distinguish high-quality candidates of H and He particles, so that a more accurate measurement can be made. For instance, the arrival directions of galactic CRs are highly isotropic, entering particles with their shower inside the BGO being not well contained could provide misleading information and enlarge the uncertainty for energy reconstruction (as discussed in chapter three). Therefore, these events should be removed. Moreover, to a more basic level, the CRs contains not only H and He nuclei, thus, a selection based on the category of particles is also necessary. Generally speaking, the applied selection cuts include: pre-selection, BGO-STK match, STK-PSD match, trigger and charge selection. Each of them will be introduced in the following sections.

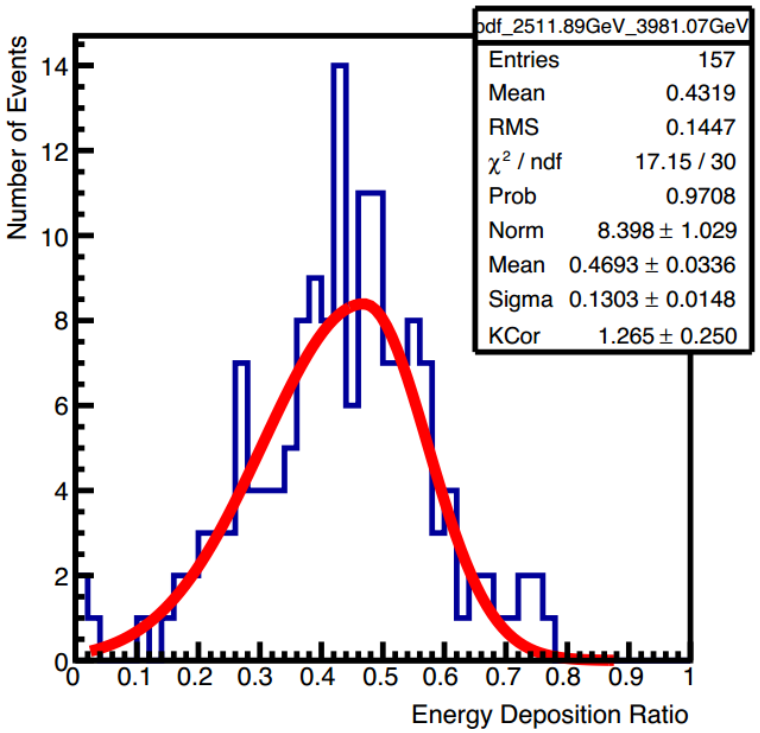

FIGURE 4.4: The distribution of the ratio between the deposited energy and primary energy for FLUKA simulated proton samples with primary energy between 2511.89 GeV and 3981.07 GeV. The red line is the fit function.

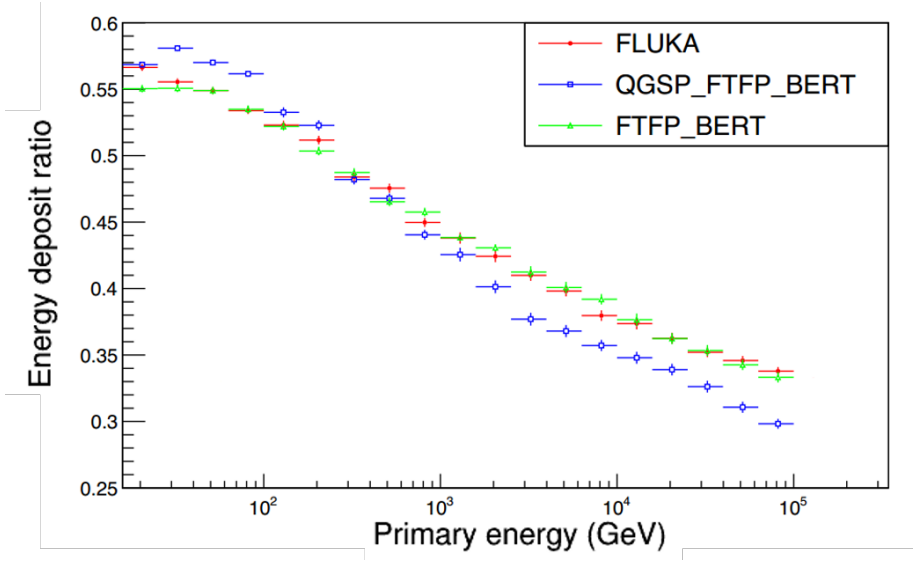

FIGURE 4.5: The energy deposit ratios in the BGO with respect to the primary energy for GEANT4 FTFP (green triangles), QGSP (blue squares) and FLUKA (red points). The FTFP model and FLUKA results are in a good agreement (with difference $< 2\%$), and a lager discrepancy can be found with the QGSP results (with difference $\sim 10\%$).

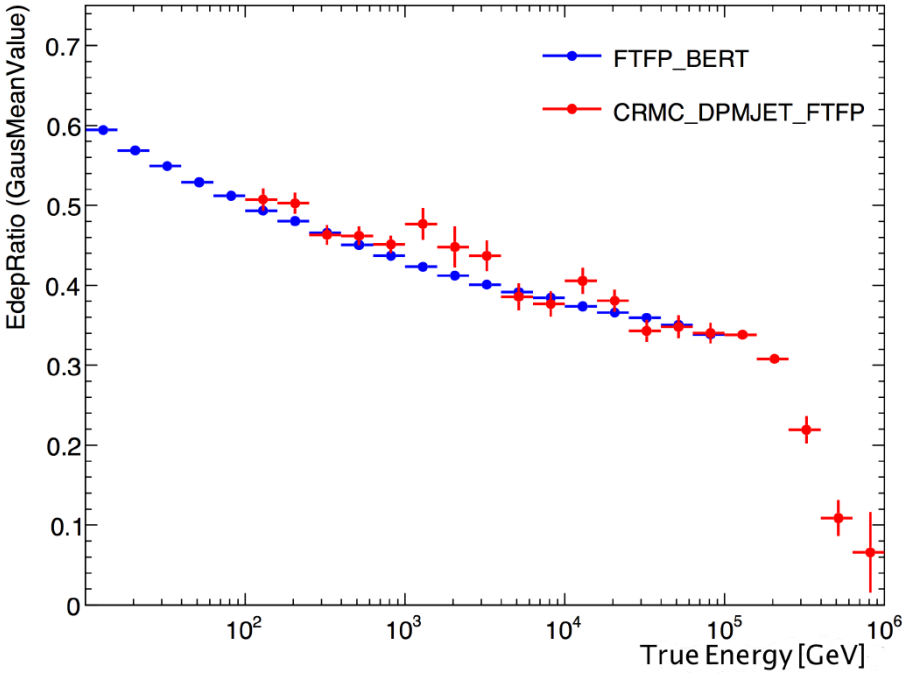

FIGURE 4.6: Fractions of the deposited energy in the BGO computed from the FTFP (blue solid) and CRMC (red solid circles) models.

4.4.1 Pre-selection cuts

All the triggered events are first selected by the pre-selection cuts, which are based mainly on the BGO measurement. The pre-selection guarantees that the shower of an incident particle are well contained by the calorimeter and removes the events that are influenced by the geomagnetic cutoff [109]. In particular, for each event, the selection cuts require:

- The deposited energy in the BGO has to be larger than 20 GeV. This selection effectively avoids the influence of the geomagnetic rigidity cutoff on the H + He candidates;
- The reconstructed track by the BGO must be fully contained in the calorimeter, i.e., to be inside [-280mm, 280mm] in x-axis and y-axis, and inside [46mm, 448mm] in z-axis of the DAMPE coordinate system. Setting this constraint on the span of the BGO track ensures the shower of the event being well-contained and removes events entering BGO from the detector side;
- The largest energy deposition in a single layer of the BGO should be less than 35% of its total energy deposition. This is to enhance the rejection power for side-incident particles;

- For the top three layers of the BGO, the bar with the largest energy deposition must not be the edge bar of that layer. This cut avoids particle showers being initialized at corner of the BGO.

4.4.2 Track reconstruction and selection cuts

The track of an entering particle is reconstructed by the STK by using a Kalman filter algorithm [3, 110]. Due to pre-showering and back-scattering of particles, normally there will be more than one track being reconstructed for an event. A best track is selected among the reconstructed tracks of an event. The selection is performed by searching a STK track that matches BGO track the most and is compatible with PSD measurement. Specifically, a selected STK track must meet the following conditions:

- The track is reconstructed with $\chi^2/ndof$ lower than 25 to ensure reconstruction quality;
- The track must have at least one cluster in X or Y layer of the first STK plane to ensure an additional charge measurement.

The selections above are based on STK itself. Besides, the track have to be matched with the BGO and PSD measurements. First, four selection cuts are performed for the STK-BGO match:

- The angle between the STK track and BGO track must be less than 25°.
- The distance between projections of the STK and BGO tracks on first layer of BGO must be less than 60 mm (for both XZ and YZ view).
- The distance between projections of BGO and STK tracks on the first layer of the STK must be less than 200 mm (for both XZ and YZ views).
- STK track-ID match. The selection Requires that STK and BGO tracks are matched at both the XZ and YZ view level. Specially, for each event, a 3-D track is firstly reconstructed by the Kalman filter algorithm, then the 3-D track is projected into XZ and YZ views thus, turning into two 2-D tracks. The same procedure is performed with BGO track. The track-matching between the STK and BGO are completed based on the 2-D tracks. In this case, a track-ID match is needed, which works as follows: a track-ID is assigned to each 3-D track, the corresponding 2-D tracks share the same track-ID with their corresponding 3-D tracks. After matching STK and BGO tracks, the survival 2-D tracks must have

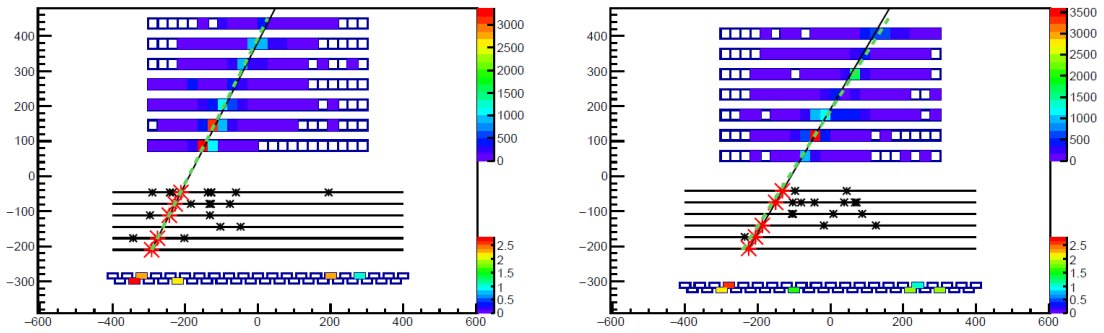

FIGURE 4.7: Example of a simulated proton event that passes all the track selections, seen from both XZ (left) and YZ (right) views. The STK track is represented by black line and the BGO track is in green dash line. The event releases 40.518 GeV energy inside the BGO calorimeter.

the same track-ID, thus indicating they come from the same 3-D track. If more than one 3-D track is found to meet the track-ID requirement, the closest STK track with BGO track will be selected.

Following the STK-BGO match selection, only one track (the best track) will be left for each event, the best track is then asked to match with the position of the BGO bar with maximum energy deposition, and then fulfills the STK-PSD match as following:

- The distance between projection of the best track and the position of BGO bar with maximum energy deposition must be less than 30 mm on first layer of the BGO;
- The projection of the best track on first layer of the PSD has to be within [-400mm, 400mm] for both XZ and YZ view in DAMPE coordinate system to ensure the track passing through the PSD;
- The PSD bars traversed by the track must have energy depositions higher than 0.5 MeV in order to make possible the reconstruction of particle charge.

An example of a well-reconstructed track of a MC proton event is presented in Fig. 4.7, where both STK track (black line) and BGO track (green dash line) are shown.

4.4.3 Trigger selection and shower development cuts

DAMPE provides four types of trigger, and the incident particles are required to activate the High Energy Trigger (HET). The HET distinguishes events with energy depositions in the first four BGO layers exceeding a threshold of 10 MIPs in each hit BGO bar.

Besides, the HET is the only type of trigger that will not suppress the trigger rate (see chapter two).

To remove events entering from the bottom of the BGO detector, a cut based on the shower development of events is used:

$$E_{BGO_{L0}} + E_{BGO_{L1}} < E_{BGO_{L2}} + E_{BGO_{L3}}, \tag{4.2}$$

$E_{BGO_{L0,1,2,3}}$ are the energy depositions from first to fourth layer of the BGO respectively.

4.4.4 Removal of electron background

The background of electrons (also positrons) must be removed. Since electrons have the same behaviour as protons in the PSD, the BGO is used to to discriminate these two particles by using their different shower shape. Electrons initiate an electromagnetic shower, meanwhile a hadronic shower will be induced by H or He events. Compared with an electromagnetic shower, a hadronic shower has a larger spread on both horizontal and vertical axes as shown in Fig. 4.8. This topological difference of two types of shower in the BGO calorimeter forms the basis for the identification. In [4], a method is presented to discriminate electrons from protons by utilizing the measurements performed by the BGO. The same method is used in this analysis for removing electrons from H + He samples. This method is based on a pattern recognition by using the variable ζ which combines lateral and vertical shower shapes:

$$\zeta = \mathcal{F}_{last} \cdot \frac{(RMS_{tot})^4}{8 \times 10^6} \tag{4.3}$$

where $\mathcal{F}_{last}$ is the ratio of deposited energy in the last BGO layer (E_{last}) over total deposited energy (E_{BGO}):

$$\mathcal{F}_{last} = \frac{E_{last}}{E_{BGO}}. \tag{4.4}$$

RMS_{tot} is defined as the sum of the energy-weighted shower dispersion for each BGO layer:

$$RMS_{tot} = \sum_{i=0}^{13} RMS_i, \tag{4.5}$$

with:

$$RMS_i = \sum_{j=0}^{21} (x_{j,i} - x_{c,i})^2 \cdot E_{j,i}, \tag{4.6}$$

where $x_{j,i}$ is the coordinate of j-th bar in i-th layer of the BGO. Meanwhile $E_{j,i}$ is deposited energy in the same bar, $x_{c,i}$ is the shower center coordinate of i-th layer.

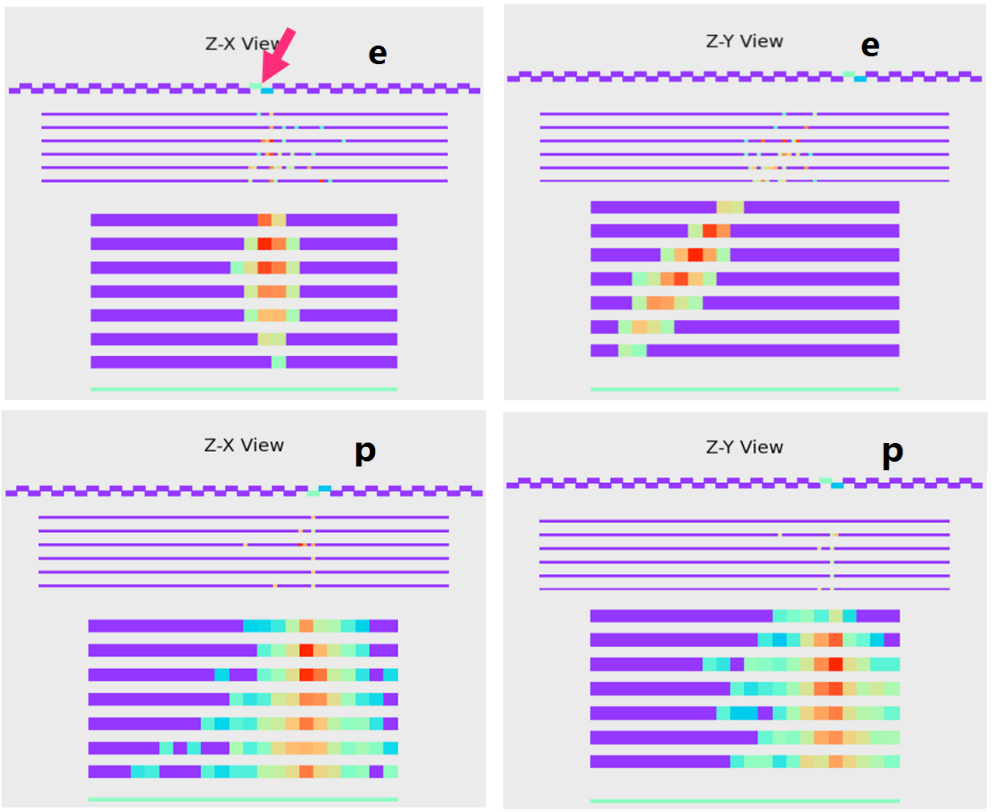

FIGURE 4.8: Examples of showers induced by a proton and electron in DAMPE. The upper two plots are the electromagnetic shower triggered by an electron event viewed from both the XZ view (upper, left) and the YZ view (upper, right). The lower two plots are the hadronic shower triggered by a proton event viewed from XZ view (lower, left) and the YZ view (lower, right). For both latitude and vertical directions, hadronic shower has a larger spread.

$\mathrm{RMS_{tot}}$ describes the size of a shower. In order to have an intuitive impression on the effect of this method, $\mathcal{F}_{\mathrm{last}}$ is shown as a function of $\mathrm{RMS_{tot}}$ in Fig. 4.9. The proton and electron events can be well separated with this method.

A template fit is implemented for ζ distributions of both electron and H + He samples so that the electron contamination can be estimated. In Fig.4.10, the ζ distributions for different BGO energy bins are presented. The estimation of electron contamination in H + He samples as a function of energy is shown in Fig. 4.11. The result shows that the contamination is less than 0.1%. Therefore, we can neglect the influence from electrons and positrons in this analysis.

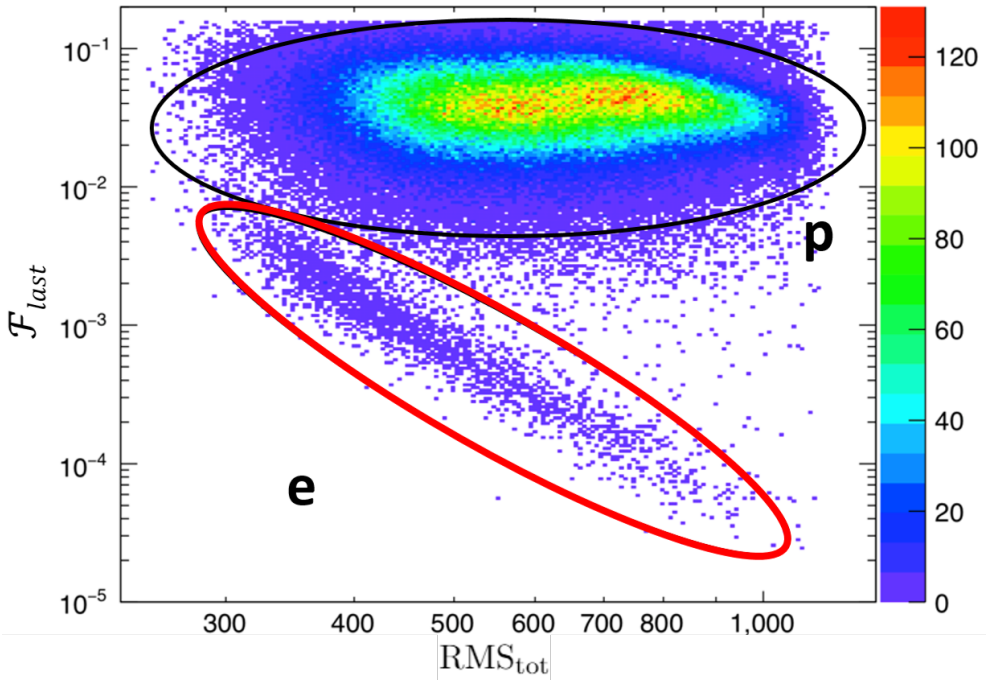

FIGURE 4.9: $\mathcal{F}_{last}$ values regarding $\mathrm{RMS_{tot}}$. The events inside the red line region are the electrons, the events inside the black line region are the protons. The plot comes from [4].

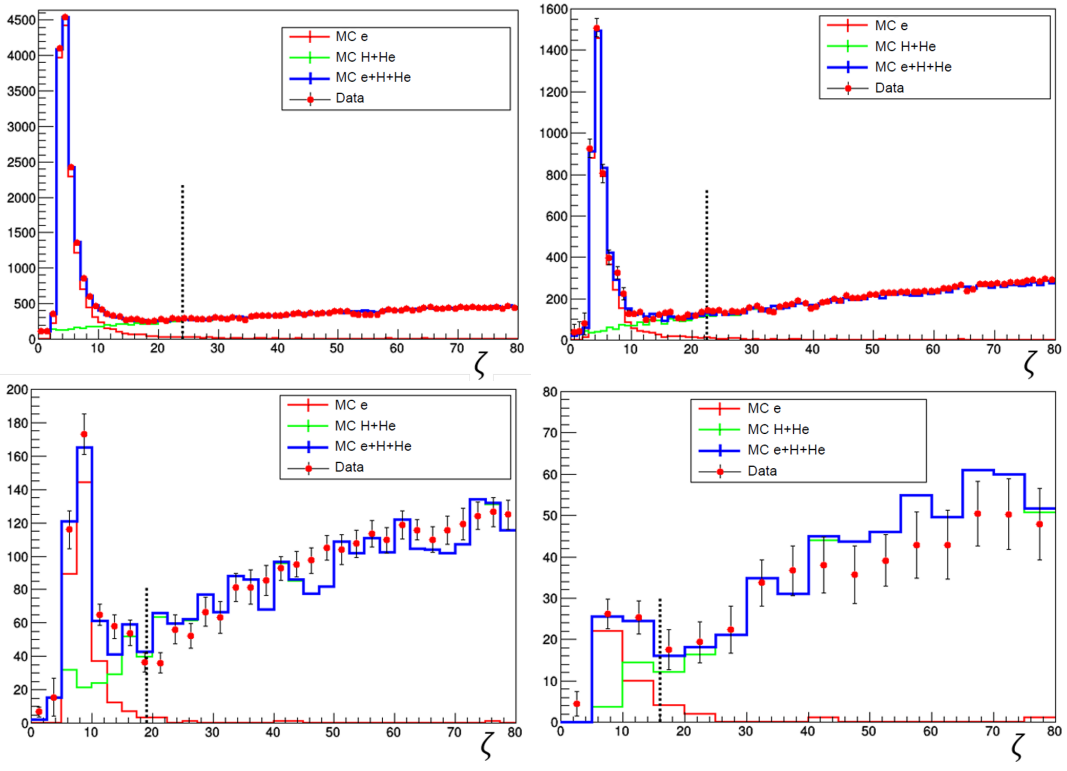

FIGURE 4.10: The ζ distributions of MC electron and H + He samples and the data regarding different BGO energy bins (upper left:133 GeV - 177 GeV, upper right: 237 GeV - 316 GeV, down left: 750 GeV - 1000 GeV, down right: 2371 GeV - 3162 GeV). The template fits are performed for each of the distribution. The black dash lines indicate the thresholds for separating the electrons (left of the lines) from H + He nuclei (right of the lines).

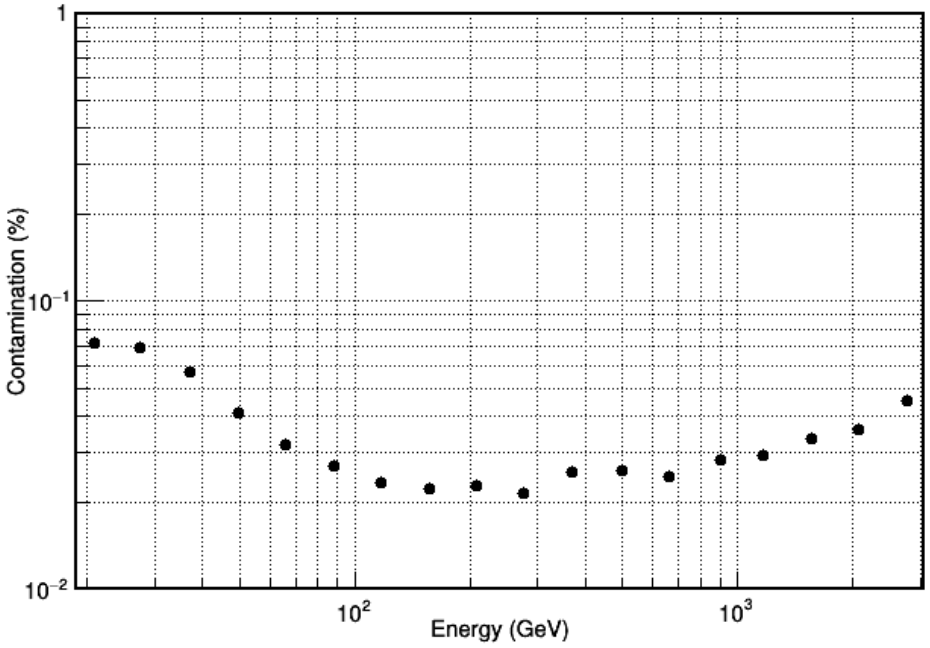

FIGURE 4.11: Electron contamination to H + He samples as the function of the BGO energy.

4.4.5 Charge selection with the PSD

Global measurement of the PSD

The charge of an impinging particle is mainly measured by the plastic scintillator detector of DAMPE. The PSD is composed of two layers of scintillator bar, and each layer is able to provide an independent charge measurement. The effect of light attenuation is firstly corrected [111], then the effect of the incident angle is corrected using track information. In Fig. 4.12, a diagram for a particle passing through one layer of the PSD is presented. In this case, Bar-1 contains a longer particle path than bar-2, thus having a larger signal output. In our analysis, instead of using the measurement only from bar-1, the bar-2 measurement is also used and combined with bar-1 as:

$$\Delta E_{track} = (E_1 + E_2) \times \frac{10\ mm}{L_1 + L_2}\ , \tag{4.7}$$

ΔE_{track} represents the energy measurement from a PSD layer. E_1 and E_2 are the energy deposition in bar-1 and bar-2 respectively. L_1 and L_2 are the path length of the trajectory in bar-1 and bar-2, 10 mm represents thickness of a PSD bar. By using the equation 4.7, not only the multiple bars measurements are combined, the effect of the incidence angle is also corrected. The charge selection for H + He candidates is based on ΔE_{track} since ΔE_{track} is only related to the charge of an entering particle. Both PSD X-layer and Y-layer can give a ΔE_{track} measurement independently, therefore a global PSD charge

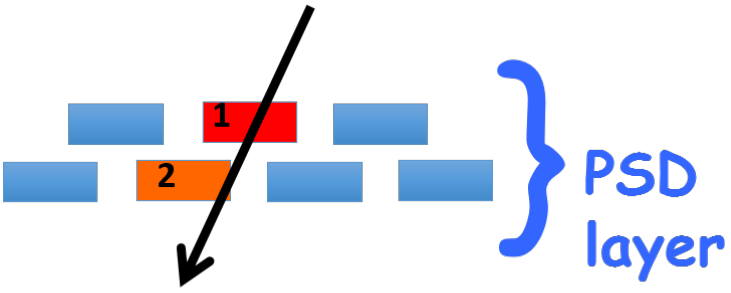

FIGURE 4.12: The diagram for a particle passing through two bars in one layer of the PSD. The black arrowhead represents the trajectory. In this case, the particle deposits more energy in bar-1 than bar-2, since its path length is longer in bar-1.

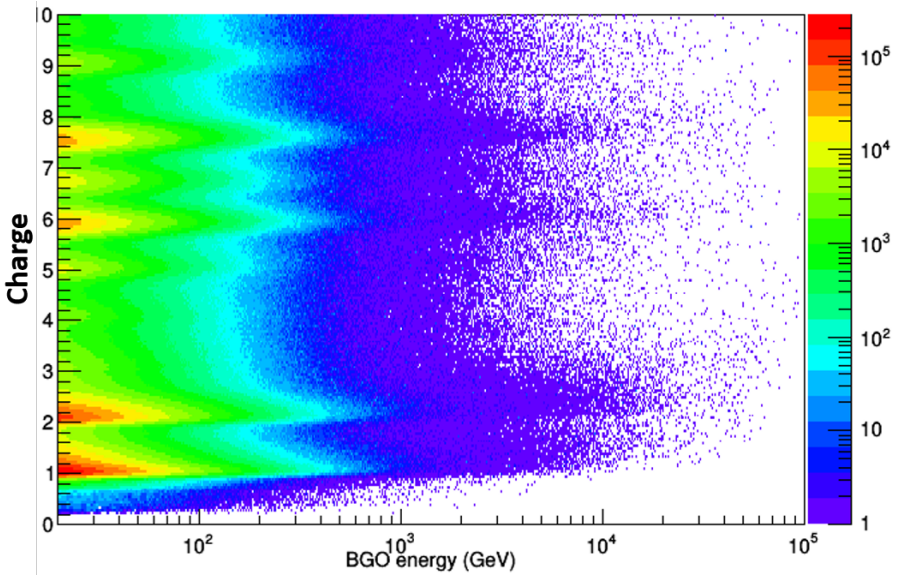

FIGURE 4.13: scatter diagram with variables $E_{PSD_{Glo}}$ normalized by the proton charge V.S. BGO energy.

measurement $E_{PSD_{Glo}}$, defined as $(\Delta E_{trackX} + \Delta E_{trackY})/2$, will be used as the reference to select H + He candidates.

In Fig. 4.13, the scatter plot with variables $E_{PSD_{Glo}}$ (normalized by the the proton charge) and BGO energy is presented, the electron events have been removed. Different elements can be recognized in different clusters.

In order to precisely select the charge, an extra selections are performed based on the ΔE_{trackY}:

- The difference between ΔE_{trackX} and ΔE_{trackY} should be less than 5 MeV.

This selection is to set a constraint on the difference of energy measured by two PSD layers. Since a large difference is possibly due to the back-scattered particles, which could results in a poor charge measurement.

PSD MC correction and selection

In general, when a high energy particle traverses a PSD bar, only a MIP signal is extracted. However, the energy deposition per unit of the length increases slightly with primary energy of a particle according to Bethe-Bloch equation [112]. Due to the large energy range measured by DAMPE (from 5 GeV/n to 100 TeV/n), the change of $E_{PSD_{Glo}}$ can not be ignored. Then, the selection range for H + He candidates should also change with the primary energy of a particle. The distributions of $E_{PSD_{Glo}}$ regarding different BGO energy intervals are studied for both MC and data. The distributions of $E_{PSD_{Glo}}$ for several BGO energy bins are fitted with Landau convoluted with Gauss function (Lan-Gaus function) as presented in Fig. 4.14.

The fit parameters of a Lan-Gaus function include the Most Probable Value (MPV), the sigmas of Gauss (σ_{Gaus}) and Landau (σ_{Lan}) functions. The square root of the quadratic sum of σ_{Gaus} and σ_{Lan} is taken as the total sigma of the Lan-Gaus function (referred as σ_{Tot}). The MPV as a function of BGO energy for H and He are shown in Fig. 4.15 where the data points are fitted with a fourth order of polynomial function respectively. The σ_{Tot} as a function of the BGO energy are shown in Fig. 4.16. The fit functions of σ_{Tot} and MPV are used for deciding the PSD selection ranges.

A non-negligible disagreement between MC and data can be found in Fig. 4.15 and Fig. 4.16. The explanation for this disagreement could be the MC overestimating the fraction of back-scattered particles, more discussion on this issue can be found in section 4.8.1. Since the MC will be used to compute the acceptance, a large charge measurement disagreement between MC and data could lead to an inappropriate Charge selection range and result in an inaccurate spectrum. Therefore, a correction on PSD charge measurement of the MC should be performed.

The correction is fulfilled event-by-event with equation 4.8:

$$E_{PSD_{Glo\_Cor}} = (E_{PSD_{Glo}} - f_{MCMPV}(E_{BGO})) \cdot \frac{f_{DataSigma}(E_{BGO})}{f_{MCSigma}(E_{BGO})} + f_{DataMPV}(E_{BGO}), \quad (4.8)$$

where the $E_{PSD_{Glo\_Cor}}$ represents the corrected PSD energy, meanwhile $E_{PSD_{Glo}}$ is the PSD energy before the correction. $f_{MCMPV}(E_{BGO})$ and $f_{DataMPV}(E_{BGO})$ are the 4th order fitting functions of the MC MPV and data MPV (as shown in Fig. 4.15). E_{BGO} is the BGO energy for each event. $f_{MCSigma}(E_{BGO})$ and $f_{DataSigma}(E_{BGO})$ are the fourth order fitting function of the σ_{Tot} for MC and data respectively (as shown in Fig. 4.16). After the correction the distributions of $E_{PSD_{Glo\_Cor}}$ (fitted with Lan-Gaus function) are presented in Fig. 4.17.

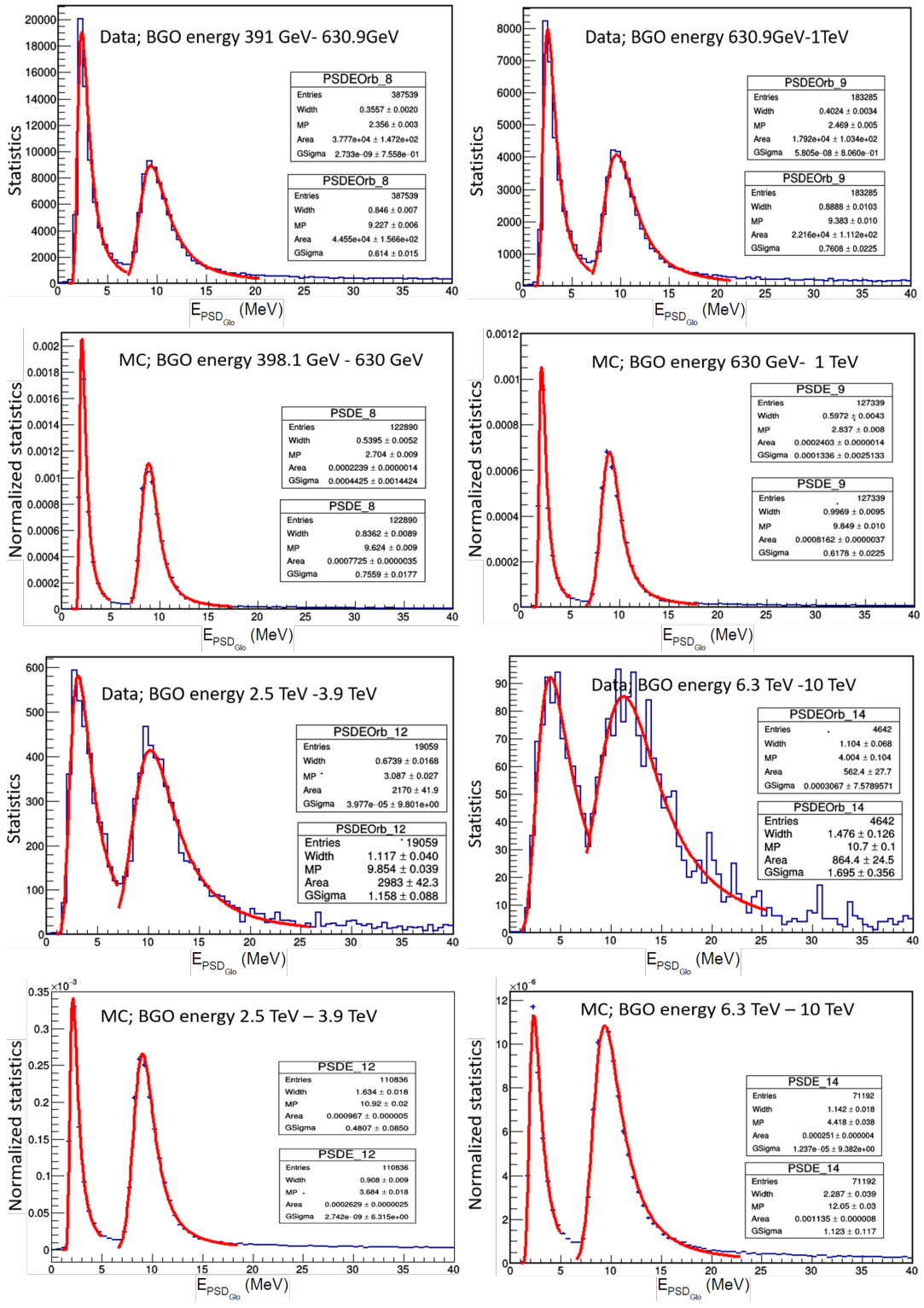

FIGURE 4.14: Distribution of $E_{PSD_{Glo}}$ for data and MC samples. The proton and helium peak can be easily recognized. The red lines mark the Lan-Gaus function fitting results.

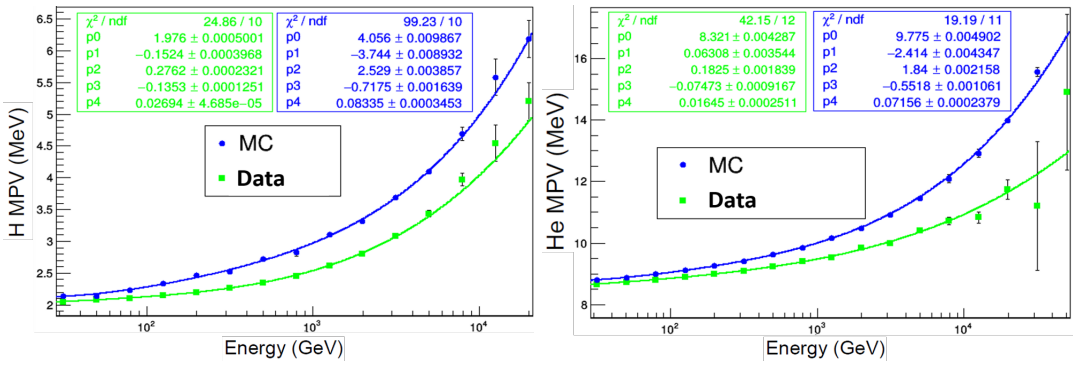

FIGURE 4.15: The MPV of Lan-Gaus fit as a function of BGO energy for H (left) and He (right). Both MC and the data are fitted with a 4-th order polynomial function. The MC is with color of blue, the data is in green.

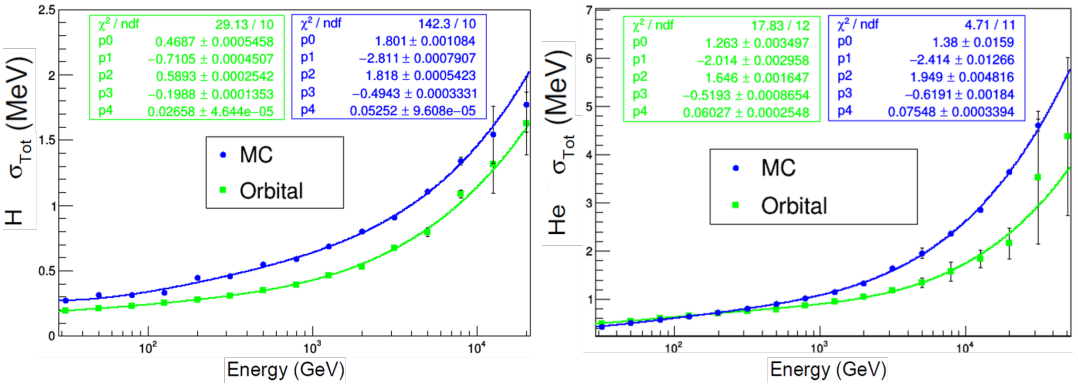

FIGURE 4.16: The σ_{Tot} of Lan-Gaus fit as a function of BGO energy for H (left) and He (right). Both MC and the data are fitted with a 4th order of the polynomial function.

The fitting results of the corrected PSD measurement as a function of BGO energy are presented in Fig. 4.18. Compared with Fig. 4.15 and Fig. 4.16, the MC and data have a better agreement after the correction.

Then the charge selection for MC samples is based on the $\mathrm{E_{PSD_{Glo\_Cor}}}$, and the fit parameters shown in Fig. 4.18. the PSD selection range for H + He candidates is decided as:

$$\mathrm{f_{H_{MPV}}(E_{BGO}) - 3 \cdot f_{H_{sigma}}(E_{BGO})} \;<\; \mathrm{E_{PSD_{Glo\_Cor}}} \;<\; \mathrm{f_{He_{MPV}}(E_{BGO}) + 6 \cdot f_{He_{sigma}}(E_{BGO})}, \quad (4.9)$$

where $\mathrm{f_{H_{MPV}}}$ represents the fitting function of the MPV of H candidates (as shown in the upper left of Fig. 4.18). The same for $\mathrm{f_{H_{sigma}}}$, $\mathrm{f_{He_{MPV}}}$ and $\mathrm{f_{He_{sigma}}}$ which represent the σ_{Tot} of H, MPV and σ_{Tot} of He respectively.

An example of the charge selection range for H and He candidates is shown in Fig. 4.19. Since mutual contamination between H and He nuclei is not an issue in this analysis, the charge selection range is larger comparing with CR proton spectrum analysis, which guarantees a larger statistics. The PSD selection range regarding the BGO energy for the orbit data of DAMPE is shown in Fig. 4.20. The shadow area between the two

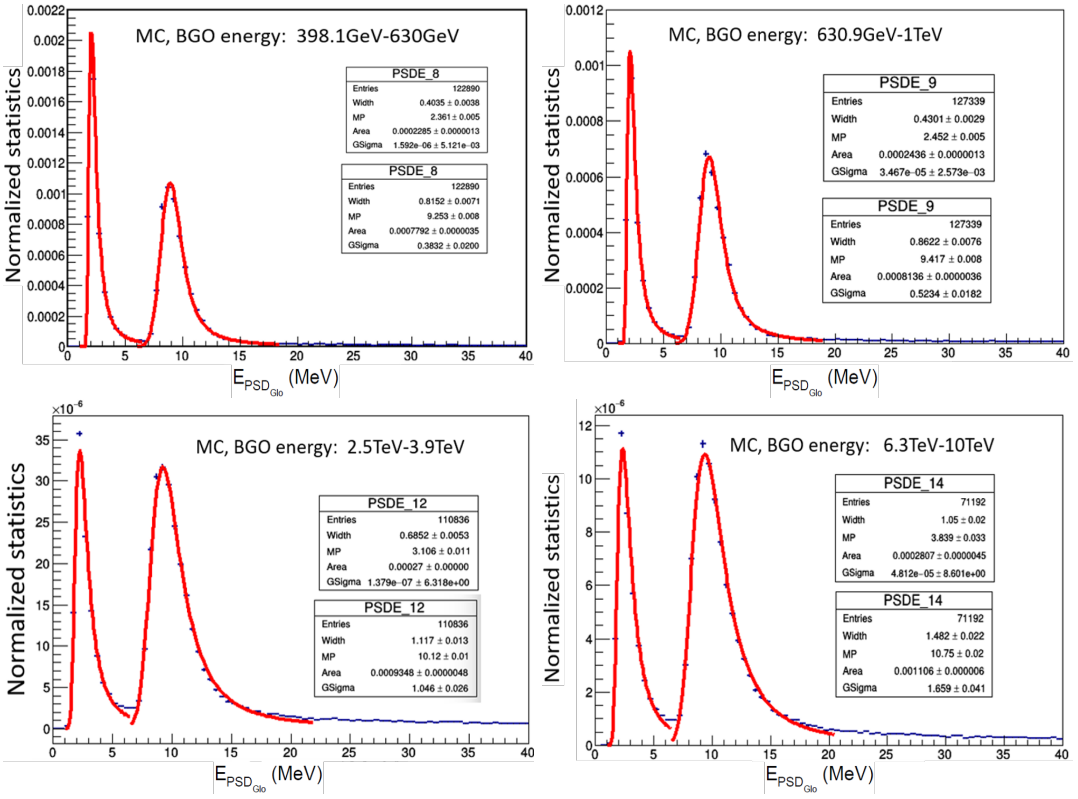

FIGURE 4.17: Distribution of MC $E_{PSD_{Glo\_Cor}}$ regarding different BGO energy bins. The red lines mark the Lan-Gaus fit.

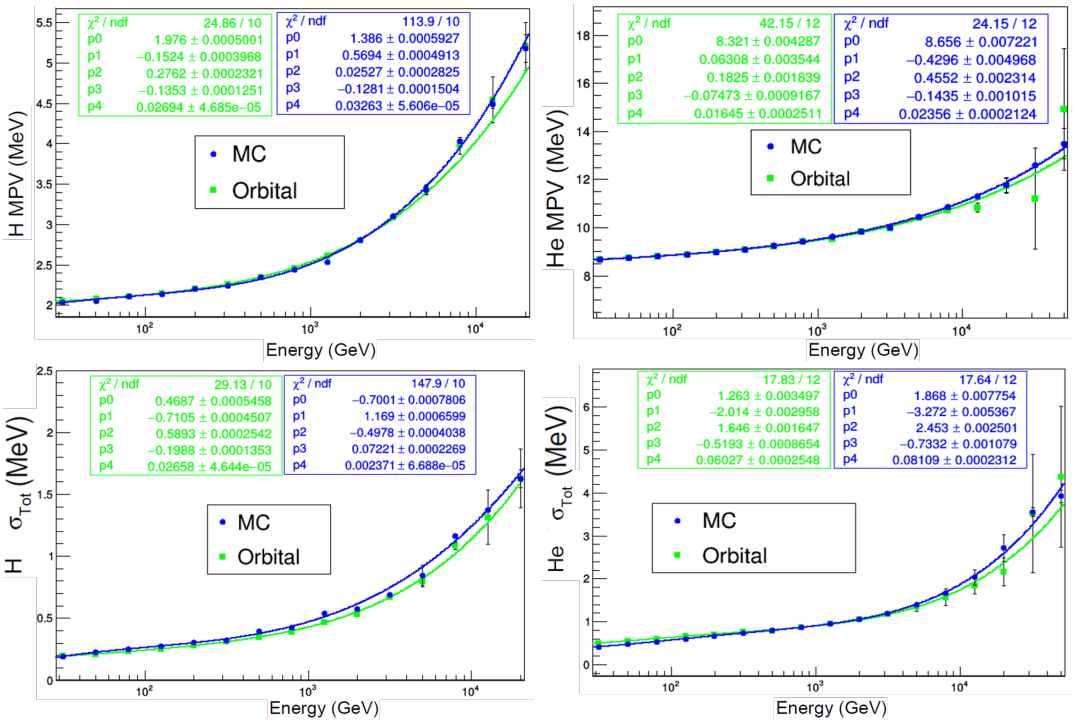

FIGURE 4.18: After the correction, the measurement of the PSD fit results as a function of BGO energy for proton MPV (upper, left), helium MPV (upper, right), proton σ_{Tot} (lower,left) and helium σ_{Tot} (lower,right).

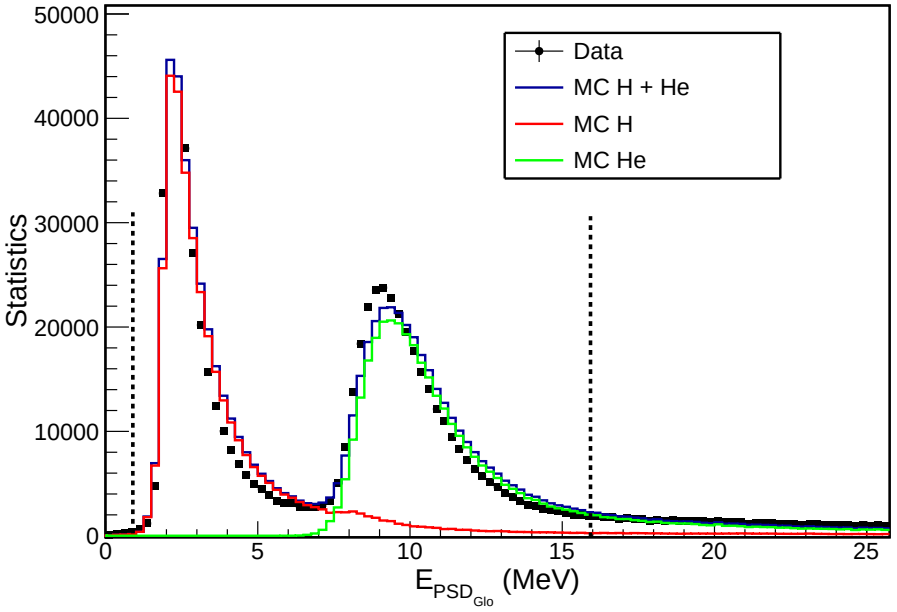

FIGURE 4.19: the PSD selection range for H and He candidates for both MC and real data in terms of BGO energy interval between 251 GeV and 398 GeV. The dash lines mark the selection range for H + He candidates.

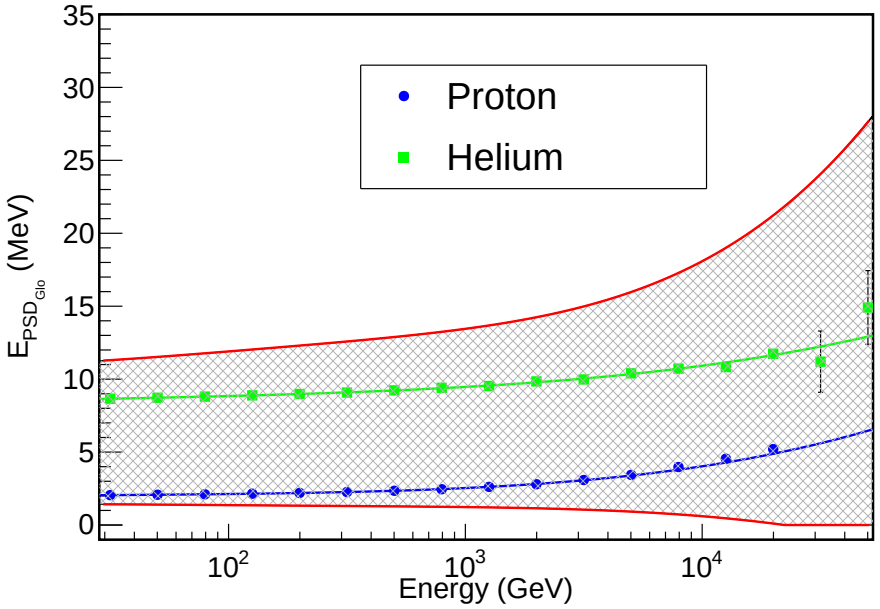

FIGURE 4.20: Charge selection range (shadow region) for the orbit data as a function of BGO energy.

red lines represents the PSD selection region for the H + He candidates. The selection range is derived from equation 4.9.

4.5 The selection Efficiency

The MC samples are used to compute the efficiency of the selection cuts as:

$$\epsilon = \frac{N_{Survival}}{N_{Total}} \ , \tag{4.10}$$

where $N_{Survival}$ is the number of the MC H + He particles that survive the selection cuts, and N_{Total} is the number of the generated MC H + He particles. The efficiency will be used to calculate the detector acceptance, which is then used to compute the flux (as shown in equation 4.1). The efficiency is not a constant regarding BGO energy, thus the efficiency as a function of BGO energy need to be studied. Moreover, in order to verify the efficiency derived from MC, we also compute the efficiency of several selections from the data and make a comparison between the MC and data. The results of the comparison will be used for calculating the systematic uncertainties. When computing the efficiency from the data, the value of N_{Total} in equation 4.10 can not be determined. An alternative way is to use a selection based on one sub-detector to distinguish a certain number of events as N_{Total}, then based on these events we perform the selection for which the efficiency will be checked. Then the number of the survival events after performing the selection cut is taken as $N_{Survival}$. By using this method, the efficiencies of three key groups of selection are computed: The high energy trigger, the charge reconstruction and the STK track selection.

4.5.1 High Energy Trigger (HET)

The HET is chosen as the standard trigger in selecting high energy H + He candidates. In order to compute the efficiency of the HET selection, the unbiased trigger is used for selecting a group of samples to compute N_{Total}, the HET efficiency in this case can be computed as:

$$\epsilon_{HET} = \frac{N_{(HET|Unb)}}{N_{(Unb)}} \tag{4.11}$$

where $N_{(Unb)}$ is the number of events passing all the aforementioned cuts in section 4.4 except the HET, instead, the unbiased trigger is required. $N_{(HET|Unb)}$ is the number of events with HET also activated among $N_{(Unb)}$. The HET efficiencies calculated in this way for both MC and data are shown in Fig. 4.21. The ratio between the data and MC is also plotted, where a difference within 6% can be found up to 10 TeV of BGO energy.

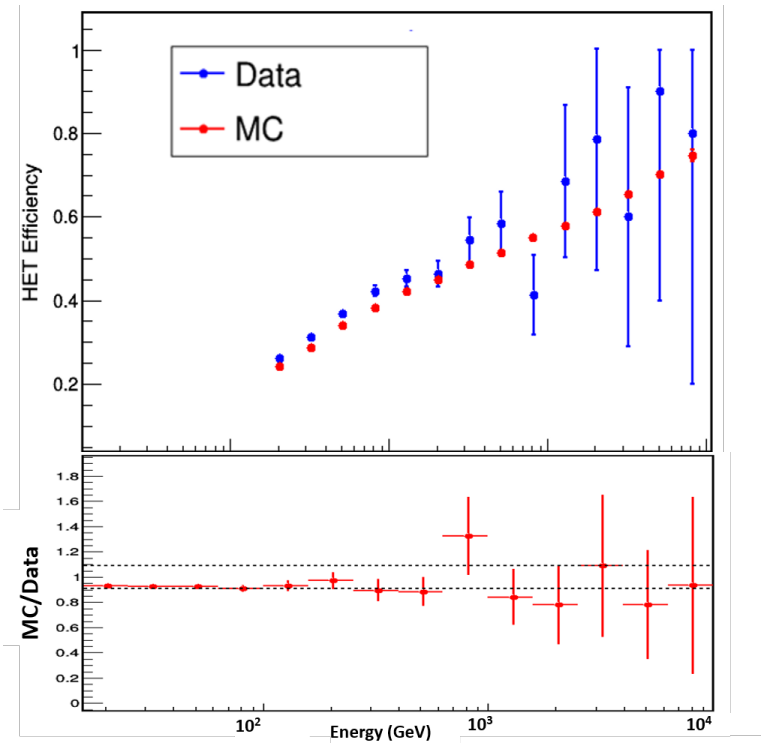

FIGURE 4.21: The high energy trigger efficiencies for MC and data (up), and the ratio of them (down). The dash lines marks boundary of the difference (within 6%).

4.5.2 Charge reconstruction

The charge reconstruction efficiency reflects the capacity of the PSD in distinguishing the charge of an entering particle. The efficiencies of both layers of the PSD are estimated by using the STK charge measurements. For instance, when the efficiency of the PSD X-layer is estimated, the PSD Y-layer and the STK (first plane) are used to select a group of H + He candidates. Then the charge reconstruction efficiency of the PSD X-layer can be computed as:

$$\epsilon_{\mathrm{PSD_X}} = \frac{\mathrm{N}_{(\mathrm{PSD_X}|\mathrm{PSD_Y}|\mathrm{STK})}}{\mathrm{N}_{(\mathrm{PSD_Y}|\mathrm{STK})}} \tag{4.12}$$

where $\mathrm{N}_{(\mathrm{PSD_Y}|\mathrm{STK})}$ is the number of events that pass all the cuts described in section 4.4 except charge selection cut, instead, the charge selection is fulfilled by the PSD Y-layer and STK. $\mathrm{N}_{(\mathrm{PSD_X}|\mathrm{PSD_Y}|\mathrm{STK})}$ represents the number of events that survive the selection from PSD X-layer as well among $\mathrm{N}_{(\mathrm{PSD_Y}|\mathrm{STK})}$. It is important to decide selection ranges of the PSD X, Y layer and STK for H + He candidates respectively. For the STK, we select events having an ADC count less than 500 (measured by first STK plane) as H + He candidates. The plots of STK charge measurements regarding two BGO energy bins are shown in Fig. 4.22.

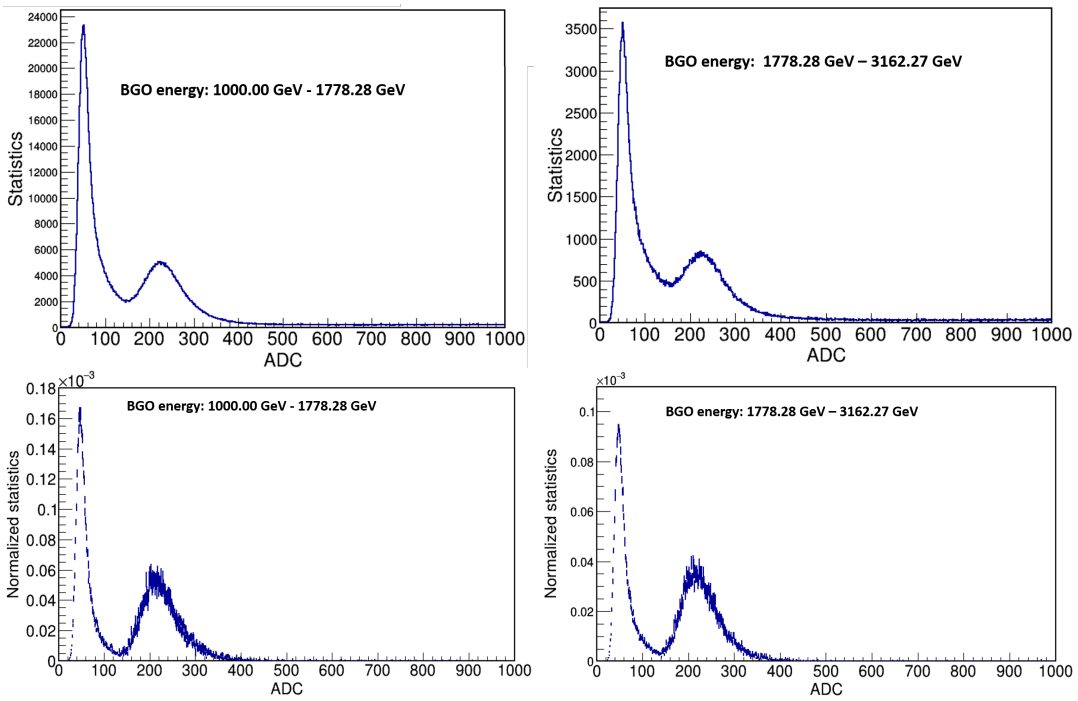

FIGURE 4.22: The distribution of STK charge measurement regarding two BGO energy bins. Both real data (upper two plots) and MC (lower two plots) are shown. The ADC here is taken as the average of the X and Y layer output of first STK plane. For both MC and data, the used candidates must survive all the selections described in section 4.4 except the charge selection.

The charge range for selecting H + He candidates with a single PSD layer is decided as described in section 4.4.5: the distributions of the PSD measurement regarding different BGO energy intervals are fitted to obtain the functions that describe the relation between deposited energy in the PSD and in the BGO for H and He nuclei (the function is similar to the plots shown in Fig. 4.18). The correction on PSD measurement is also performed for each layer. The distributions of the energy measurement from the PSD X-layer (referred as E_{PSD-X}) and their fitting results regarding two BGO energy intervals are presented in Fig. 4.23. Analogously, the distribution of the PSD Y-layer energy measurements (referred as E_{PSD-Y}) are shown in Fig. 4.24.

The MPV of PSD X and Y layer as a function of BGO energy is presented in Fig. 4.25. The data sets are fitted with a fourth order polynomial function, and the parameters will be used to decide the selection range for PSD X and Y layer separately.

A method analogous with Eq. 4.9 is used: an interval of $[MPV_H - 3\sigma_H,\ MPV_{He} + 6\sigma_{He}]$ is given to determine the selection range. By using of the fitting parameters in Fig. 4.25, both PSD selection range for X and Y layers can be decided. Combining the charge selection from STK, the efficiency of the PSD charge reconstruction can be derived. In Fig. 4.26 the efficiencies (MC and data) for both layers of the PSD together with the

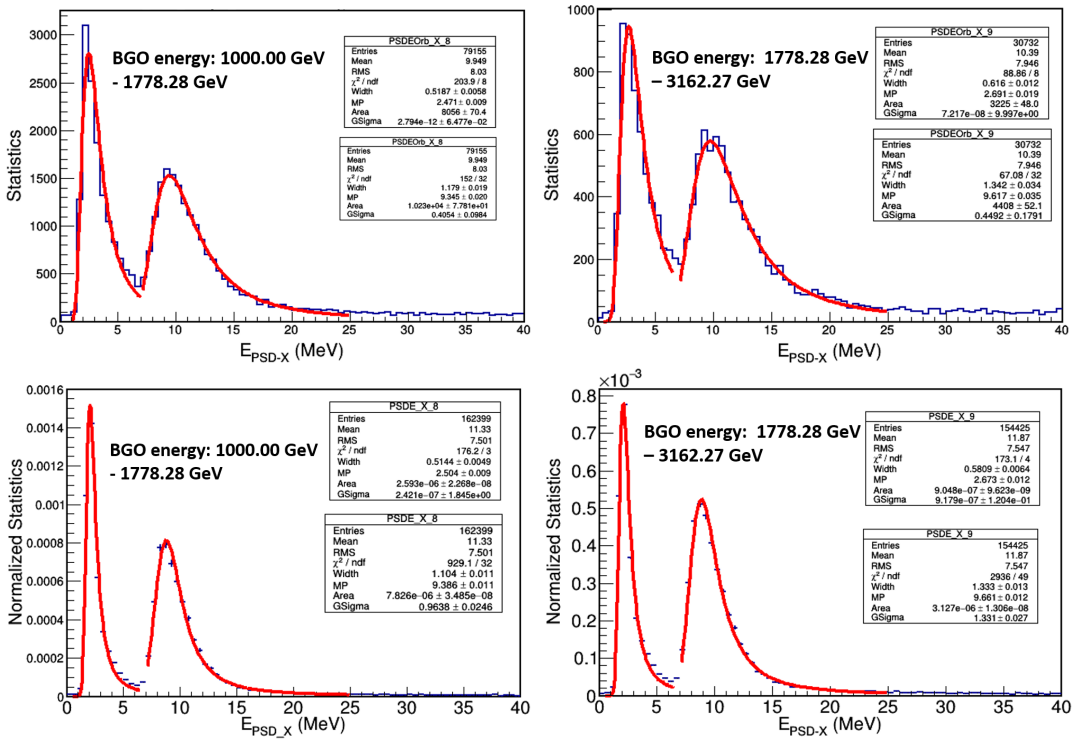

FIGURE 4.23: The distribution of E_{PSD-X} regarding two BGO energy bins. The upper two plots are from the real data, while the lower two plots are from the MC. The distributions are fitted with the Lan-Gaus function (red lines).

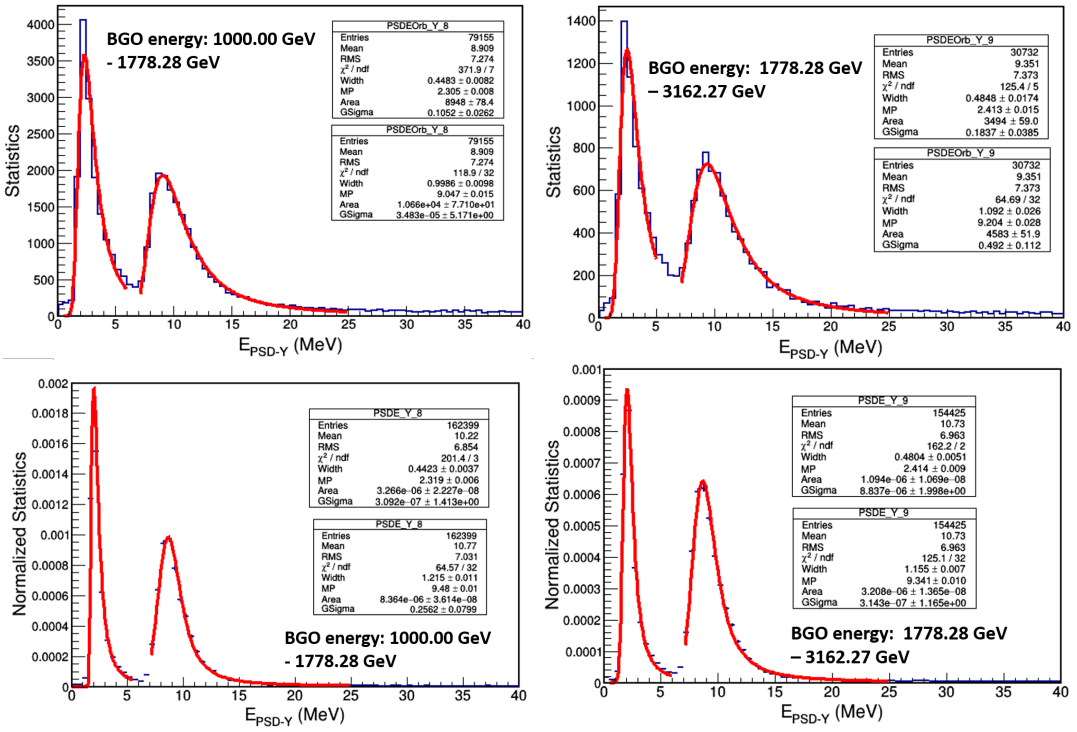

FIGURE 4.24: The distribution of E_{PSD-Y} regarding two BGO energy bins. The upper two plots are from the data, while the lower two plots are from the MC.

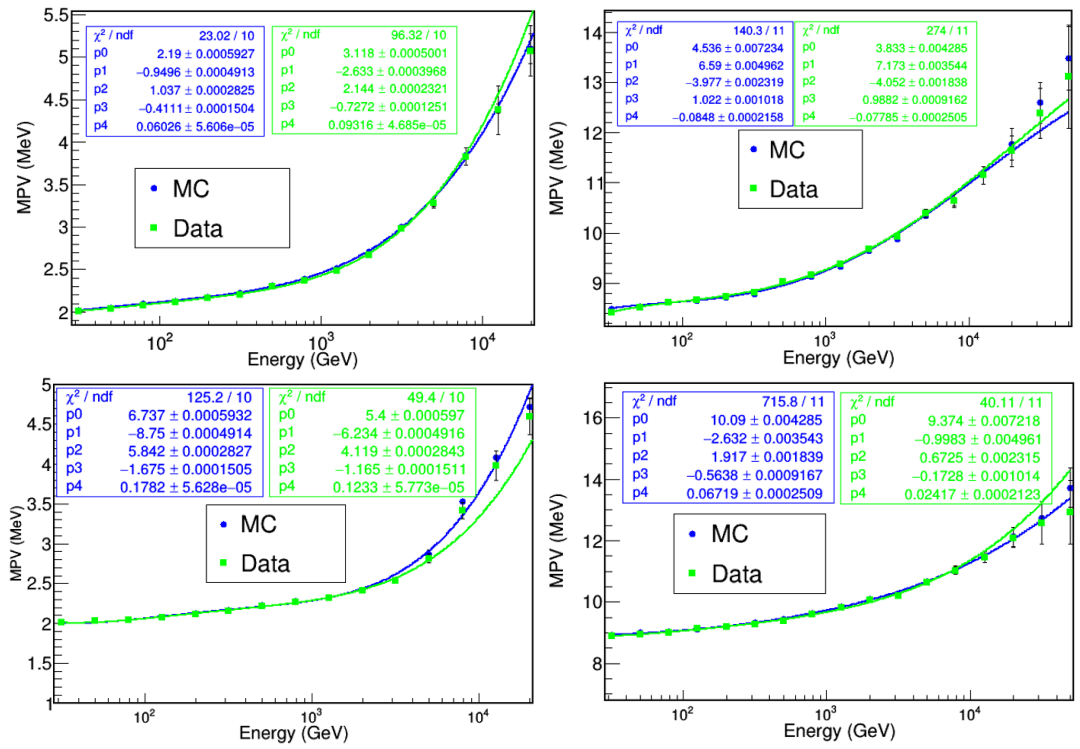

FIGURE 4.25: The measurement of the PSD fit results as a function of BGO energy for proton MPV (up, left), helium MPV (up, right) of the X layer; and proton MPV (down ,left), helium MPV (down, right) of the Y layer.

ratio between the MC and data are presented. The ratio shows that the difference is within 4%.

4.5.3 Track selection efficiency

In section 4.4.2, the selection cuts for the STK track are introduced. Equation 4.13 can be used to estimate the efficiency of this group of selections:

$$\epsilon_{\text{Track}} = \frac{N_{(\text{STK}|\text{BGO})}}{N_{(\text{BGO})}} , \tag{4.13}$$

where a track reconstructed by the BGO is needed. Since the selection efficiency related to STK is being estimated, only BGO and PSD measurements can be used to select H + He candidates. In equation 4.13, $N_{(\text{BGO})}$ is the number of selected H + He candidates, $N_{(\text{STK}|\text{BGO})}$ is that among $N_{(\text{BGO})}$, the number of the events that survive the STK track selections described in section 4.4.2.

Particles are required to survive the selections described in sections 4.4.1, 4.4.3 and 4.4.4 to select H + He candidates by using the BGO and PSD only. Moreover, the following selections are also needed to guarantee a better selection quality:

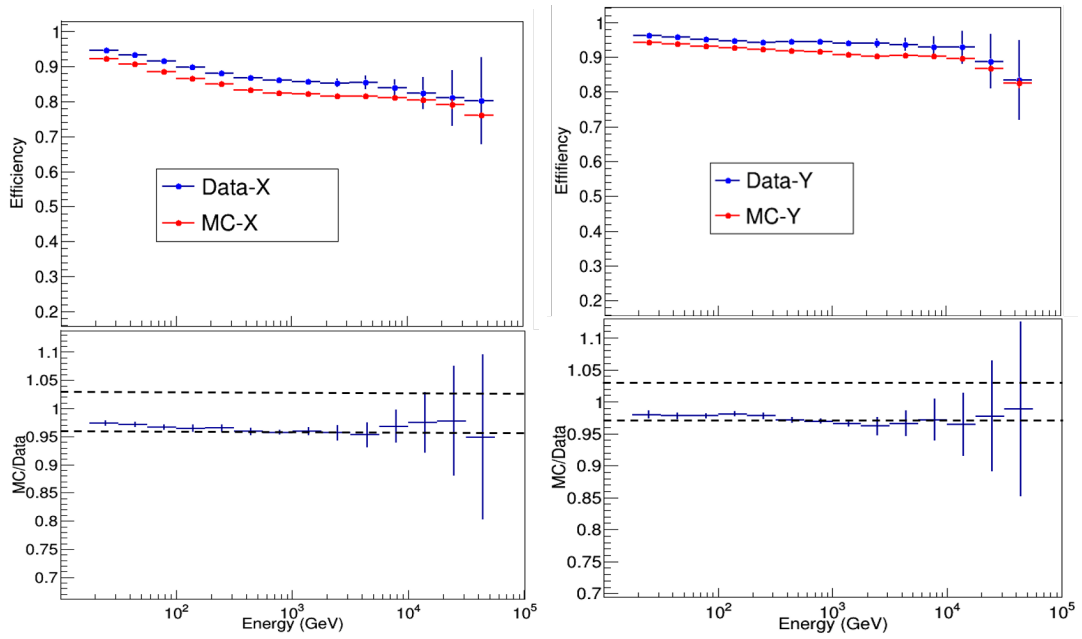

FIGURE 4.26: The charge reconstruction efficiency for PSD X layer (left) and Y layer (right) regarding to the BGO energy. The ratios between the data and MC efficiencies are shown at the bottom of each efficiency plot.

- The BGO track projection on the PSD should not be at the edge bars of the PSD.
- The distance between the projection of BGO track on the PSD and the PSD hit position, which demands the energy deposition is larger than 1 MeV, should be less than 40 mm. If there are more than one PSD hit within 40 mm, the event with largest PSD deposited energy will be chosen.
- In the first four layers of the BGO, the distance between BGO track projection and BGO bar with largest energy deposit should be less than 40 mm.
- The PSD selections (as described in section 4.4.5) are applied as the final selection.

After applying the selection cuts above, the number of survival events (the H + He nuclei selected by using the BGO and PSD only) is used as $N_{(BGO)}$ for equation 4.13. The $N_{(STK|BGO)}$ is derived by applying the selection cuts described in section 4.4.2 on these H + He candidates. Then, the efficiency can be computed with equation 4.13.

The STK track selection efficiencies regarding BGO energy is presented in Fig. 4.27 for both the data and MC. The ratio between the data and MC efficiencies is also plotted at the bottom of Fig. 4.27. The ratio plot shows that the difference is within 4%.

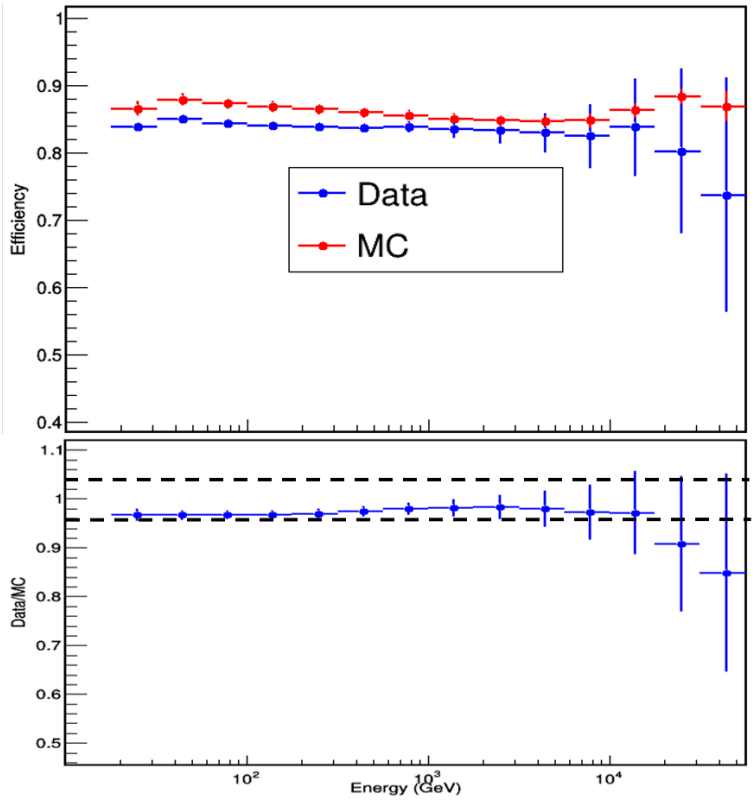

FIGURE 4.27: The STK track selection efficiency (upper), and the ratio between the data and the MC (lower) as functions of the BGO energy. The dash lines mark the interval [0.96, 1.04], which indicates that the difference between the data and MC efficiencies is within 4%.

4.6 Effective acceptance

In the MC simulation, the fluxes of the proton and helium are assumed to be isotropic. In this case, a half sphere with DAMPE located at its centre is used as the surface to generate the events (see appendix A). The effective acceptance of the DAMPE is defined as the geometrical acceptance multiplying the efficiencies of all the selection cuts:

$$A^{i}_{acc} = G_{gen} \cdot \frac{N(E^{i}_{T}, sel)}{N(E^{i}_{T})}, \tag{4.14}$$

where G_{gen} is geometrical acceptance used for generating the simulation data. $N(E^{i}_{T}$ and $N(E^{i}_{T}, sel)$ are the number of generated events and those that survive the selection cuts in i-th energy bin (primary energy: E_T). The sphere is with radius 1.38 m for proton and 1 m for helium. The geometrical acceptance equals $2\pi^2 \times r^2$, thus it is 37.59 sr m^2 for MC proton, 19.74 sr m^2 for MC helium. In H + He analysis, only an unique acceptance can be used by the algorithm for producing spectrum, therefore a correction is necessary in equation 4.14 to have an exclusive acceptance. G_{gen} of the MC proton is used as the benchmark, so G_{gen} of the MC helium is changed from 19.74 srm^2

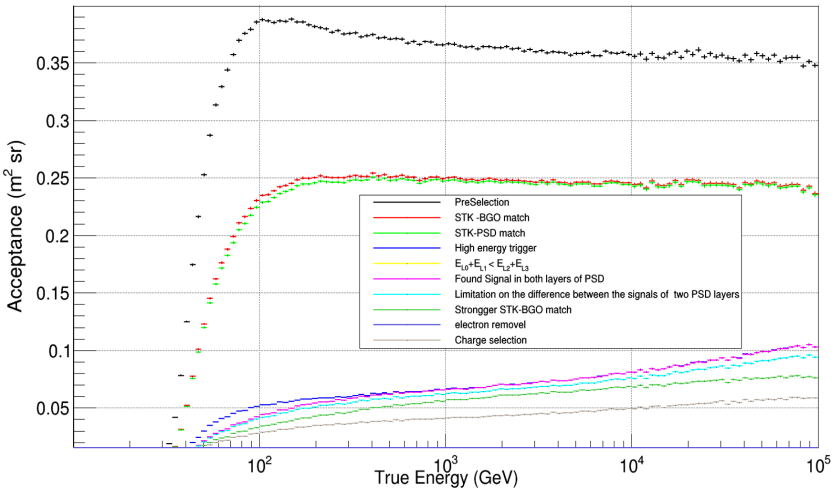

FIGURE 4.28: The acceptances for each set of selection cuts.

to 37.59 srm^2. According to Eq. 4.14, in order to ensure the correctness of A^i_{acc}, if G_{gen} is reassigned, the $N(E^i_T, sel)/N(E^i_T)$ must be corrected to compensate the change of G_{gen}. In this case, the compensation can be done by multiplying a factor equals 19.74/37.59 to the efficiency part. The reliability of this correction method will be discussed in the appendix A. The acceptance for each cut regarding the primary energy of MC H + He particles is shown in Fig. 4.28. After all the selections, the effective acceptance is around 0.05 m^2 sr at 10^4 GeV.

4.7 Energy reconstruction for H + He nuclei

Since the thickness of the BGO calorimeter is only ~ 1.6 interaction length, the deposited energies for H and He nuclei are only 35%-40% of their primary energies. In chapter three, we have discussed three methods to unfold the detector response and reconstruct the primary energies of hadronic particles. Among them, the method based on the Bayes theorem has been proved to have a better performance for DAMPE. Hence, in this section the Bayes unfolding method will be used to reconstruct the primary energy of H + He candidates. The events are firstly selected through the cuts introduced in section 4.4, then the unfolding algorithm is applied.

In order to understand the behaviour of hadrons in the BGO, the ratio between deposited energies (E_{BGO}) and the primary energies (E_T) of MC H + He nuclei have been studied. In Fig. 4.29, we present the distribution of deposited-primary energy ratio in two energy bins. The distributions are fitted with an asymmetric Gauss function which can be written as:

$$f(x) = \begin{cases} Gaus(x, \mu_0, \sigma/\kappa) & x \leq \mu_0 \\ Gaus(x, \mu_0, \sigma \cdot \kappa) & x > \mu_0 \end{cases} \tag{4.15}$$

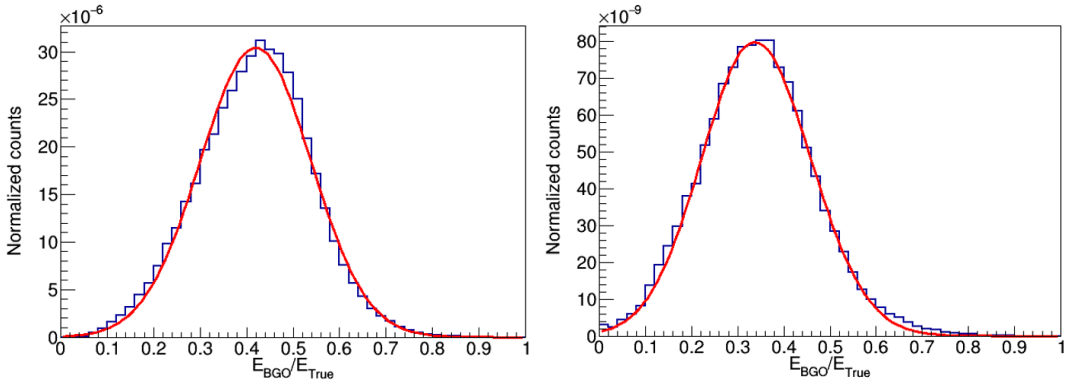

FIGURE 4.29: The distributions of the ratio between deposited energy and primary energy of H + He samples. The primary energies of the events are within interval of 251.1 GeV - 398.1 GeV (left), and 1000.0 GeV - 15848.9 GeV (right). The red lines mark the fitting functions.

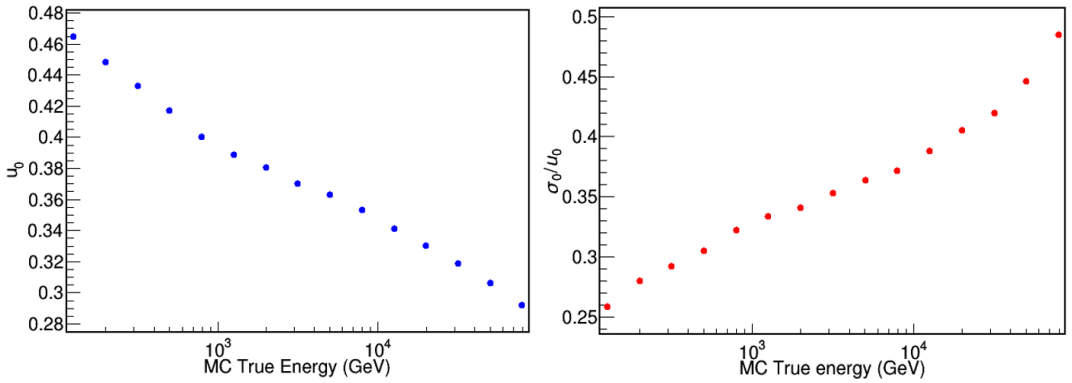

FIGURE 4.30: The μ_0 (left) and μ_0/σ (right) as a function of particle primary energy.

where μ_0 represents the most probable value of the fit function, κ is the correction factor for σ, it reflects the asymmetry of the Gauss functions. In order to see the dependency of μ_0 on primary energy, the values of μ_0 and μ_0/σ as functions of E_T are presented in Fig. 4.30. It shows that μ_0 decreases with increasing primary energy. The correlation between μ_0 and primary energy indicates that the energy leakage becomes larger as the primary energy of particles becomes higher. The trend of μ_0/σ regarding primary energy in the right panel of Fig. 4.30 indicates that the fluctuation of deposited energy becomes larger with increasing primary energy. These facts reaffirm the larger uncertainty in hadron energy measurement and challenges for energy reconstruction. The method based on the Bayes theorem has been verified (in chapter three) to be able to reconstruct the hadron energy effectively, therefore the Bayes method will be used to unfold the detector response and reconstruct the energy of H + He candidates.

4.7.1 The unfolding algorithm based on Bayes theorem

The procedures for implementing the Bayes method to unfold the detector response has been discussed in section 3.3.1. The energy reconstruction of hadron particles can be achieved by equation 4.16:

$$N(E_T^i) = \sum_{j=1}^{n} P(E_T^i|E_{BGO}^j) \cdot N(E_{BGO}^j), \quad j = 1, 2, ... \tag{4.16}$$

where $N(E_{BGO}^j)$ represents the event number in j-th bin of BGO energy (E_{BGO}), $P(E_T^i|E_{BGO}^j)$ is the probability matrix for migrating events among different energy bins to make the energy distribution approaching to the distribution before detector response. The distribution of the primary energy of the candidates is represented by $N(E_T^i)$. $P(E_T^i|E_{BGO}^j)$ can be derived from MC by using of the Bayes theorem as:

$$P(E_T^i|E_{BGO}^j) = \frac{P(E_{BGO}^j|E_T^i)P_0(E_T^i)}{\sum_{i=1}^{n} P(E_{BGO}^j|E_T^i)P_0(E_T^i)} \ . \tag{4.17}$$

$P_0(E_T^i)$ can be determined by referring to previous experiment measurements, and it will be updated as the unfolding procedures going on. $P(E_{BGO}^j|E_T^i)$ is derived from the MC (see more details in chapter three). In Fig. 4.31, the $P(E_{BGO}^j|E_T^i)$ used in this analysis is presented. As the unfolding procedures start, a spectrum with spectral index equals to -2.7 is used to determine the prior probability $P_0(E_T^i)$, the primary energy of H + He candidates can be reconstructed iteratively through the routine described in section 3.3.1. Moreover, a χ^2 is defined as equation 4.18 to see the influence of each iteration on energy distributions of the candidates.

$$\chi^2 = \sum_{j}^{n} \left(\frac{\hat{N}_{Af}^j - \hat{N}_{Bef}^j}{\sqrt{\hat{N}_{Bef}^j}}\right)^2 , \tag{4.18}$$

where $\hat{N}_{Bef}^j$ and $\hat{N}_{Af}^j$ are the number of event in j-th energy bin before and after an iteration. In Fig. 4.32, the value of χ^2 is plotted as a function of iteration. After 5 iterations, the χ^2 becomes very small, which indicates that the unfolding process no longer has an obvious impact on the candidate energy distribution.

4.7.2 The statistical error

As discussed in section 3.3.1, the calculation of the statistical error propagated by the Bayes method to the unfolded result is complicated. Therefore, a TOY-MC method is used to estimate the statistical error for the spectrum. The same method is also

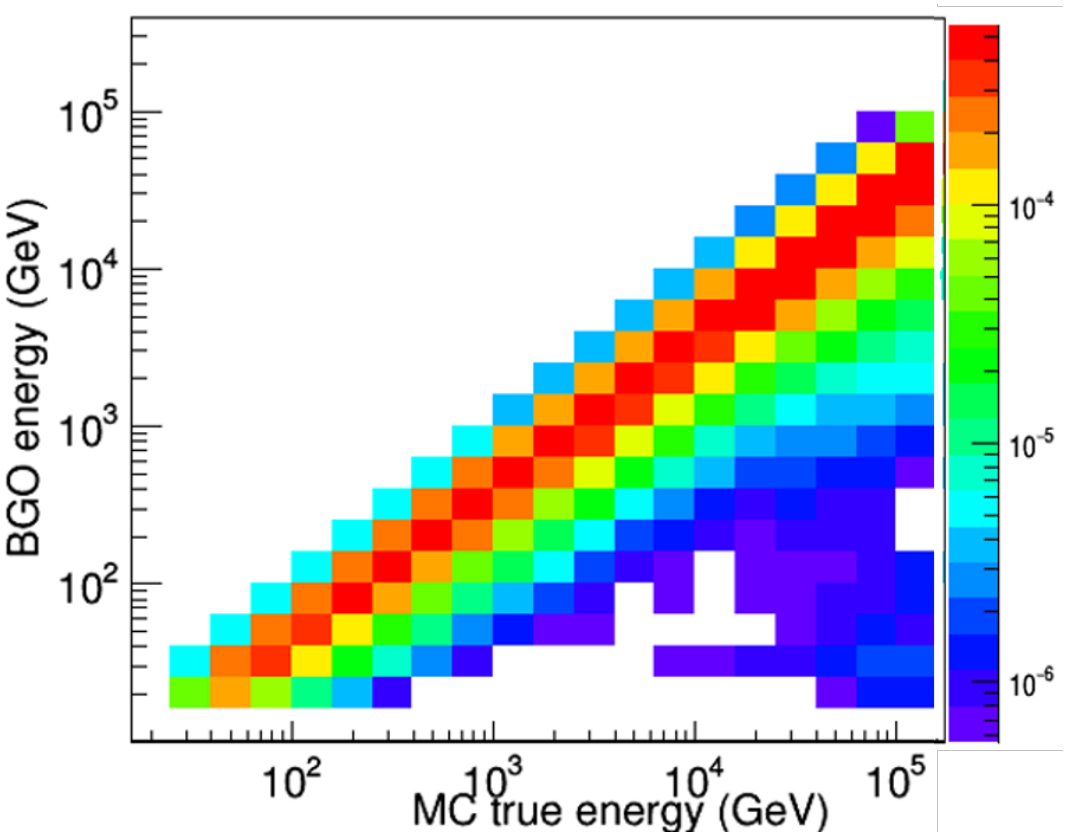

FIGURE 4.31: The matrix of $P(E^j_{BGO}|E^i_T)$ used in this analysis.

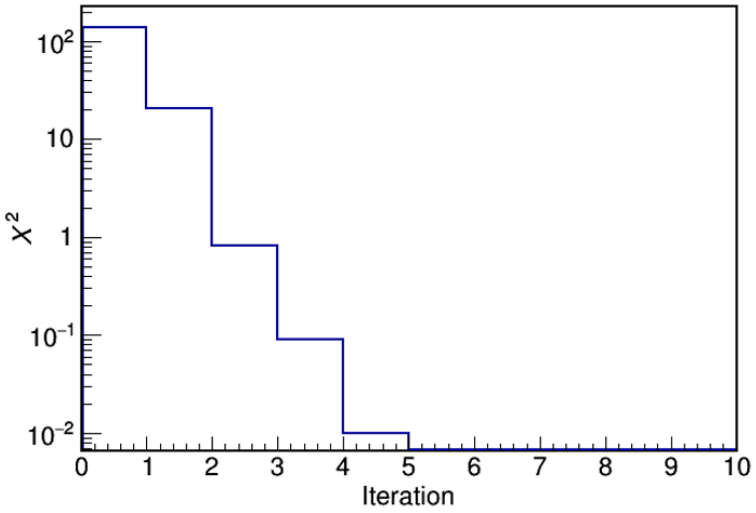

FIGURE 4.32: The χ^2 value as a function of the iteration time.

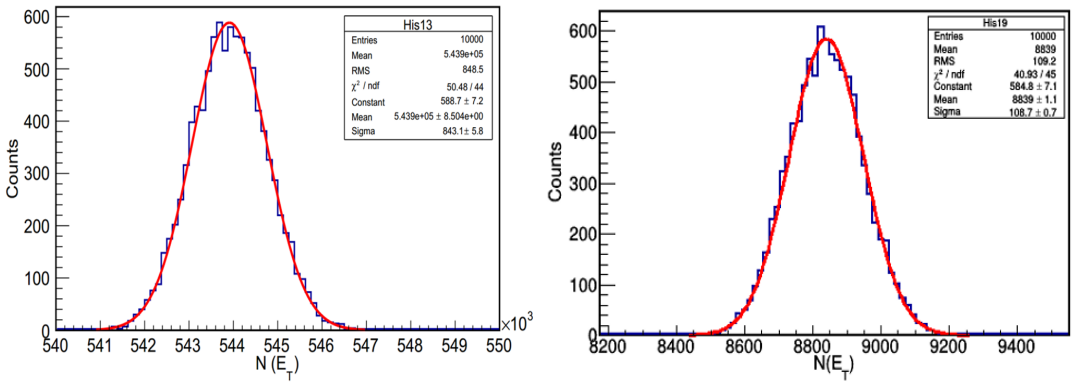

FIGURE 4.33: The distribution of $N'(E_T^j)$ obtained with the TOY-MC method in energy bin of 398.1 GeV – 630.9 GeV (left) and 6309.5 GeV – 10000 GeV (right). The distributions are fitted with Gauss function.

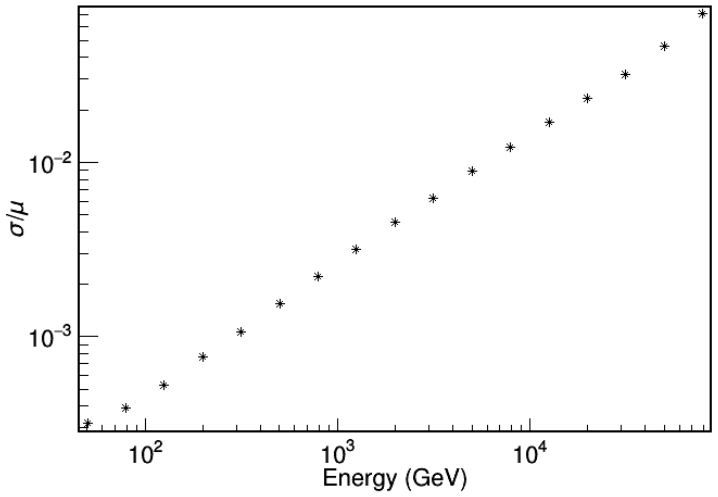

FIGURE 4.34: The σ/μ of the Gauss distribution as a function of energy.

applied and verified in [94]. The number of the events in i-th bin of the BGO energy ($N(E_{BGO}^i)$) will be used as the mean value of a Poisson distribution. Then a random number $N'(E_{BGO}^i)$ will be generated following the probability density function of the Poisson distribution. By using $N'(E_{BGO}^i)$ to replace $N(E_{BGO}^i)$ in the i-th bin, a new observed spectrum can be obtained. Performing the unfolding procedures on the new observed spectrum, a new unfolded result of the energy distribution, represented by $N'(E_T^j)$, can be obtained. Repeat this routine for 10000 times, a new $N'(E_T^j)$ will be produced each time. The distribution of $N'(E_T^j)$ in each energy bin can be fitted with a Gauss function. The $N'(E_T^j)$ distributions in two energy intervals are shown in Fig. 4.33. The ratio between the Gauss sigma and mean value as a function of energy is presented in Fig. 4.34. This ratio can be regarded as the reference for computing the statistical uncertainties.

In order to verify the TOY-MC method, a comparison are make between the statistical

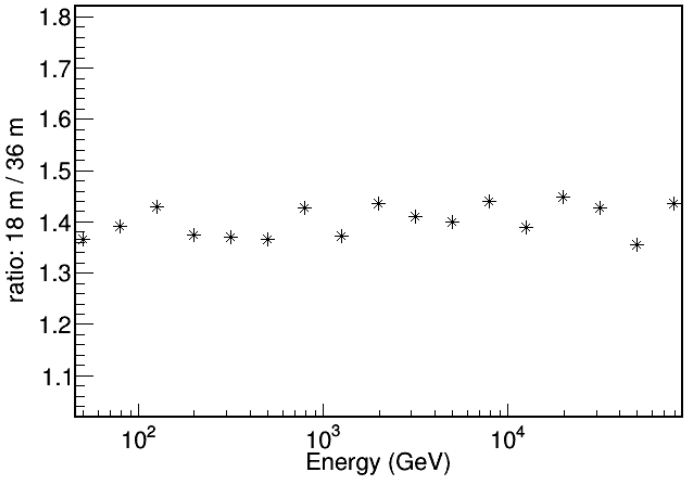

FIGURE 4.35: The ratio between the statistical errors of 18 months and 36 months data computed by using the TOY-MC method.

errors produced by TOY-MC method with 18 months and 36 months of orbit data. The ratio between the two groups of the error is expected to be $\sqrt{2}$. In Fig. 4.35 the ratio regarding the particle primary energy is presented. The value of the ratio slightly fluctuate around 1.4, which is consistent with the expectation.

4.8 Results of proton + helium flux

The derivation of CR flux has been shown in equation 4.1. It can be modified in terms of each bin of the flux as:

$$\Phi_i = \frac{N_i}{\Delta T \times A_{acc-i} \times \Delta E_i} \tag{4.19}$$

where Φ_i represents the flux in i-th energy bin, N_i is the number of events in i-th bin (after the unfolding procedures), ΔT equals 5.9×10^7s (as it was computed in section 4.2), A_{acc-i} is the acceptance in i-th bin (calculated in section 4.6, see Fig. 4.28), ΔE_i represents the energy interval of i-th bin. By using of equation 4.19, the flux for each bin can be derived. In this section, we will first introduce the computation of the systematic uncertainties, then the H + He flux will be presented with both statistical and systematic uncertainties.

4.8.1 Systematic uncertainties

The systematic uncertainties for the H + He spectrum mainly come from the following aspects:

- The acceptance. The acceptance is computed by MC then used to data. Therefore, the difference between MC and data selection efficiencies leads to a certain amount of systematic uncertainties;
- The ratio between MC H and He in the response matrix. Since the response matrix used in unfolding process is filled by MC H and He samples, the ratio between the numbers of H and He samples could affect the unfolding result and lead to different spectra;
- The hadronic model. In the MC simulation of DAMPE, the selection of different hadronic reaction models might affect the behaviours of H and He samples in the BGO, which could affect the final spectra;
- The PSD correction in the MC. In section 4.4.5, we corrected the energy deposition in the PSD for the MC to match the real data. The effect of this correction on the spectrum is studied and regarded as a source of the systematic uncertainty.
- The contamination from the heavier nuclei (with $Z > 2$).
- The contamination from the electron and positron particles. This issue has been discussed in section 4.4.4 and the contamination is negligible (less than 0.1%).

The calculation of the systematic uncertainties due to the above issues will be discussed one by one as follows.

The acceptance

In section 4.5, the efficiency differences between MC and data for the three groups of selection cut have been estimated regarding the BGO energies of the candidates (as shown in Fig. 4.21, 4.26, 4.27). In order to transfer the differences into the true energy (or primary energy E_T) of events, the unfolding equation can be referred to. In this case, the equation 4.16 can be re-written as:

$$N(E_T^i) = \sum_{j=1}^{n} P(E_T^i|E_{BGO}^j) R_{Sel}^j N(E_{BGO}^j) \ , \tag{4.20}$$

where R_{Sel}^j is the selection efficiency (high energy trigger, track selection and charge reconstruction efficiencies) ratio between MC and data in j-th energy bin. The differences between the efficiencies of MC and data for these three groups of selection are

considered as constants regarding the energy (see section 4.5). Thus R^{j}_{Sel} in Eq. 4.20 is a constant, and will not be affected by the unfolding procedures. Therefore, we have the differences of 6% for the high energy trigger efficiency (σ_{HET}), 4% for the charge reconstruction efficiency(σ_{Char}), 4% for the STK track selection efficiencies (σ_{Track}). In total the systematic uncertainty due to the acceptance (or selection efficiency) is:

$$\begin{aligned}\sigma_{Acc} &= \sqrt{\sigma^2_{HET} + \sigma^2_{Char} + \sigma^2_{Track}} \\ &= \sqrt{(6\%)^2 + (4\%)^2 + (4\%)^2} \\ &= 8.24\% \ .\end{aligned} \tag{4.21}$$

The ratio between H and He samples in the response matrix

The response matrix $P(E^{j}_{BGO}|E^{i}_{T})$ (as shown in Fig. 4.31) are produced by MC H and He samples. An issues towards the response matrix should be discussed: the proportion between the numbers of H and He samples in the matrix could affect the value of $P(E^{j}_{O}|E^{j}_{T})$, thus leads to a different unfolding result. The H-He ratio from previous measurements could be referred to to decrease the systematic uncertainty. There are various measurements on the CR H and He fluxes, for instance, in Fig .4.31, the H-He ratios measured by AMS-02 (for spectral energy $<$ 1 TeV) + CREAM-III(for spectral energy $>$ 1 TeV) are used to produce the response matrix. The idea for deriving the systematic uncertainty due to the H-He ratio is that keeping all the other conditions unchanged (include all the selection cuts and unfolding procedures), but modifying the H-He ratio in $P(E^{j}_{O}|E^{j}_{T})$ following different experiments: the ATIC-02 [99] or PAMELA [98] (for spectral energy $<$ 1 TeV) + NUCLEON [113] (for spectral energy $>$ 1 TeV) measurements. The spectrum obtained with the ratio of AMS-02 + CREAM-III will be regarded as the benchmark (the reason for this will be discussed later) and compared with the other two spectra (referring the H-He ratio of ATIC-02 and PAMELA + NUCLEON measurements), the spectral differences are used to derive the systematic uncertainties.

In Fig. 4.36, the response matrix with H-He ratio following the ATIC-02 measurements are presented. The HET efficiencies for MC and data are shown in the left panel of Fig. 4.37. The HET efficiency difference between the MC and data is around 11% (right of Fig. 4.37), which is higher than the case with the ratio referring the AMS-02 + CREAM-III measurements (6%, Fig. 4.21). The response matrix and corresponding HET efficiency with H-He ratio following the PAMELA + NUCLEON measurement is shown in Fig. 4.38 and Fig. 4.39. In this case, the HET efficiency difference between the MC and data is around 10%, which is also larger than the case when the H-He ratio is referring to the AMS-02 + CREAM-III measurements.

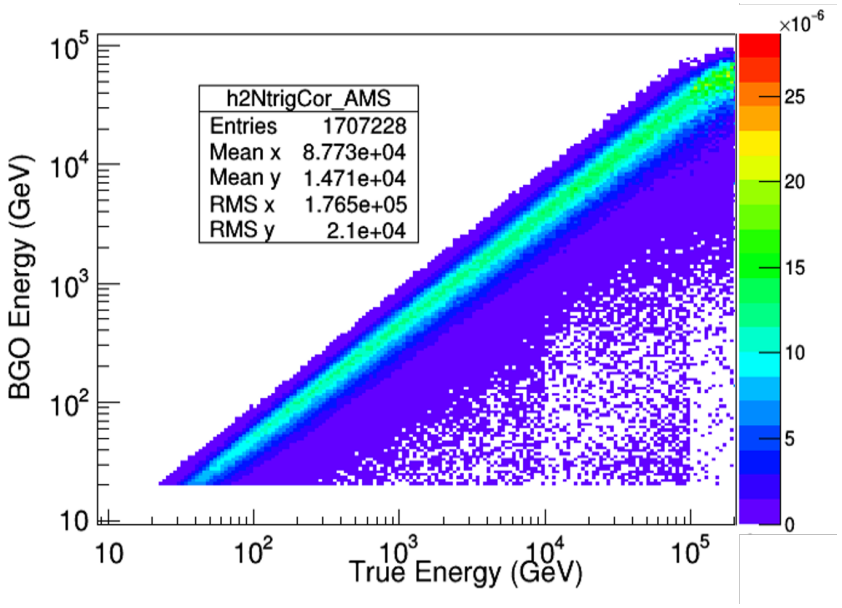

FIGURE 4.36: The response matrix with H-He ratio referring to the ATIC-02 measurements.

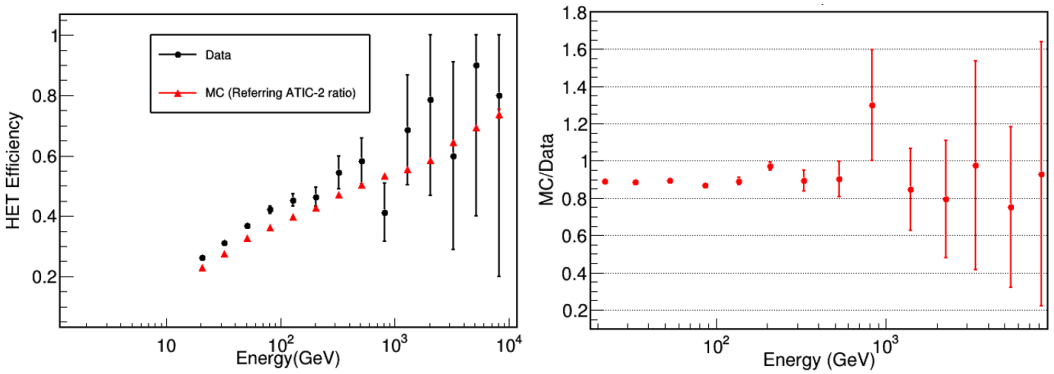

FIGURE 4.37: The high energy trigger efficiency of data (black points) and MC (red triangles) as functions of BGO energy with H-He ratio referring ATIC-02 measurement (left), and the efficiency difference between the MC and data (right).

Considering the behaviours in HET efficiency, the spectrum with H-He ratio referring to AMS-02 + CREAM-III measurements is regarded as the benchmark spectrum. The three spectra are shown in Fig. 4.40. The differences between the other two spectra and benchmark spectrum is presented in Fig. 4.41. Since the spectrum referring ATIC-02 measurement shows a larger difference with the benchmark one, we will use their comparison to compute the systematic uncertainties. The difference is directly taken as the amount of the systematic uncertainty, which are 1% for E $<$ 300 GeV, 2% for 300 GeV$<$ E $>$ 10 TeV, and 1% for E $>$ 10 TeV.

The hadronic model

Due to the limited knowledge of hadronic interaction process at high energy regions, the H + He spectrum is partially dependent on the used hadronic model in MC simulation.

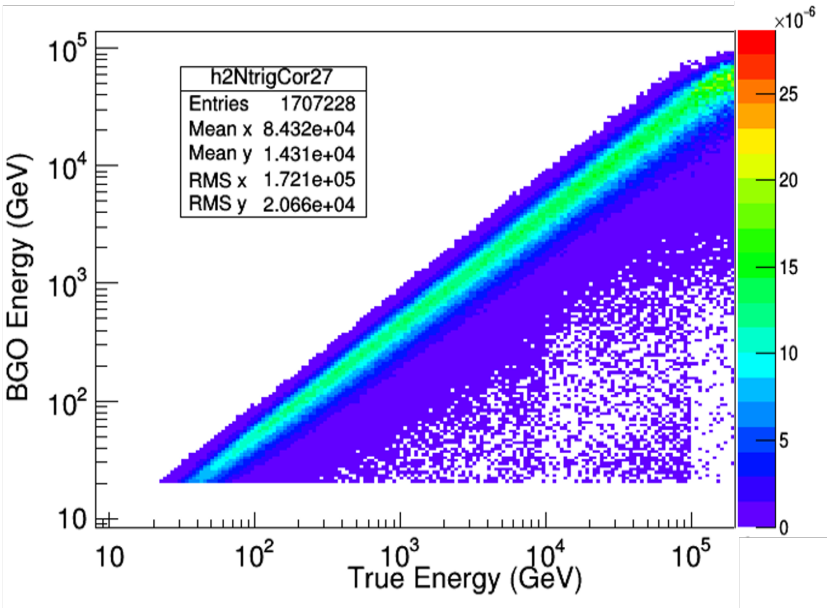

FIGURE 4.38: The response matrix with H-He ratio referring the PAMELA + NUCLEON measurements.

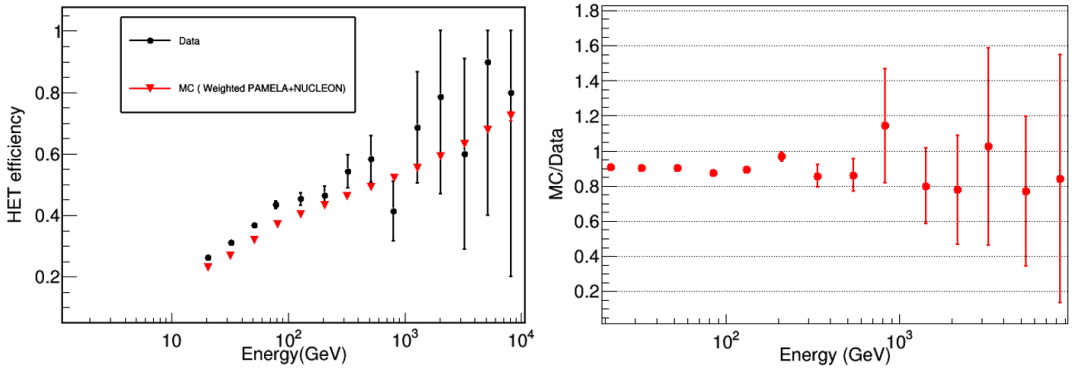

FIGURE 4.39: The high energy trigger efficiency of real data (black points) and MC (red triangles) as functions of BGO energy with H-He ratio referring PAMELA + NUCLEON measurements (left), and the difference between MC and data (right).

In this work, the presented results are all based on the FTFP + DPMJET models. In order to assess the systematic uncertainty due to the hadronic models, the spectrum based on QGSP model is also derived and compared with spectrum based on the FTFP + DMPJET models. The discrepancy between the two spectra will be referred for the evaluation of the uncertainty. The HET efficiencies of MC with QGSP model and data are compared in Fig. 4.42. The difference is around 13% at energy region < 1 TeV, which is higher than the result shown in Fig. 4.21 (6%). This can be another supportive reason for using the spectrum based on FTFP+DPMJET models as the benchmark model.

Both spectra using the FTFP and QGSP models are shown in Fig. 4.43. Since for MC with QGSP model, we only have the simulated samples up to 100 TeV for both H and He

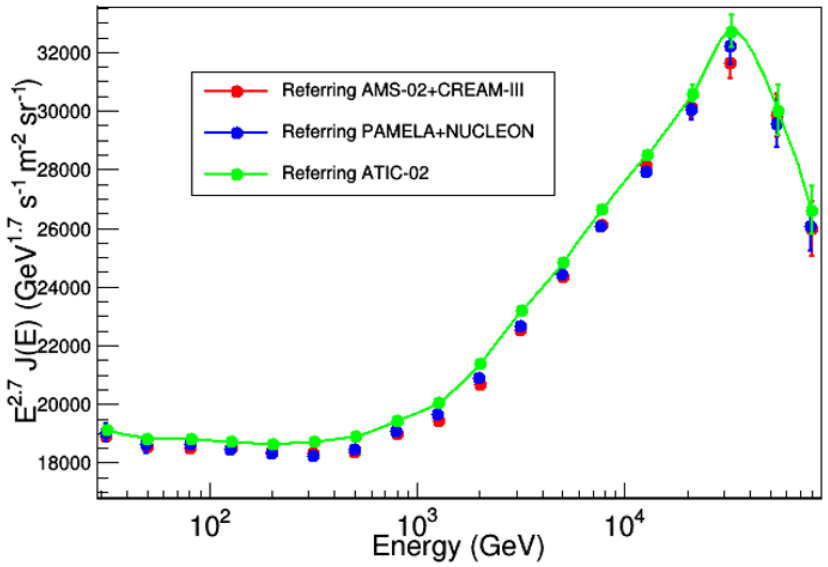

FIGURE 4.40: The spectra derived from three different H-He ratios in response matrix. The fluxes have been multiplied by $E^{(2.7)}$ to enhance the visibility. In order to clearly see the comparison, the spectrum referring the ATIC-02 measurements (green points), which is higher than the spectrum referring PAMELA + NUCLEON measurements (blue points) and the one referring AMS-02 + CREAM-III measurements (red points), is linked by a green line.

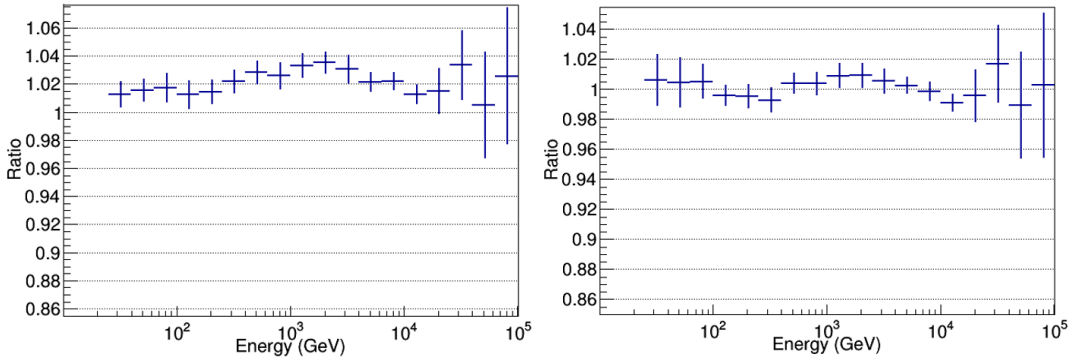

FIGURE 4.41: Left: the difference between the spectrum with H-He ratio referring ATIC-02 measurements and the benchmark spectrum. Right: the difference between the spectrum with H-He ratio referring PAMELA + NUCLEON measurements and the benchmark spectrum.

nuclei, therefore, the MC-dependent unfolding method can only reconstruct the particle energy with a maximum of 100 TeV. The particles with primary energy larger than that will be assigned into the last few bins of the spectrum. So in Fig. 4.43, the last two points of the QGSP spectrum show an abnormal excess which should not be taken into account. The ratio between the two fluxes in each bin are shown in Fig. 4.44. The last two points are not reliable due to the absence of the QGSP MC samples at higher energies ($>$ 100 TeV). However, if we ignore the last two points, the ratio is stable at around 90% as the energy larger than 2 TeV. Therefore, we adopt the ratio of 90% until 100 TeV as the reference for systematic uncertainty. The uncertainty regarding different

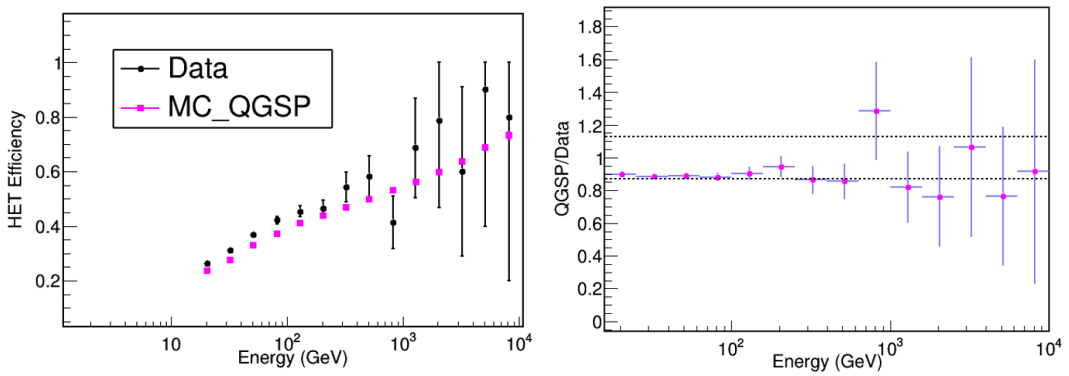

FIGURE 4.42: Left: the high energy trigger efficiency of data (black points) and the MC with QGSP model (pink squares). Right: the efficiency difference between the MC and data, the dash lines marks the number of 0.87 and 1.13 indicating the difference is within 13%.

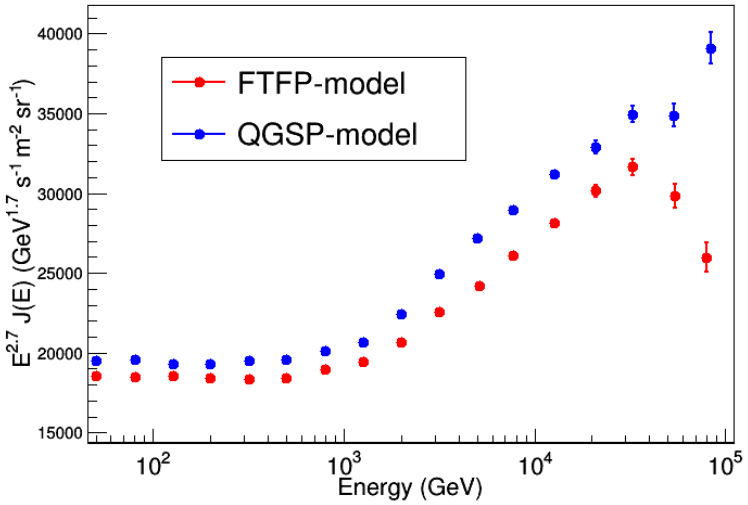

FIGURE 4.43: The spectra derived from both FTFP (red points) and the QGSP (blue points) models. The fluxes has been multiplied by $E^{2.7}$. The error bars only represent the statistical uncertainties (see the text for the abnormal behaviour of the last 2 data points of QGSP model).

energy intervals of the spectrum are shown in Tbl. 4.1.

Energy(GeV)	39.8-1584.8	1584.8-2511.8	2511.8-100000.0
uncertainties	5%	7.4%	10%

TABLE 4.1: The systematic uncertainties due to the hadronic models (see text).

PSD correction in the MC

The proton spectrum analysis group of DAMPE performed a specific study on the phenomenon of discrepancy between MC and data for the PSD energy measurement [5]. A correlation between the discrepancy and the Z-axis coordinate of the first particle-detector interaction is found. In Fig. 4.45, the distributions of the stop Z coordinates of MC proton particles are shown. There are two groups of data in each plot, one group

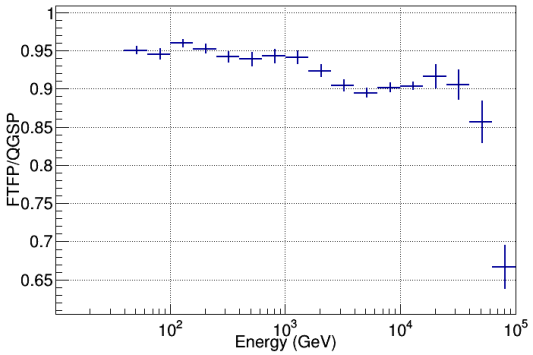

FIGURE 4.44: The ratio between the FTFP and QGSP spectra.

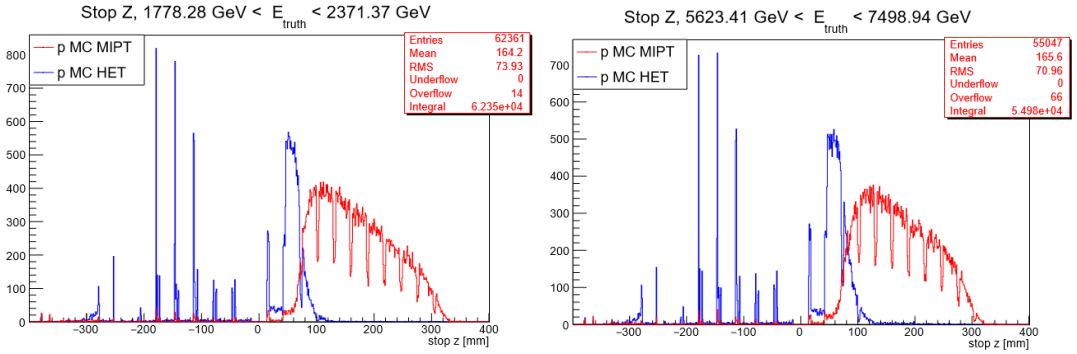

FIGURE 4.45: Distributions of the Z coordinate of the primary interaction for MC proton particles. The events comes from two primary energy (E_{true}) bins. The blue line represents the events with the HET, while the red line represents the event with the MIP trigger. The plots are from [5].

requires the protons must activate the hgh energy trigger, meanwhile the other group requires MIP trigger. In the distribution of HET protons, there are several peaks before the events reaching the BGO calorimeter (with Z coordinate > 0 mm). For instance, the two peaks at around -300 mm are due to particles interacting with two layers of the PSD. The other six peaks are attributed to interactions in the six layers of the STK. On the other hand, the distributions of MIP trigger protons show no peak with Z coordinate $<$ 0 mm, which indicates the events turning into secondary particles only when they reach the BGO.

If the HET selection is replaced by the MIP trigger in the selections described in section 4.4, the MC and data difference for the PSD energy measurement (as shown in Fig. 4.15 and Fig.4.16) is much less as it was shown in Fig. 4.46. Considering that there will be a large number of back-splash particles reaching the PSD if incident particles induce a shower before arriving at the calorimeter, therefore, the discrepancy between MC and data PSD measurements can be explained as MC overestimating the particle interactions before they reach the BGO, thus results in more back-splash particles entering the PSD in MC than that in data. More discuss on this issue can be found in [5].

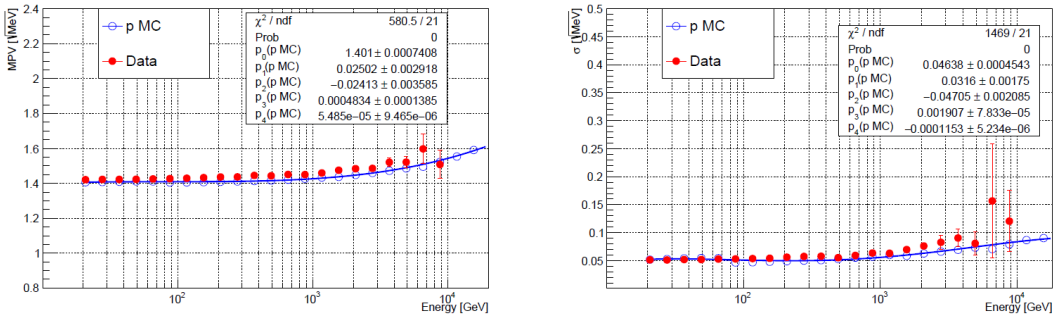

FIGURE 4.46: The MPV (left) and sigma (right) of the distributions of PSD energy measurements for MIP proton events. The MC results are fitted with a fourth order polynomial function. The plots come from [5].

In order to assess the influence of the PSD correction on the H + He spectrum, the charge reconstruction efficiency is checked again in the case without the PSD correction. The used method is the same as described in section 4.5.2. Without the PSD correction, the efficiencies for each layer of the PSD are shown in Fig. 4.47. The difference between the MC and data is within 7% for PSD X layer and 5% for PSD Y layer, which is larger than the results in section 4.5.2. (within 3%). The spectrum without the PSD correction is shown in Fig. 4.48 where the spectrum with the PSD correction is also plotted for comparison. The spectral difference regarding different energy intervals are shown in Tbl. 4.2. The PSD correction has only small effect on the H + He spectrum. However, without the correction, the discrepancy between the MC and data for the charge reconstruction efficiency becomes larger (which will enlarge the systematic uncertainties). Therefore, the PSD correction will be kept. The influence of the correction on the spectrum (Tbl. 4.2) will be regarded as systematic uncertainty of the spectrum.

Energy(TeV)	<10.0	10.0-39.81	39.81-100.0
uncertainty	1%	2%	3%

TABLE 4.2: The systematic uncertainties due to the PSD correction.

Contamination from heavy nuclei

The H + He spectrum has a slight contamination from heavy nuclei due to the fact that CR fluxes of lithium (Li), beryllium (Be), boron (B) are much lower compared with H + He flux. Nevertheless, the effect of the heavy nuclei, including Li, Be, B, carbon (C), on the H + He spectrum is studied by using of a template fit. The fluxes of these elements are so small that if the distribution of the PSD measurement ($E_{PSD_{Glo}}$) with the events from one BGO energy bin is plotted, the existence of these elements can hardly be noticed. For instance, in Fig. 4.19, the Li nuclei are supposed to be observed at around 18 MeV, however, no bump can be found due to the statistics issue. In order to assess the contamination quantitatively, we plot the distribution of $E_{PSD_{Glo}}$ with events integrating along all the BGO energies (as shown in Fig. 4.49). A template fit method is

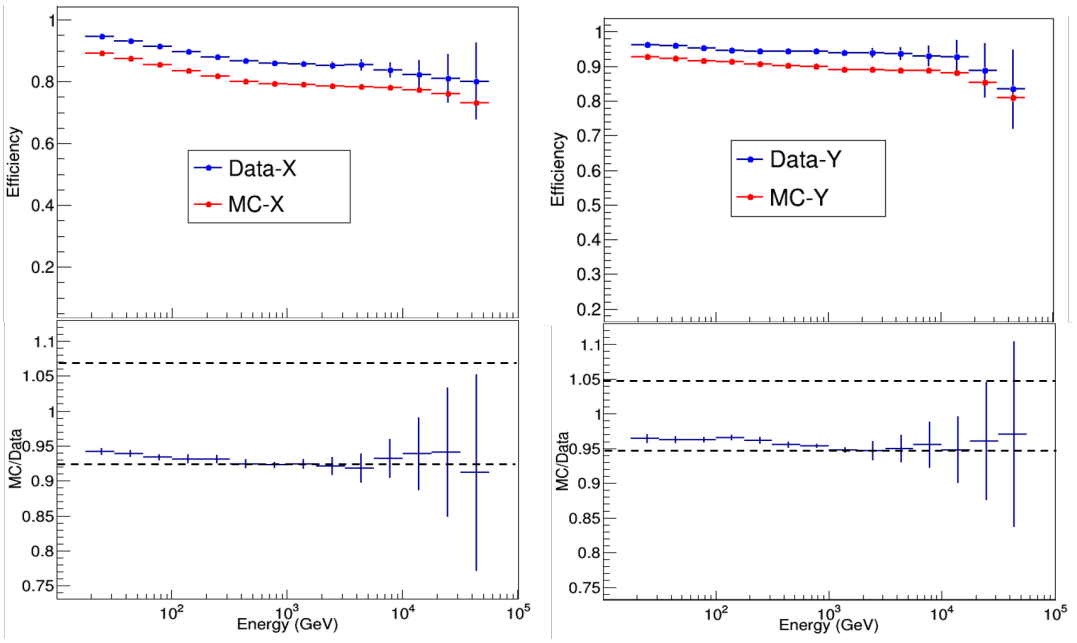

FIGURE 4.47: The charge reconstruction efficiency (with MC as red points and data as blue points) for PSD X (left, upper) and Y layer (right, upper) and the ratios between MC and data efficiencies (left lower for PSD X layer and right lower for PSD Y layer).

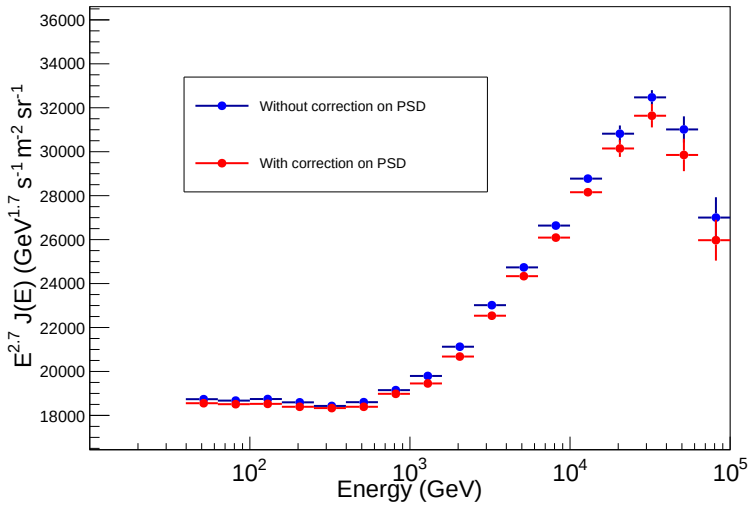

FIGURE 4.48: Comparison between the spectra with and without the PSD correction.

used for the distribution of each element. To decide the PSD selection range for H + He particles in this case, we refer to the functions shown as red lines in Fig. 4.20. First, 25 MeV is chosen as the upper boundary for H + He nuclei, which is a relatively large value since in Fig. 4.20, it represents the boundary of events with BGO energy around few tens TeV (after unfolding, most of these events will be put into energy bins around 100 TeV). On the other hand, when choosing 25 MeV of $E_{PSD_{Glo}}$ as the threshold, most of Li and part of Be events are included. Therefore, the contamination will be overestimated. In Tbl. 4.3, the contamination from each element is shown. In total, the contamination is around 0.7%, which is a small amount comparing with other systematic uncertainties.

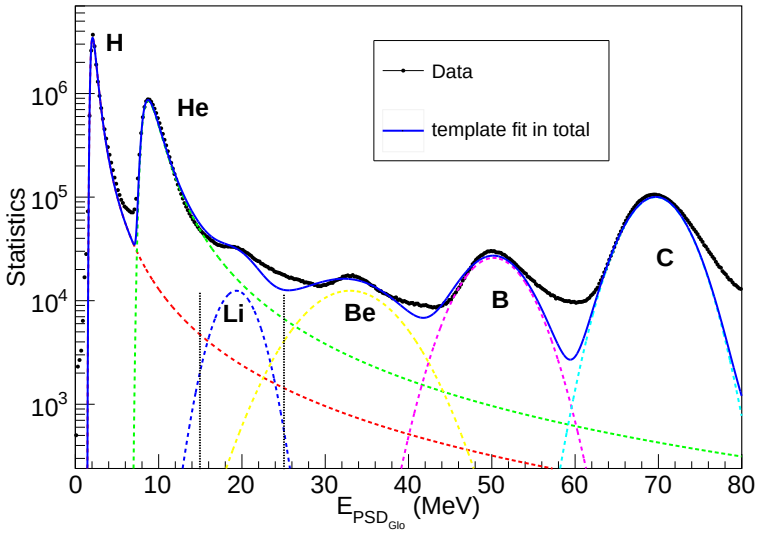

FIGURE 4.49: The distribution of $E_{PSD_{Glo}}$ integrating along the BGO energies. The template fit is used for each element. The black dash lines mark two different thresholds (15 MeV and 25 MeV) for selecting H + He particles.

In Tbl. 4.4, we present the contamination if the threshold energy for recognizing H + He nuclei is chosen as 15 MeV (an average value of $E_{PSD_{Glo}}$ for selecting H + He nuclei). In this case, the contamination is around 0.03%. This discussion shows that the effect of the CR heavy nuclei (with charge > 2) on H +He spectrum is negligible, thus no systematic uncertainties will be added because of the heavy nuclei contamination.

Element	Li	Be	B	C	Total
Contamination	0.71%	0.019%	—	—	0.73%

TABLE 4.3: Contamination from heavy nuclei when the up threshold of $E_{PSD_{Glo}}$ is chosen at 25 MeV.

Element	Li	Be	B	C	Total
Contamination	0.03%	—	—	—	0.03%

TABLE 4.4: Contamination from heavy nuclei when the up threshold of $E_{PSD_{Glo}}$ is chosen at 15 MeV.

Total systematic uncertainty

The total uncertainty equals the square root of quadratic sum of uncertainties described in this section (as shown in Fig. 4.50). At energy region of E < 2.5 TeV, the uncertainty is around 9.5%, then it grows with an increasing energy and gets stable at around 13% after 4 TeV. At the low energy region (E < 3 TeV), the uncertainty mainly comes from the acceptance. Meanwhile the hadronic model becomes the main contributor to the uncertainty at high energy region (E > 3 TeV). This may be due to the scarce experiment data on high energy region, which bring a larger discrepancy between different hadron

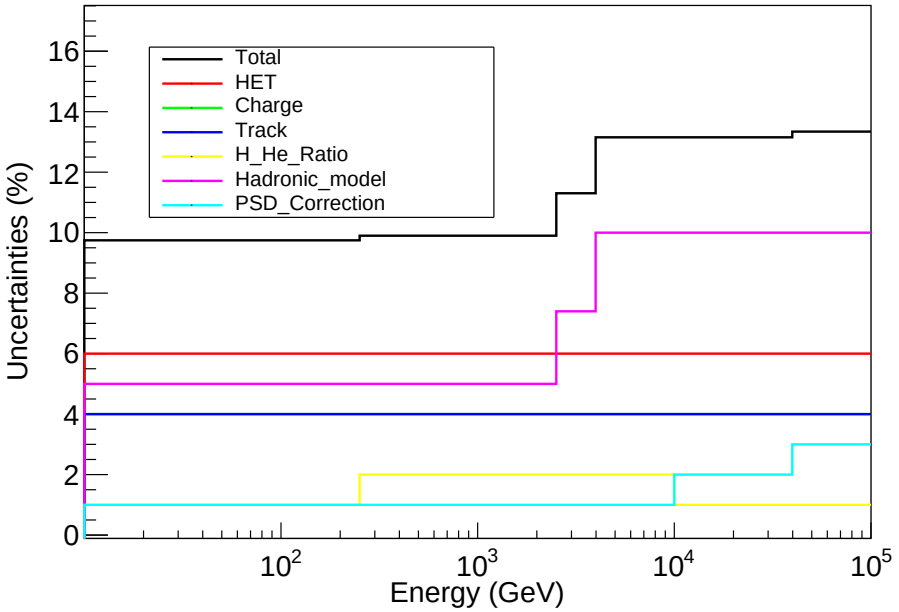

FIGURE 4.50: Each part of the systematic uncertainty for the spectrum.

reaction models. This leads to the selection of hadronic model being the dominating factor for the systematic uncertainties at high energy.

4.8.2 The proton + helium flux

After all the selection cuts, we are able to compute the H + He flux basing on 3.77×10^7 CR events. The BGO energy distribution of these candidates is shown in Fig. 4.51. In order to see the effect of the unfolding procedure, in Tbl. 4.5, the numbers of events in each energy bin before and after the energy unfolding procedures are presented. As the final result, the H + He spectrum with energy interval 50 GeV to 100 TeV is presented in Fig. 4.52 where the flux is multiplied by $E^{2.7}$ to enhance the visibility of the spectral features. The error bars represent the statistical uncertainty, meanwhile the systematic uncertainties are represented by the shadow region. The DAMPE H + He spectrum reveals the spectral hardening at $\sim$ 500 GeV, moreover, a spectral softening at around $\sim$ 30 TeV can also be observed. The flux and the corresponding statistical and systematic uncertainties are presented in Tbl. 4.6.

The H + He flux measured by DAMPE is compared with previous experiments in Fig. 4.53. DAMPE result has a good agreement with the ATIC-02, NUCLEON and HAWC measurements. Considering the proton flux measured by DAMPE [6] where a softening at $\sim$ 13 TeV is observed, the softening feature in the H + He spectrum could come from the same mechanism with the one observed in proton spectrum. Considering the energy of the softening point, it could be a rigidity dependent feature. Several models have been

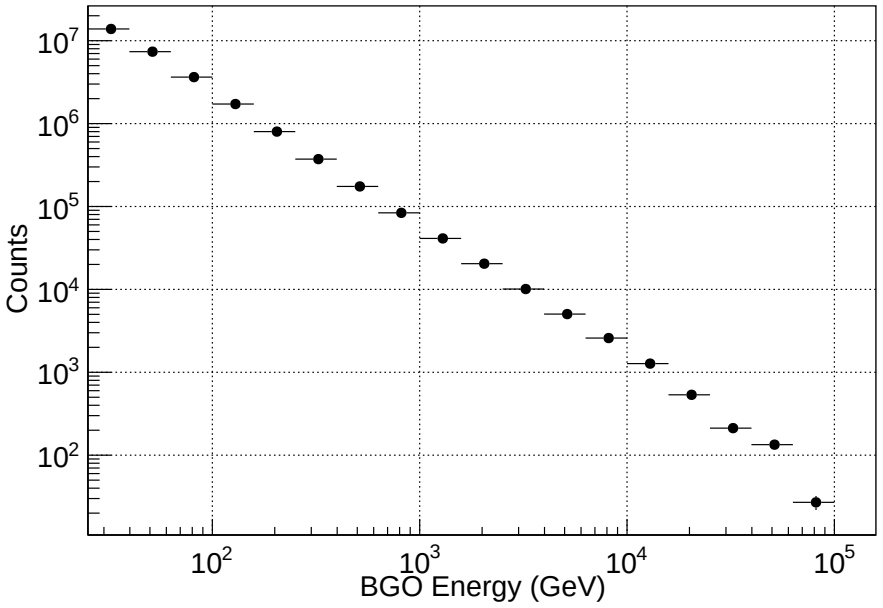

FIGURE 4.51: The selected H + He candidates as a function of the BGO energy.

Energy bin (GeV)	Events before the unfolding	Events after the unfolding
25.1-39.8	24998978	3813946
39.8-63.1	7372579	12962485
63.1-100.0	3637847	9892676
100.0-158.5	172219	5518425
158.5-251.2	800674	2825416
251.2-398.1	372859	1372626
398.1-630.9	174554	665092
630.9-1000.0	83852	324701
1000.0-1584.9	41191	157393
1584.9-2511.9	20429	79340
2511.9-3981.1	10100	40879
3981.1-6309.6	5037	20853
6309.6-10000.0	2588	10691
10000.0-15848.9	1273	5483
15848.9-25118.9	535	2807
25118.9-39810.7	212	1395
39810.7-63095.7	134	626
63095.7-100000.0	27	254

TABLE 4.5: The amount of H + He candidates in each energy bin interval before and after the unfolding procedure.

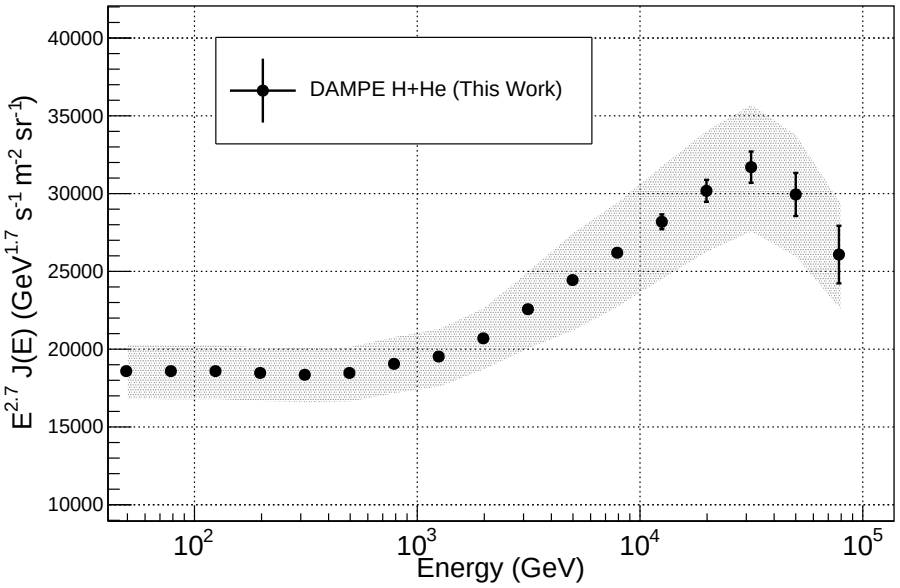

FIGURE 4.52: The preliminary H + He flux multiplied by $E^{2.7}$. The error bars represent the statistical uncertainties, the black shadow region marks the systematic uncertainties.

Energy (GeV)	Energy bin interval (GeV)	$\Phi \pm \sigma_{stat} \pm \sigma_{sys}$ (GeV^{-1} s^{-1} m^{-2} sr^{-1})
49.8	39.8-63.1	$(4.77 \pm 0.001 \pm 0.45) \times 10^{-1}$
78.9	63.1-100.0	$(1.37 \pm 0.0005 \pm 0.13) \times 10^{-1}$
125.1	100.0-158.5	$(3.96 \pm 0.002 \pm 0.37) \times 10^{-2}$
198.3	158.5-251.2	$(1.13 \pm 0.0008 \pm 0.11) \times 10^{-2}$
314.2	251.2-398.1	$(3.26 \pm 0.003 \pm 0.31) \times 10^{-3}$
498.1	398.1-630.9	$(9.43 \pm 0.01 \pm 0.90) \times 10^{-4}$
789.5	630.9-1000.0	$(2.81 \pm 0.01 \pm 0.27) \times 10^{-4}$
1251.2	1000.0-1584.9	$(8.30 \pm 0.03 \pm 0.79) \times 10^{-5}$
1983.0	1584.9-2511.9	$(2.54 \pm 0.01 \pm 0.24) \times 10^{-5}$
3142.9	2511.9-3981.1	$(8.00 \pm 0.05 \pm 0.88) \times 10^{-6}$
4981.2	3981.1-6309.6	$(2.50 \pm 0.02 \pm 0.32) \times 10^{-6}$
7894.6	6309.6-10000.0	$(7.70 \pm 0.09 \pm 0.99) \times 10^{-7}$
12512.6	10000.0-15848.9	$(2.40 \pm 0.04 \pm 0.31) \times 10^{-7}$
19830.3	15848.9-25118.9	$(7.4 \pm 0.17 \pm 0.95) \times 10^{-8}$
31429.2	25118.9-39810.7	$(2.24 \pm 0.07 \pm 0.29) \times 10^{-8}$
49812.5	39810.7-63095.7	$(6.10 \pm 0.28 \pm 0.8) \times 10^{-9}$
78946.7	63095.7-100000.0	$(1.53 \pm 0.11 \pm 0.20) \times 10^{-9}$

TABLE 4.6: The flux and the uncertainties for different energy intervals.

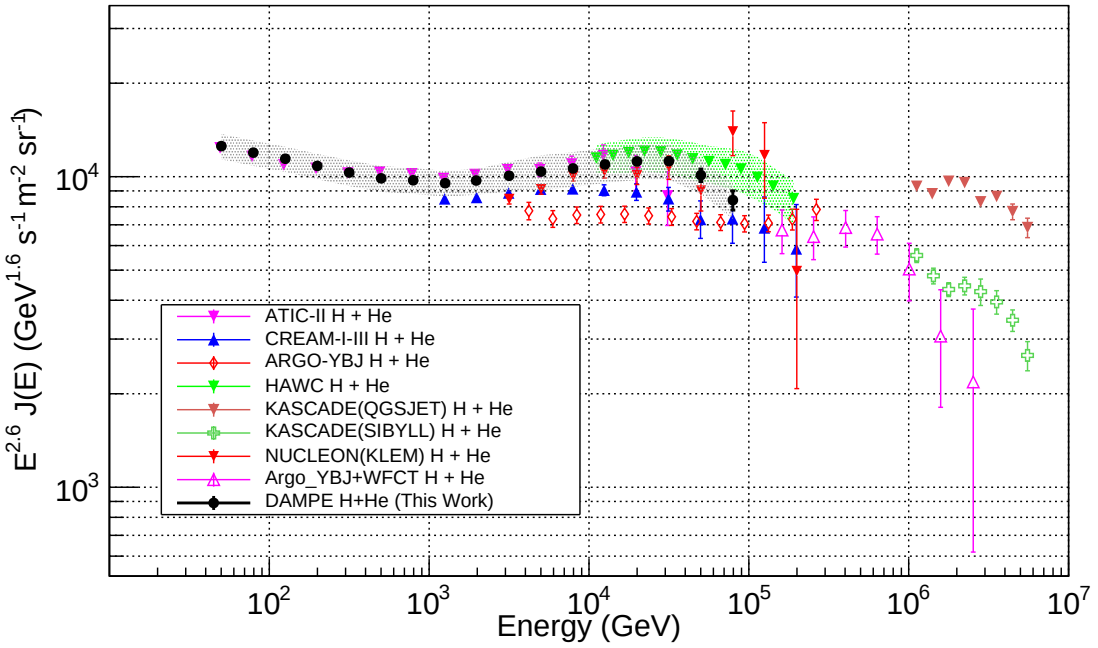

FIGURE 4.53: The DAMPE H + He flux multiplied by $E^{2.6}$. Some of previous measurements on CR H + He nuclei are also presented.

proposed to explain this feature [114], which indicating that the softening depends on rigidity and is supposed to be visible for all the CR nuclei spectra. At lower energy, the DAMPE H + He spectrum shows a spectral hardening at $\sim$ 500 GeV which is consistent with the AMS-02 and PAMELA helium measurements. At higher energy (E $>$ 100 TeV), the extrapolation of DAMPE spectrum has a good agreement with KASCADE (SIBYLL) [115] and ARGO (YBJ + WFCT) [48] measurements. There is a discrepancy between the extrapolation of the DAMPE spectrum and KASCADE (QGSJET)[115] measurement, if the latter is the real case, then another spectral hardening would be observed at energy interval between 100 TeV and 1 PeV. Given these questions, a precise CR flux measurement at energy larger than 100 TeV with less systematic uncertainty could enhance our understanding on the spectrum features. Several experiments have been proposed or partly put in use now (for instance, High Energy cosmic-Radiation Detector (HERD) [116] and the Large High Altitude Air Shower Observatory (LHAASO) [117]).

Summary and conclusions

This thesis concentrates on the DAMPE measurement of CR proton + helium spectrum. DAMPE is a satellite-borne detector system for CR direct observation. The distinctive design on the detectors structure makes DAMPE capable to measure the CR nuclei up to energy of 100 TeV with unprecedented energy resolution. In chapter 2, we introduced the scientific goals and sub-detectors of DAMPE. Several topics can be studied with DAMPE including the search of a signature of dark matter particles in the lepton spectrum, the measurement of CR proton and helium spectra, the CR B/C fluxes ratio up to few tens TeV/n, gamma ray astronomy,etc (section 2.1). Given the scientific goals of DAMPE, the performances of the sub-detectors are highly demanding. The introduction for each sub-detector of DAMPE was presented in section 2.2. The charges of the CR particles are measured by the PSD which is located at the top of the whole system. Besides, the PSD is also used as a veto detector to identify the gamma and electron/positron events (section 2.2.1). The STK, arranged below the PSD, is in charge of reconstructing the trajectories of entering particles. For gamma ray events, the tungsten board, inserted between the layers of the STK, can provide a conversion into electron-positron pairs, thus measuring the direction of the gamma rays (section 2.2.2). The BGO calorimeter is the energy measurement device of DAMPE. By using of the deposited energies of events in the BGO, the primary energies can be reconstructed with an unfolding method. Moreover, by looking at the shower development in the BGO, electrons and protons can be identified (section 2.2.3). The NUD detector is assigned to enhance the capacity of DAMPE for identifying leptons and hadrons (section 2.2.4). In the last two sections of chapter 2, the data acquisition system and the coordinate system of DAMPE were introduced (section 2.3, 2.4).

The large uncertainty in a hadronic shower imposes difficulties on measuring the energy of hadrons with calorimeter (section 3.2). The measurement of CR nuclei is one of the main scientific goals of DAMPE, thus an effective method for reconstructing their energy is necessary. Three widely used reconstruction methods were discussed (section 3.3.1, 3.3.2 and 3.3.3), and their performances were test by using the MC samples. It turned out that the Bayes method can reconstruct the energy with least biases (2%). Meanwhile

the SVD and IDS methods produced the results with larger biases (5%) (section 3.4). In order to see the performance of the Bayes method in real data, the data of the proton beam with energies of 400 GeV and 150 GeV were used. The Bayes method proved its reliability working in real data by reconstructing the incident beam energy with good accuracy with only about 1% shift for 400 GeV beam data, and 2.7% for 150 GeV beam data (section 3.5). Given these test results, we decide to use the Bayes method in our analysis for energy reconstruction of proton + helium candidates.

In chapter 4, the proton + helium spectrum with energy from 40 GeV to 100 TeV was presented together with the analysis processes. In order to measure the flux, the essential factors includes the calculation of the exposure time (section 4.2), the selection of the candidates (section 4.4), using MC to compute the selection efficiency then deriving the acceptance (section 4.3, 4.6) and energy unfolding (section 4.7). The spectrum contains statistical and systematic uncertainties, a TOY-MC method was used to compute the statistical uncertainties (section 4.7.2), and the systematic uncertainties were composed by the effects from the acceptance, the ratio of proton and helium events in the response matrix, the PSD correction and the hadronic models. In totoal the systematic uncertainty is about 9.5% at energy region less than 2.5 TeV, then it grows slightly and get stable at about 13% at 6 TeV (section 4.8.1). The final spectrum is shown in section 4.8.2. A spectral hardening is observed at $\sim$ 500 GeV which is compatible with AMS-02 and PAMELA measurements. Moreover, in this analysis, a softening is found at $\sim$ 30 TeV. Considering the proton flux measured by DAMPE where a softening at $\sim$ 13 TeV is observed, the softening feature in the H + He spectrum could come from the same mechanism with the proton one, and it could be rigidity dependent. This is an important and unexpected feature, if confirmed by further evidences, it will be an important input for galactic CR modeling.

Appendix A

Geometric factor correction

The response of DAMPE to CR nuclei has been simulated by using of MC method. In the simulation, a hemisphere surface was used as the source for generating hadronic particles. However, the radii of the hemispheres for simulating proton and helium are different: The hemisphere radii are 1.38 m for proton, 1 m for helium, as shown in Fig. A.1. This difference leads to an issue in computing the acceptance of the detector. Since the proton + helium flux can be calculated as (equation 4.1):

$$\Phi(\mathrm{E}, \mathrm{E}+\mathrm{dE}) = \frac{\mathrm{N_{H+He}}(\mathrm{E}, \mathrm{E}+\mathrm{dE})}{\Delta \mathrm{T} \cdot \mathrm{A_{acc}} \cdot \mathrm{dE}}, \tag{A.1}$$

where $\mathrm{A_{acc}}$ is the acceptance and can be computed as:

$$\mathrm{A_{acc}} = \frac{\mathrm{N_{sel}}}{\mathrm{N_{gen}}} \cdot \varsigma \tag{A.2}$$

with $\mathrm{N_{gen}}$ and $\mathrm{N_{sel}}$ represent the number of the generated MC sample and the number of the sample that survive all the selection cuts respectively. The ratio $\mathrm{N_{sel}}/\mathrm{N_{gen}}$ is the efficiency of the selections. The geometric factor ς can be deducted as: $\varsigma = 2 \times \pi^2 \times \mathrm{radius}^2$. Since different hemisphere radii are used for different nucleus simulations, this result in two different acceptances in equation A.1. However, only an unique acceptance can be taken in order to calculate the proton + helium flux. Therefore, one of the geometric factors must be corrected to meet the requirement of equation A.1.

The radius of the proton-generating hemisphere is taken as benchmark. Then a compensation item which corresponds to the change of the ς must be added to the helium part in order to guarantee a corrected acceptance stays unchanged. Specifically, the ς of the helium is changed from 1m to 1.38m. The acceptance of the helium samples with

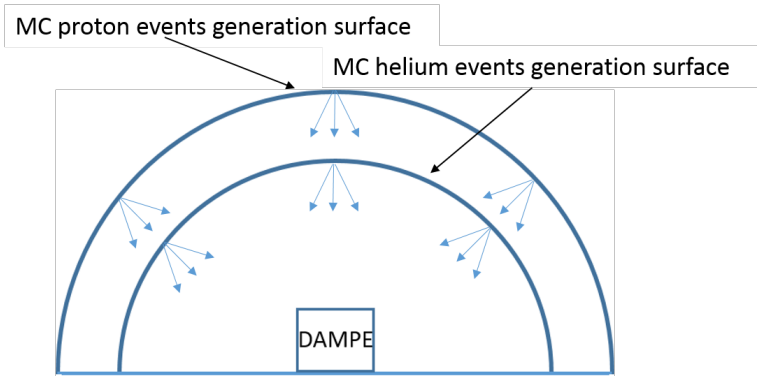

FIGURE A.1: The diagram of the MC particles generation surfaces for proton and helium nuclei. The particles are generated at random positions on the surface.

the geometric correction correspondingly should be:

$$A_{acc_{He}} = \frac{N_{sel_{He}}}{N_{gen_{He}}} \cdot \varsigma_H \cdot \frac{\varsigma_{He}}{\varsigma_H} \ , \tag{A.3}$$

ς_{He} is the geometric factor of helium and equals $2 \cdot \pi^2 \cdot 1^2$ sr m^2. Meanwhile the ς_H is the proton geometric factor and equals $2 \cdot \pi^2 \cdot 1.38^2$ sr m^2. The compensation item can be distributed to the efficiency calculation processes in practice. i.e. when we select the helium candidates in MC, a weight that equals the compensation item ($\varsigma_{He}/\varsigma_H$) is added to each survival helium events, thus the equation A.3 is implemented.

A similar method used in chapter 3 for testing the unfolding method (section 3.4) is applied in order to verify this correction method: The fitting functions of the AMS-02-measured proton and helium fluxes are used to weight a set of MC data, which produces the pseudo spectra following the AMS-02 measurements. Use these pseudo spectra as the input to DAMPE, and simulate the detector response. Finally, reconstruct the spectrum with and without using the correction method. The quality of the reconstructed spectrum can be estimated by comparing it with the spectral functions (the AMS-02 measurement [35, 36]). The situations of the reconstructed helium spectrum with and without the compensation item are presented in Fig. A.2. An incorrect result can be obtained if we use the geometric factor of the proton simulation ($2 \cdot \pi^2 \cdot 1.38^2$ m^2 sr) to helium directly (as shown in the left of Fig. A.2). However, once the change of the geometric factor is compensated in the the efficiency by multiplying the correction factor, a correct result can be obtained as shown in the right of A.2.

The similar process is also performed to a pseudo proton + helium spectrum. In this case, the acceptance is calculated as:

$$A_{acc_{H+He}} = \frac{N_{sel_H} + N_{sel_{He}} \cdot (\varsigma_{He}/\varsigma_H)}{N_{gen_H} + N_{gen_{He}}} \cdot \varsigma_H \ . \tag{A.4}$$

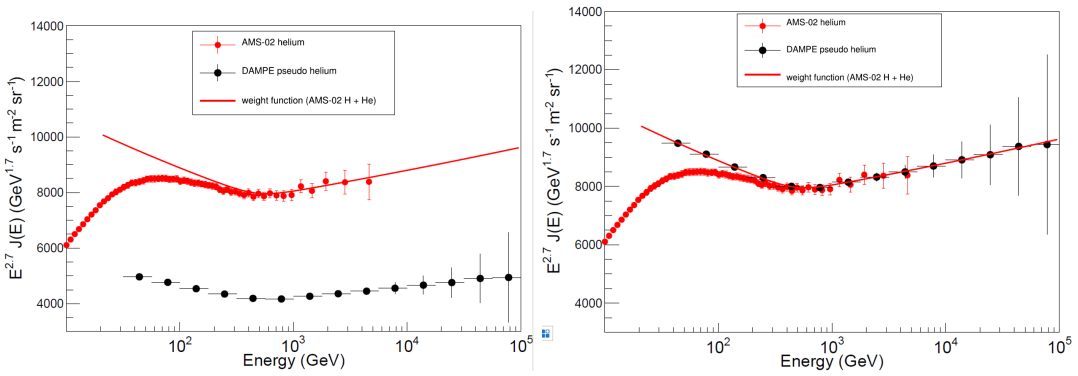

FIGURE A.2: Left: the reconstructed helium spectrum by using the geometric factor of proton simulation but without compensation on the selection efficiency. Right: the reconstructed helium spectrum by adopting the geometric factor of proton simulation and with the compensation on the selection efficiency.

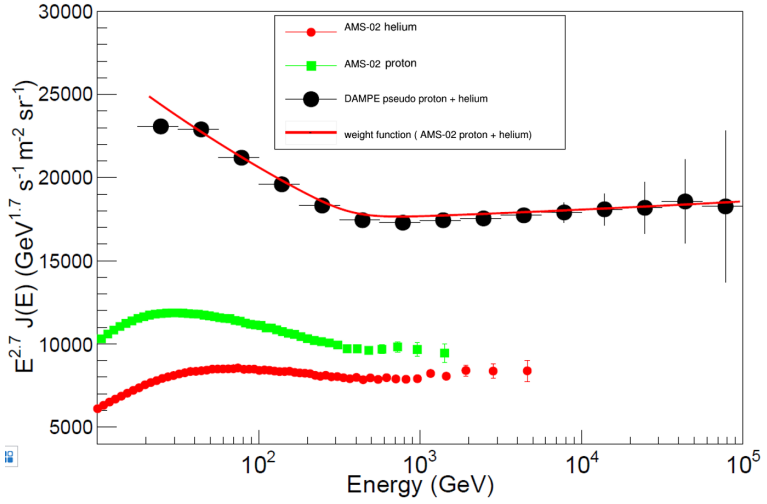

FIGURE A.3: The reconstructed proton + helium spectrum by using an unique geometric factor and with the compensation on the helium selection efficiency.

The reconstructed spectrum and its weighting function, which is derived by adding the AMS-02-measured proton and helium spectral fitting functions [35, 36], are presented in Fig. A.3. The reconstructed spectrum agree well with its weighting function, which implies the reliability of this correction method.

Acknowledgement

First, I would like to thank Gran Sasso Science Institute (GSSI) for offering me the chance to come to Italy for my Ph.D degree. GSSI is an amazing place with many excellent researchers gathering here. I have learned a lot from them. Moreover, as an international student, I experienced a different culture and lifestyle in Italy and had a lot of great time with my friends here. All these wonderful experiences are attributed to GSSI offering me the Ph.D position.

I would also like to thank Prof. Ivan De Mitri for his invaluable, and patient supervision. Prof. De Mitri offered me the chance to work for DAMPE collaboration and proactively helped me get into the group quickly. He gave me many constructive suggestions regarding my topic which assisted me to have a smooth and enjoyable Ph.D research life. Besides, I would like to thank Prof. Paolo Bernardini, Prof. Antonio Surdo who supported me a lot at the beginning of my Ph.D. topic. Thanks to Margherita Di Santo, Antonio De Benedittis, Ines Valino and Guillermo Torralba Elipe, as my colleagues. It has been a great time to work with them. We had a lot of great time together out of the work as well.

The three-year Ph.D life has given me a plenty of unforgettable memories: the excitement when I was informed for getting the position, the slight discomfort for adjusting a new lifestyle, the funny moment when I stumbled to pronounce the Italian words, the delicious arrosticini... All these experiences will be the treasures in my life.

Bibliography

[1] Maurizio Spurio. *Particles and Astrophysics – A multi-messenger approach.* Springer International Publishing, 2015.

[2] B. Bartoli, *et al.* Light-component spectrum of the primary cosmic rays in the multi-TeV region measured by the ARGO-YBJ experiment. *Physics Review D*, 85:092005, 2012.

[3] A. Tykhonov, *et al.* Internal alignment and position resolution of the silicon tracker of DAMPE determined with orbit data. *Nuclear Instruments and Methods in Physics Research Section A*, 893:43–56, 2018.

[4] G. Ambrosi, *et al.* Direct detection of a break in the teraelectronvolt cosmicray spectrum of electrons and positrons. *Nature*, 552:63–66, 2017.

[5] Stefania Vitillo. *Tracker Charge Identification and Measurement of the Proton Flux in Cosmic Rays with the DAMPE Experiment.* PhD thesis, Geneva University, 2018.

[6] Q. An, *et al.* Measurement of the cosmic ray proton spectrum from 40 GeV to 100 TeV with the DAMPE satellite. *Science Advances*, 5(9):eaax3793, 2019.

[7] M. S. Longair. *High Energy Astrophysics (Third Edition).* Cambridge university press, 2011.

[8] T. Wulf, *et al.* Observations on the radiation of high penetration power on the Eiffel tower. *Physikalische Zeitschrift*, 11:811, 1910.

[9] V. Hess. On the Observations of the Penetrating Radiation during Seven Balloon Flights. *arXiv:1808.02927v2*, 2018.

[10] A. Putze. Propagation of cosmic rays in the Earth's atmosphere. *HAL-IN2P3*, 41: in2p3–00106675, 2006.

[11] J. Clay, *et al.* Results of the Dutch Cosmic Ray Expedition 1933: II. The magnetic latitude effect of cosmic rays a magnetic longitude effect. *Physica*, 1(7-12):829–838, 1934.

[12] P. Auger, *et al.* Extensive cosmic-ray showers. *Review of Modern Physics*, 11 (7-12):288291, 1939.

[13] M. Schein, *et al.* The Nature of the Primary Cosmic Radiation and the Origin of the Mesotron. *Physics Review*, 59(7):615, 1941.

[14] M. Schein, *et al.* Evidence for a primary cosmic-ray particle with energy 10^{20} eV. *Physics Review Letter*, 10(4):146–148, 1963.

[15] P. Carlson, *et al.* Nationalism and internationalism in science: the case of the discovery of cosmic rays. *The European Physical Journal H*, 35:309329, 2010.

[16] F. Aharonian, *et al.* Primary particle acceleration above 100 TeV in the shell-type supernova remnant RX J1713.7-3946 with deep HESS observations. *Astronomy and Astrophysics*, 464:235–243, 2007.

[17] H. Netzer. *The Physics and Evolution of Active Galactic Nuclei.* Cambridge university press, 2013.

[18] E. Fermi. On the Origin of the Cosmic Radiation. *Physics Review*, 75(8):1169, 1949.

[19] E. Fermi. Galactic Magnetic Fields and the Origin of Cosmic Radiation. *Astrophysics Journal*, 119:1–6, 1954.

[20] W.I. Axford. The acceleration of cosmic rays by shock waves. *Proceedings of the 15th International Cosmic Ray Conference*, 11:132–135, 1977.

[21] G.F. Krymsky. A regular mechanism for the acceleration of charged particles on the front of a shock wave. *Akademiia Nauk SSSR, Doklady*, 234:1306–1308, 1977.

[22] A. R. Bell. The acceleration of cosmic rays in shock fronts. *Monthly Notices of the Royal Astronomical Society*, 182:147–156, 1978.

[23] R.D. Blandford, *et al.* Particle acceleration by astrophysical shocks. *Astrophysics Journal*, 221:L29–L32, 1978.

[24] Samuel Ting. The Alpha Magnetic Spectrometer on the International Space Station. *Nuclear Physics B*, 243244:12–24, 2013.

[25] P. S. Marrocchesi. CALET on the ISS: a high energy astroparticle physics experiment. *Journal of Physics: Conference Series*, 718:052023, 2016.

[26] J. Chang, *et al.* The DArk Matter Particle Explorer mission. *Astropart. Phys.*, 95:6–24, 2017.

[27] AMS-02 Homepage. URL https://ams.nasa.gov.

[28] B. Alpat, *et al.* The internal alignment and position resolution of the AMS-02 silicon tracker determined with cosmic-ray muons. *Nuclear Instruments and Methods in Physics Research A*, 613(2):207–217, 2010.

[29] G. Ambrosi, *et al.* Alignment of the AMS-02 silicon Tracker. *Proceedings of the 33th International Cosmic Ray Conference*, C-07-02:1260, 2013.

[30] G. Ambrosi, *et al.* The spatial resolution of the silicon tracker of the Alpha Magnetic Spectrometer. *Nuclear Instruments and Methods in Physics Research A*, 869: 29–37, 2017.

[31] Ph. v. Doetinchem, *et al.* Performance of the AMS-02 transition radiation detector. *Nuclear Instruments and Methods in Physics Research A*, 58:526535, 2006.

[32] V. Bindi, *et al.* Calibration and performance of the AMS-02 time of flight detector in space. *Nuclear Instruments and Methods in Physics Research A*, 743:22–29, 2014.

[33] M. Aguilar-Benitez, *et al.* In-beam aerogel light yield charaterization for the AMS RICH detector. *Nuclear Instruments and Methods in Physics Research A*, 614(2): 237–249, 2010.

[34] F. Cadoux, *et al.* The Ams-02 electromagnetic calorimeter. *Nuclear Physics B - Proceedings Supplements*, 113(1-3):159–165, 2002.

[35] M. Aguilar, *et al.* Precision Measurement of the Proton Flux in Primary Cosmic Rays from Rigidity 1 GV to 1.8 TV with the Alpha Magnetic Spectrometer on the International Space Station. *Physics Review Letter*, 114:171103, 2015.

[36] M. Aguilar, *et al.* Precision Measurement of the Helium Flux in Primary Cosmic Rays of Rigidities 1.9 GV to 3 TV with the Alpha Magnetic Spectrometer on the International Space Station. *Physics Review Letter*, 115:211101, 2015.

[37] O. Adriani, *et al.* Extended Measurement of the Cosmic-Ray Electron and Positron Spectrum from 11 GeV to 4.8 TeV with the Calorimetric Electron Telescope on the International Space Station. *Physics Review Letter*, 120:261102, 2018.

[38] P. S. Marrocchesi, *et al.* Beam test performance of a scintillator-based detector for the charge identification of relativistic ions. *Nuclear Instruments and Methods in Physics Research A*, 659:477–483, 2011.

[39] Yuki Shimizu, *et al.* The CALET CHD for determination of nuclear charge. *Proceedings of the 32th International Cosmic Ray Conference*, C11-08-11:391, 2011.

[40] P. Brogi, *et al.* CALET measurements with cosmic nuclei: expected performances of tracking and charge identification. *Proceedings of the 34th International Cosmic Ray Conference*, C15-07-30:595, 2015.

[41] S. Torii, *et al.* The CALorimetric Electron Telescope (CALET): a High-Energy Astroparticle Physics Observatory on the International Space Station. *Proceedings of the 34th International Cosmic Ray Conference*, C15-07-30:581, 2015.

[42] G. Ambrosi, *et al.* Direct detection of a break in the tera-electronvolt cosmic-ray spectrum of electrons and positrons. *Nature*, 552:63–66, 2017.

[43] P. Bernardini. ARGO-YBJ experiment in Tibet. *Journal of Physics: Conference Series*, 120(6):06202, 2008.

[44] G. Sinnis. HAWC: A NEXT GENERATION ALL-SKY VHE GAMMA-RAY TELESCOPE. *The Tenth Marcel Grossmann Meeting*, pages 1068–1088, 2012.

[45] J. Goodman. HAWC: The High Altitude Water Cherenkov Observatory. *Proceedings of the Centenary Symposium 2012: Discovery of Cosmic Rays*, 2012.

[46] G. Aielli. Layout and performance of RPCs used in the Argo-YBJ experiment. *Nuclear Instruments and Methods in Physics Research A*, 562:9296, 2006.

[47] B. Bartoli, *et al.* Cosmic ray proton plus helium energy spectrum measured by the ARGO-YBJ experiment in the energy range 3300 TeV. *Physics Review D*, 91: 112017, 2015.

[48] A. D'Amone, *et al.* Measurement of the cosmic ray all-particle and light-component energy spectra with the ARGO-YBJ experiment. *arXiv:1502.04840*, 2015.

[49] R. Alfaro, *et al.* All-particle cosmic ray energy spectrum measured by the HAWC experiment from 10 to 500 TeV. *Physics Review D*, 96:122001, 2017.

[50] J. C. Arteaga-Velzquez, *et al.* The spectrum of the light component of TeV cosmic rays measured with HAWC. *Proceedings of the 36th International Cosmic Ray Conference*, PoS(ICRC2019)176, 2019.

[51] J. Chang. Dark Matter Particle Explorer: The first Chinese Cosmic Ray and Hard γ ray Detector in Space. *Chinese Journal of Space Science*, 34(5):550–557, 2014.

[52] G. Bertone, *et al.* Particle dark matter: evidence, candidates and constraints. *Physics Report*, 405(5-6):279–390, 2005.

[53] C. Boehm, *et al.* MeV Dark Matter: Has It Been Detected ? *Physics Review letters*, 92:101301, 2004.

[54] Z. M. Wang, *et al.* Temperature dependence of the plastic scintillator detector for DAMPE. *Chinese Physics C*, 41(1):016001, 2017.

[55] Y. H. Yu, *et al.* The plastic scintillator detector at DAMPE. *Astroparticle physics*, 94:1–10, 2017.

[56] P. Azzarelloa, *et al.* The DAMPE silicon-tungsten tracker. *Nuclear Instruments and Methods in Physics Research A*, 831:378–384, 2016.

[57] Z. Y. Zhang, *et al.* The calibration and electron energy reconstruction of the BGO ECAL of the DAMPE detector. *Nuclear Instruments and Methods in Physics Research A*, 836:98–104, 2016.

[58] M. He, *et al.* Geant4 Simulation of Neutron Detector for DAMPE. *Chinese Astronomy and Astrophysics*, 40(4):474–482, 2016.

[59] G.Ambrosi, *et al.* The on-orbit calibration of DArk Matter Particle Explorer. *Astropart.Phys.*, 106(16):18–34, 2019.

[60] Particle Data Group PDG. Passage of particles through matter. *Nuclear and Particle Physics*, 33(27):258–270, 2006.

[61] C. Yue, *et al.* Charge Measurement of Cosmic Ray Nuclei with the PSD of DAMPE. *Proceedings of the 36th International Cosmic Ray Conference*, PoS(ICRC2019)063, 2019.

[62] W. B. Atwood, *et al.* The Large Area Telescope on the Fermi Gamma-Ray Space Telescope Mission. *The Astrophysical Journal*, 697(10):10711102, 2009.

[63] M. Feroci, *et al.* SuperAGILE: The hard X-ray imager for the AGILE space mission. *Nuclear Instruments and Methods in Physics Research Section A*, 581(3): 728–754, 2007.

[64] X. Wu, *et al.* The Silicon-Tungsten Tracker of the DAMPE Mission. *Proceedings of the 34th International Cosmic Ray Conference*, PoS(ICRC2015)1192, 2016.

[65] Hamamatsu Photonics. URL http://www.hamamatsu.com/us/en/index.html.

[66] Integrated Detector Electronics AS. URL http://www.ideas.no.

[67] R. Fruhwirth, *et al.* Application of Kalman filtering to track and vertex fitting. *Nuclear Instruments and Methods in Physics Research Section A*, 262:444–450, 1987.

[68] V. Gallo, *et al.* The test results of the Silicon Tungsten Tracker of DAMPE. *Proceedings of the 34th International Cosmic Ray Conference*, PoS(ICRC2015)1199, 2016.

[69] J. H. Guo, *et al.* Design of the Prototype Readout System of BGO Calorimeter in the Space Dark Matter Detector of Purple Mountain Observatory. *Chinese Astronomy and Astrophysics*, 36(3):318–326, 2012.

[70] J. Wu, *et al.* Expected performance of the Chinese high energy cosmic particle detector to be in space. *Proceedings of the 32th International Cosmic Ray Conference*, 5(0069), 2011.

[71] S.Agostinelli, *et al.* Geant4: a simulation toolkit. *Nuclear Instruments and Methods in Physics Research A*, 506(3):250–303, 2003.

[72] D. M. Drake, *et al.* New electronically black neutron detectors. *Nuclear Instruments and Methods in Physics Research A*, 247(3):576–582, 1986.

[73] C. Q. Feng, *et al.* Development of the DAQ system of Chinese high energy cosmic ray detector in space. *Proceedings of the 32th International Cosmic Ray Conference*, 5(0989), 2011.

[74] Z. Y. Zhang. *The development and calibration of the BGO calorimeter of the Dark Matter Particle Explorer.* PhD thesis, University of Science and Technology of China, 2015.

[75] L. Landau, *et al.* The Cascade Theory of Electronic Showers. *Proceedings of the Royal Society A*, 592:1, 2004.

[76] H. Bichsel, *et al.* Passage of particles through matter. *Physics Letters B*, 592:1, 2004.

[77] M. V. S. Rao, *et al. Extensive Air Shower.* World Scientific, 1998.

[78] K. A. Olive, *et al.* Review of particle physics. *Chinese Physics C*, 38(9):090001, 2014.

[79] R. Bock, *et al.* Parametrization of the longitudinal development of hadronic showers in sampling calorimeters. *Nuclear Instruments and Methods in Physics Research A*, 186(3):533–539, 1981.

[80] D. Acosta, *et al.* Lateral shower profiles in a lead/scintillating fiber calorimeter. *Nuclear Instruments and Methods in Physics Research A*, 316(2):184–201, 1992.

[81] Chuan Yue. *Energy Reconstruction of Dark Matter Particle Explorer and Analysis of Cosmic-ray Proton Flux.* PhD thesis, Purple Mountain Observatory, Chinese Academy of Sciences, 2018.

[82] T Antoni, *et al.* Test of high-energy interaction models using the hadronic core of EAS. *Journal of Physics G: Nuclear and Particle Physics*, 25(10):21612175, 1999.

[83] T Antoni, *et al.* Test of Hadronic Interaction Models in the Forward Region with KASCADE Event Rates. *Journal of Physics G: Nuclear and Particle Physics*, 27 (8):1785–1798, 2001.

[84] L. Lindemann, *et al.* Unfolding by weighting Monte Carlo events. *Nuclear Instruments and Methods in Physics Research A*, 354(2-3):516–521, 1995.

[85] L. Lindemann, *et al.* A determination of (M_{z^o}) at LEP using resummed QCD calculations. *ZEITSCHRIFT FOR PHYSIK C*, 59:1–19, 1993.

[86] G. D'Agostini, *et al.* A multidimensional unfolding method based on Bayes' theorem. *Nuclear Instruments and Methods in Physics Research A*, 362:487–498, 1995.

[87] A. Hoecker, *et al.* SVD Approach to Data Unfolding. *Nuclear Instruments and Methods in Physics Research A*, 372:469–481, 1996.

[88] B. Malaescu. An Iterative, Dynamically Stabilized(IDS) Method of Data Unfolding. *arXiv:1106.3107v1*, 2011.

[89] B. Malaescu. An iterative, dynamically stabilized method of data unfolding. *arXiv:0907.3791v1*, 2009.

[90] M. N. Mazziotta. A method to unfold the energy spectra of point like sources from the Fermi-LAT data. *arXiv:0912.1236*, 2009.

[91] M. Ackermann, *et al.* Measurement of the high-energy gamma-ray emission from the Moon with the Fermi Large Area Telescope. *Physical Review D*, 93:082001, 2016.

[92] F. Loparco, *et al.* Unfolding spectral analysis of the Fermi-LAT data. *arXiv:0912.3695*, page 082001, 2009.

[93] G. Aad, *et al.* Unfolding spectral analysis of the Fermi-LAT data. *Physics Letters B*, 688:2142, 2010.

[94] T. Adye, *et al.* Corrected error calculation for iterative Bayesian unfolding. *http://hepunx.rl.ac.uk/∼ adye/software/unfold/bayes_errors.pdf*, 2011.

[95] V. Blobel. An Unfolding Method for High Energy Physics Experiments. *arXiv:hep-ex/0208022*, 2002.

[96] M. Schmelling. The method of reduced cross-entropy: a general approach to unfold probability distributions. *Nuclear Instruments and Methods in Physics Research A*, 340(2):400–412, 1994.

[97] C. L. Lawson, *et al.* *Solving Least Square Problems*. Society for Industrial and Applied Mathematics (SIAM), 1987.

[98] O. Adriani, *et al.* PAMELA Measurements of Cosmic-Ray Proton and Helium Spectra. *Science*, 332:69–72, 2011.

[99] H.S.Ahn, *et al.* The energy spectra of protons and helium measured with the ATIC experiment. *Advances in Space Research*, 37:1950–1954, 2006.

[100] G. O. Dickson, *et al.* Magnetic anomalies in the South Atlantic and ocean floor spreading. *Journal of Geophysical Research*, 73(6):2087–2100, 1968.

[101] G. P. Ginet, *et al.* Energetic Proton Maps for the South Atlantic Anomaly. *IEEE Radiation Effects Data Workshop*, pages 1–8, 2007.

[102] R. Gubby, *et al.* Energetic Proton Maps for the South Atlantic Anomaly. *Journal of atmospheric and solar-terrestrial physics*, 64(16):1723–1733, 2002.

[103] J. Allison, *et al.* Geant4: a simulation toolkit. *IEEE Transactions on Nuclear Science*, 53(1):270–278, 2006.

[104] A.B. Kaidalov, *et al.* Predictions of Quark-Gluon String Model for pp at LHC. *Eur.Phys.J.*, C67:397–404, 2010.

[105] V. V. Uzhinsky. Fritiof (FTF) Model, 2013. URL https://indico.cern.ch/event/232125/contributions/1541450/attachments/386057/537020/FTF.pdf.

[106] S. Roesler, *et al.* The Monte Carlo Event Generator DPMJET-III. *arXiv:hep-ph/0012252v1*, 2000.

[107] CRMC (Cosmic Ray Monte Carlo package), 2019. URL https://web.ikp.kit.edu/rulrich/crmc.html.

[108] G. Battistoni, *et al.* Overview of the FLUKA code. *Annals of Nuclear Energy*, 82:10–18, 2015.

[109] E. Thebault, *et al.* International Geomagnetic Reference Field: the 12th generation, Earth. *Earth, Planets and Space*, 67:79, 2015.

[110] R. Fruhwirth. Application of Kalman filtering to track and vertex fitting. *Nuclear Instruments and Methods in Physics Research A*, 262:444–450, 1987.

[111] P. Ma, *et al.* A Method of Alignment of the Plastic Scintillator Detector of DAMPE. *Research of Astronomy and Astrophysics*, 19:082, 2019.

[112] N.Nakamura, *et al.* Review of Particle Physics. *Particle data group*, 2016.

[113] E. Atkin, *et al.* First results of the cosmic ray NUCLEON experiment. *arXiv:1702.02352v2*, 2018.

[114] V. I. Zatsepin, *et al.* Three components model of cosmic ray spectra from 10 GeV to 100 PeV. *Astronomy and Astrophysics*, 458:1–5, 2006.

[115] K. H. Kampert, *et al.* Cosmic Rays in the 'Knee'-Region - Recent Results from KASCADE. *arXiv:astro-ph/0405608*, 2004.

[116] Y. Dong, *et al.* Overall Status of the High Energy Cosmic Radiation Detection Facility Onboard the Future Chinas Space Station. *Proceedings of the 36th International Cosmic Ray Conference*, PoS(ICRC2019)063, 2019.

[117] M. Chen. Status and first result of LHAASO-WCDA. *Proceedings of the 36th International Cosmic Ray Conference*, PoS(ICRC2019)217, 2019.